Approved: Greg Nellis

Gregory F. Nellis, William A. and Irene Ouweneel-Bascom Professor

Approved: _____

Mark Anderson, Assistant Professor

Approved: _____

Arganthaël Berson, Faculty Associate

Date: _____

GEOMETRIC CONSIDERATIONS FOR STABILITY OF DIRECT CONTACT STEAM CONDENSATION IN LIQUID CROSSFLOW

By

Zach Alden

A thesis submitted in partial fulfillment of

the requirements for the degree of

Master of Science

(Mechanical Engineering)

at the

UNIVERSITY OF WISCONSIN-MADISON

2020

Contents

Acknowledgements

I would like to thank my trio of advisors, Arganthaël Berson, Kristofer Dressler, and Greg Nellis, for the knowledge, encouragement, and undisputed belief that I could do great things during my time in the MFVAL lab, even when it was only by Google Chat meetings during the COVID pandemic. You kept me going when I didn't think I could keep going myself, and I am forever indebted in this regard.

I would like to thank everyone at Hydro-Thermal Corporation for keeping me constantly on my toes during our biweekly meetings. Jim Zaiser, Shawn Berg, and Mark Kliewer showed constant enthusiasm with the work presented in this thesis, and I will always laugh at Jim asking just one more question during our meetings. Thank you for driving hours just to check that my loop is working properly.

A thank you to all the undergraduate students who have helped on this project during my time as a graduate student. Mitch Langer (who I will concede is a graduate student as well), Spencer Enriquez, Gunnar Maples, Christian Thorpe, Ali Heineman, and Lauren Hunter all provided a light during my time in the lab. I have learned just as much from them as they have learned from me.

An enormous thank you to Shaun Aakre for providing me with nozzle scans in the middle of a pandemic. They were very much worth the effort.

They say that if you are the smartest person in the room, you need to find a better room. That is not the case with the MFVAL team. Roman Morse, Jason Chan, and Brett Lindeman are some of the smartest people I know, and it was an honor to work beside them. While Brett Lindeman gave me guidance on pretty much every aspect of my project, I consider the deal even by showing him how to use the CSR option in the PCC software. Jason is a LabVIEW wizard, and I can only bow in deference. Roman was a joy to have alongside in classes and in the lab, giving me a pep talk when I needed it most.

I would like to thank the friends that kept me sane during these two years. To Meg Sill for the nights at Blue Velvet, the brunches at Marigold Kitchen, and the days I needed to use your sunroom. To

Marisa Dunning and the SND crew for fun times in the classroom, senior design room, and Sunday night dinners. To Tanner Mantel for coming to my aid whenever I was at my wits end. To Eve Williams and the ULC staff for a quiet place to write (before the pandemic) and a hot tea whenever I needed it.

Finally, I'd like to thank my family, without whom I would not be where I am. To Rick Alden and Judi Jesse for constant advice and a comforting place to stay in the middle of a global pandemic. To Josh and Mollie Alden for a bit of small town wisdom. To my dog Molly for reminding me of what matters most. Thank you.

Figure 0. To man's best friend. Deeply missed.

1. Introduction

Direct contact steam condensation is a common mode of two-phase energy transfer in industrial fluid heating applications and power plant pressure relief systems. Its ability to introduce all of the available energy within the steam directly into the process fluid rather than having to cross the conductive boundary associated with conventional heat exchangers is a distinct advantage. The direct introduction of steam also overcomes the fouling and clogging associated with the buildup of baked on substances that can degrade the performance of conventional heat exchangers.

Under many operating conditions the steam condensation is stable and introduces no safety concerns. However, there are process conditions where the steam condensation becomes unstable, introducing pressure oscillations associated with the expansion and contraction of the steam plume. These pressure oscillations generate loud acoustic noise, which is unpleasant and can reach levels beyond proper safety guidelines. These pressure oscillations can even reach a level where they induce stresses that pose a risk to the surrounding structure and equipment.

Much research has been devoted to characterizing this ‘switch’ from stable to unstable behavior. Many researchers have categorized steam injection into distinct regimes, such as condensation oscillation or chugging, based on process parameters such as steam mass flux and liquid subcooling. Despite these many efforts, a completely unified regime ‘map’ has not been found. Regime maps in the literature do not agree quantitatively with each other or with the work done in the Multiphase Flow Visualization and Analysis Lab at the University of Wisconsin - Madison. It is also noted that the literature is largely focused on these process parameters and does not generally provide much detail regarding the geometry of the injection nozzle. The literature includes a wide range of nozzle diameters and injection environments, but no articles have been found that test the stability of a 0.096” diameter nozzle injected vertically into a crossflow of water, the injection environment presented here. There is also scant literature on the stability effect of geometric alterations to the nozzle design.

This thesis focuses on the conditions that lead to injection instability and the impact of geometric variations of the nozzle on stability. Better equipment design and the ability to optimize the injection process are important outcomes that are enabled by the work described in this thesis. While process conditions may be adjusted during operation, the proper starting geometry sets the playing field for the transition to instability. This work shows that small variations in geometry can cause changes in the transition threshold for instability that are large compared to process parameters involved.

2. Background

Since the 1970s, research into direct contact condensation has been devoted to understanding condensation regimes [1-20], steam jet patterns and penetration lengths [12, 15-16, 21-23], heat transfer coefficients [8, 13-14, 22, 24], and pressure oscillations introduced by the steam condensation [1-5, 17, 20, 24-36], all of which are interrelated. The injection environments that have been studied range from stagnant pools of liquid to parallel flow or crossflow liquid channels, and the nozzle that have been studied range from horizontal to vertical to angled and from orifice holes to de Laval nozzles. The majority of published research focuses on horizontal and vertical downward injection into a stagnant pool of liquid. Safety cooling systems in boiling water reactors require that the nuclear reactor reject large amounts of heat through steam vents into pools of water; hence, the bulk of research in steam injection is centered around this application. Other applications of direct contact condensation include industrial process heating systems, which involve the more complex injection environments associated with a flowing liquid channel. This application and environment is the focus of this thesis.

Previous work on direct contact condensation in the Multiphase Flow Visualization and Analysis Lab (MFVAL) at UW-Madison include a study on jet penetration length and the temperature distribution associated with steam that is being vertically injected into a crossflow of water [37], and experiments on condensation stability as a function of the process parameters of liquid temperature, injection pressure ratio, and liquid flow rate [38]. The former study is not discussed in this work, but the latter study provides the foundation for this work. The work presented here is focused on understanding geometric changes to the injection nozzle and the effect on the condensation mode and propagation into the injection environment.

This background section serves to elaborate on two main distinctions in the literature: previously proposed ‘regime maps’ and frequency distributions associated with the steam plume activity. There is no literature that describes a proper study of geometric effects on nozzle stability. It is noted, however, that

many different nozzle geometries have been used in the various literature studies. These large variations in nozzle size and/or shape may explain the discrepancies in some of the conclusions that are found in the literature. As noted in the previous work in the MFVAL and also shown in the present work, quantitative results from the literature do not agree with each other or the experimental findings from the MFVAL; however, qualitative trends still hold across the nozzle geometries.

2.1 Literature Condensation Regimes

Literature commonly reports the findings of direct contact condensation in the form of 'regime maps' that discretely demarcate steam plume behaviors based on visual observations of the plume as it is being injected. This map serves as an indication of when the plume should either remain stable or unstable based on process conditions. The most common process conditions used in the literature are steam mass flux and liquid water temperature (or the degree of subcooling of the liquid water). These have been chosen to represent the driving force for the steam injection process (in the steam mass flux) and the driving force for the condensation process (the degree of subcooling); these are the two forces that are believed to have the most influence on the stability of the steam plume. Other regime parameters include the water Reynolds number for injection into a moving flow [13, 15, 17], the nozzle pressure ratio [12], and the ambient (outlet of nozzle) pressure [16, 20].

Appendix A shows a comprehensive breakdown of regime maps that have been developed through the years, including their regime parameters, the identified condensation regimes, injection environment, steam jet orientation, nozzle diameter, water temperature, and steam mass flux. It is clearly seen that the regime maps include a wide range of nozzle diameters, water temperatures, and steam mass fluxes and have been measured in different environments. To date, no single, universal regime map is available that covers the entire range of conditions and environments encountered in the literature.

Arinobu [1] created one of the first regime maps of direct contact steam condensation in a pool of subcooled water, shown in Fig. 1. Labeling by number, they classified regimes by location where the

steam condenses in relation to the injector (i.e. inside the nozzle or outside) and the oscillations of the steam plume interface. Regimes II and IV were given special names of chugging and condensation oscillation, respectively. Chugging was defined as the steam pushing out of the injector, collapsing, water rushing into the injector to fill the void left by this collapse, and the steam continuing the cycle by pushing out of the injector. Condensation oscillation was named for the periodic pressure oscillations observed in the water as the steam-water interface oscillated violently outside of the injector. These two regimes have shown up continuously in research and are some of the most common methods used to characterize the steam plume stability.

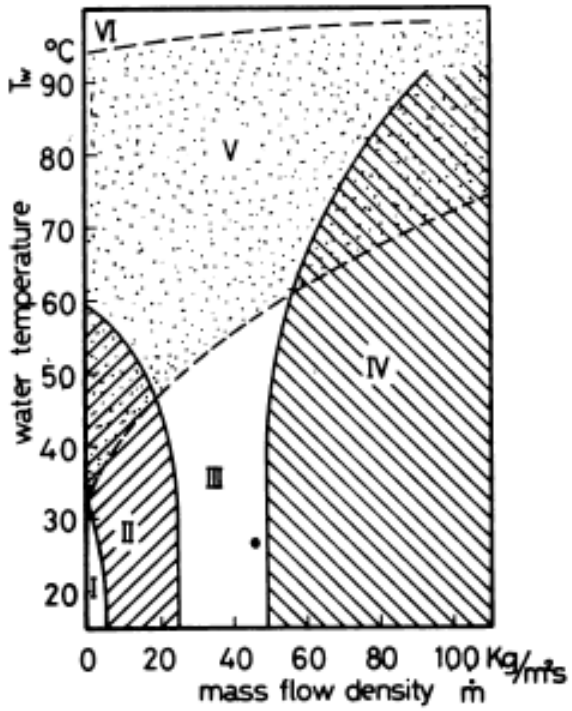

Figure 1. Regime map proposed by Arinobu [1] that demarcated plume phenomena by number. Regions II and IV are one of the first unique regime names in chugging and condensation oscillation, respectively. The other regions do not have formal names. Steam fully condenses in the injection pipe in region I. Steam no longer condenses in the pipe in region III. The pipe is surround by a steam bubble in region V, and the steam no longer condenses in region VI.

Chan and Lee [2] presented a more comprehensive regime map with additional regimes included; for example, ellipsoidal jet, oscillatory cone jet, oscillatory bubble, external chugging, and internal chugging. The criteria for regime classification are the location of the steam condensation relative to the injector and the location of bubble detachment along the steam plume. While they discuss similar regime structures under similar process conditions, the demarcation of these regimes is different than that of Arinobu [1]. For example, the transition to chugging occurs around 75 $\frac{kg}{m^2 s}$ rather than 20 $\frac{kg}{m^2 s}$. The closest regime descriptions to condensation oscillation are oscillatory cone jet and ellipsoidal jet, and this transition occurs around 125 $\frac{kg}{m^2 s}$ rather than 50 $\frac{kg}{m^2 s}$. A greater emphasis was placed on bubble formation, producing a wider range of regimes with very descriptive names. Many subsequent researchers cite Chan and Lee as one of the first regime maps, but the differences between Chan and Lee and Arinobu highlight the challenge of quantitively defining regime transitions. It is important to note that the nozzle diameter used in the study of Chan and Lee is almost double (51 mm) that of those used by Arinobu (16.1, 27.6 mm).

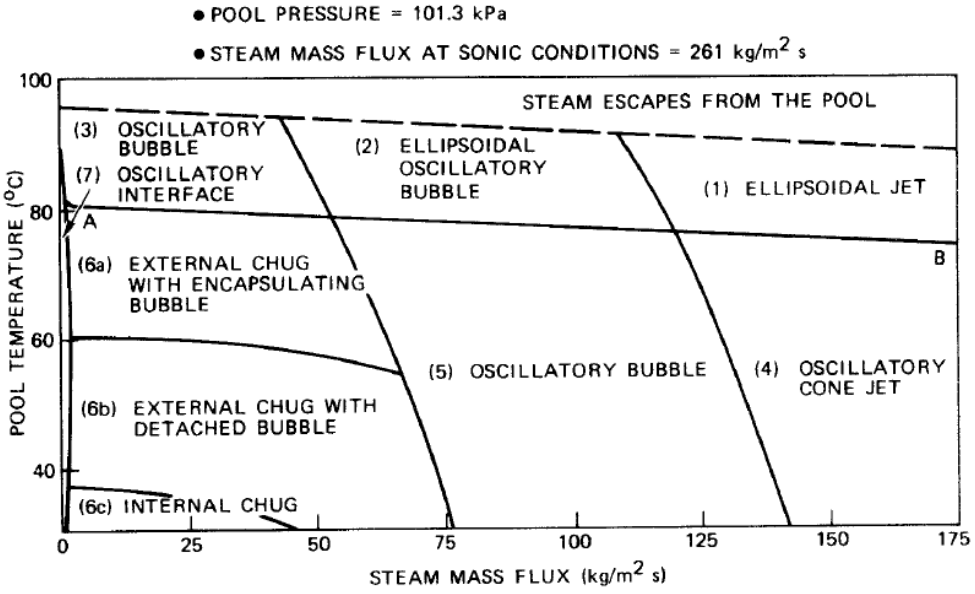

Figure 2. A more comprehensive regime map proposed by Chan and Lee [2]. More descriptive regime names are given with a greater emphasis on bubbling, jetting, and chugging classification.

Numerous researchers have subsequently proposed other regime maps with their own unique regime names. The regime map of Cho et al. [9] is one that is often cited. Cho et al. proposed six regime names across 0-100°C water temperature and 45-450 $\frac{kg}{m^2 s}$ steam mass flux for horizontal injection into a stagnant pool. Chugging (C) occurs at steam mass fluxes and water temperatures that are similar to those observed by Chan and Lee [2] and is defined in a manner that is consistent with Arinobu [1]. Condensation oscillation (CO) is also defined in a manner that is consistent with Arinobu [1] and the lower transition to this regime occurs under similar process conditions to those observed by Chan and Lee [2]. Transition chugging (TC) serves as an intermediary between these two regimes. Bubble condensation oscillation (BCO) involves large steam bubbles breaking off from the steam plume and either condensing or escaping to the free surface of the water. Interface oscillation condensation (IOC) is a regime that is described as being similar to that of CO but with the steam-water interface oscillating violently. Stable condensation (SC) is for the first time described in this regime map, as well as that of Chun et al. [8]. Steam is quietly condensed with no violent oscillations in the liquid water. The trends of Cho et al. [9] echo other researchers in that higher mass fluxes and lower water temperatures produce more stable regimes. It should also be noted that the nozzle diameters used by Cho et al. [9] are not the same as those used by Chan and Lee [2] (5, 10, 15, and 20 mm vs 51 mm), yet these two regime maps are better aligned than Cho et al. is with Arinobu [1] even those these use similar nozzle diameters (5, 10, 15, and 20 mm vs 16.1, 27.6 mm).

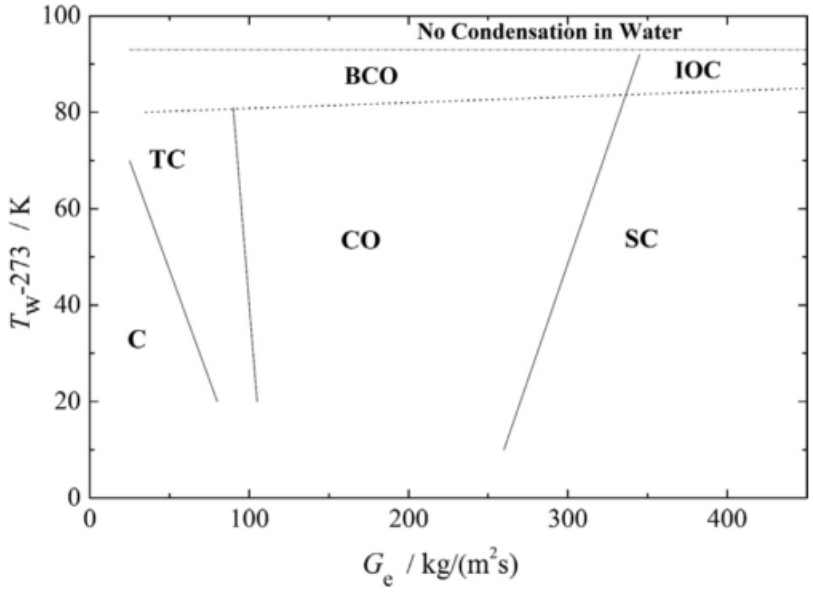

Figure 3. Regime map proposed by Cho et al. [9]. Higher mass fluxes introduce the stable condensation (SC), middle mass fluxes introduce condensation oscillation (CO), and low mass fluxes initiate chugging (C).

Recently research focus has shifted to steam injection into a flowing liquid environment. The water Reynolds number is usually given as a third parameter in regime maps associated with this situation in order to characterize the more complex process. Xu et al. [16] provides the experimental facility (3 mm diameter nozzle injected into a crossflow of water) and process conditions (20-70°C water temperature and 0-900 $\frac{kg}{m^2 s}$ steam mass flux) that is closest to the work presented here; however, Xu et al. describe regime maps (for example, Fig. 4) that differ dramatically from those observed in this work. The regimes that are described include hemisphere, conical, and expansion-contraction, which are all derivatives of a stable regime definition; no instability was noted in their work at all. This result may be due to the use of water pressures and a nozzle injection orientation that are different from the work presented here. The regime map presented in Fig. 4 for instance only presents nozzle outlet pressures that are at least 100 kPa less than that used in this work, and the inlet pressure is not given for the regime map, thereby calling into question what the pressure ratio across the nozzle is for comparison. The orientation used by Xu et al. is

horizontal steam injection, rather than the vertical injection used in this work. These differences highlight the complexity of the stability problem and the difficulty of directly comparing regime maps.

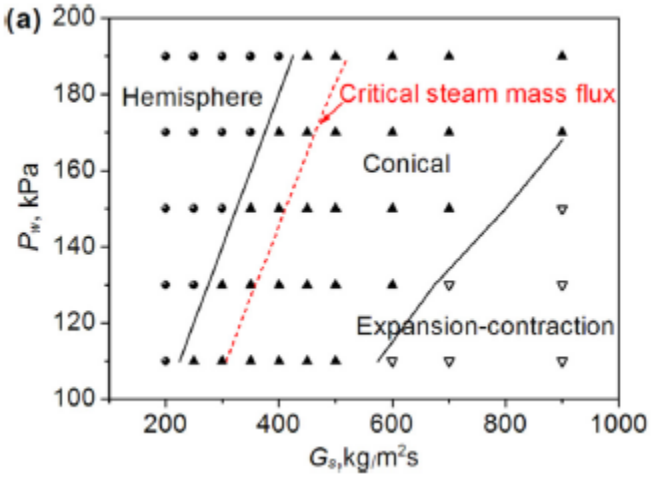

Figure 4. Regime map proposed by Xu et al. [16]. One of few regime maps presented in terms of steam mass flux and outlet pressure, the regimes presented here do not follow literature or experimental expectations. Data taken at a constant Reynolds number of 29,473 and process water temperature of 30°C.

Only one regime map was found in the literature that explicitly considered nozzle injection diameter. Petrovic De With et al. [11] combined three regime maps from previous researchers [2,6,7] with differing nozzle diameters each injecting into a stagnant pool into a single regime map that is based on injector nozzle diameter, steam mass flux, and degree of subcooling, as shown in Fig. 5 and Fig. 6. The data suggests that high steam mass fluxes introduce only jetting phenomena and no instability in the steam plume. Differences in nozzle diameter mostly affect the bubbling and chugging regimes, with higher diameter nozzles transitioning to instability at higher mass fluxes.

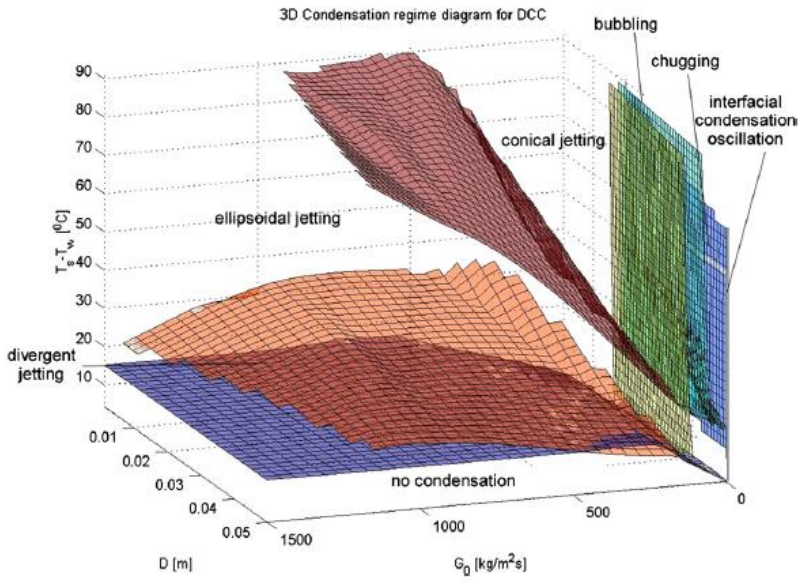

Figure 5. Combined regime map proposed by Petrovic de With et al. [11]

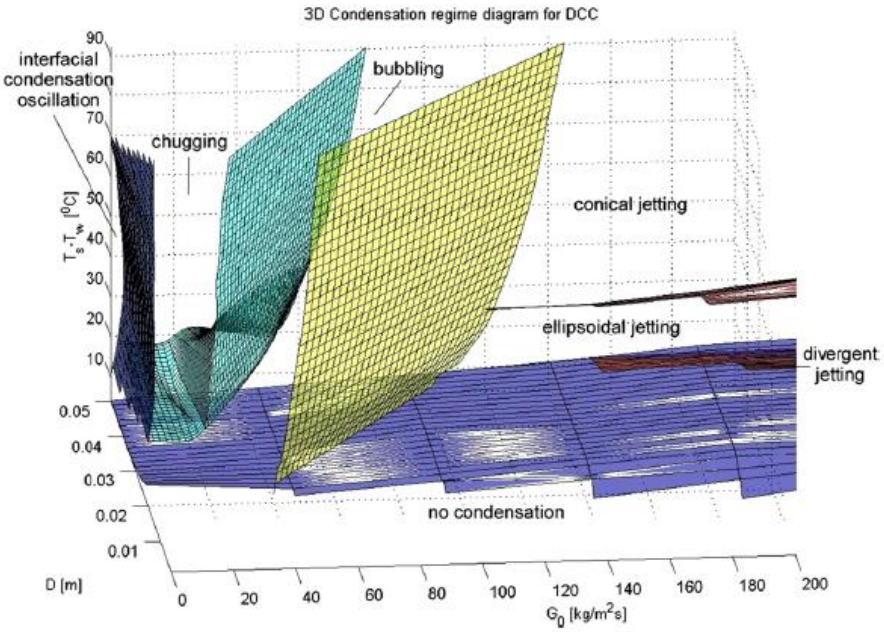

Figure 6. Side profile of regime map by Petrovic de With et al. [11]. This view more clearly demonstrates the effect of nozzle diameter on bubbling and chugging stabilities.

In 2018, Zhao and Hibiki [19] attempted to consolidate the many regimes that have been presented in the literature into a unified naming convention. They proposed that the regimes be called

chugging, hemispherical bubble oscillation, condensation oscillation, stable condensation, steam escape, and no condensation. Transition boundaries between these regimes were created based on a comparison of previous regime maps, empirical correlations, and an analytical model proposed by Liang and Griffith [7]. Yet discrepancies between maps, correlations, and models were still observed, due to differences in test section design and the dependence on secondary parameters that might affect stability. As a result, the authors were unable to generate a completely unified regime map.

2.2 Literature Oscillation Frequencies

In addition to classifying condensation regimes, researchers have focused on determining the characteristics of the pressure oscillations introduced by the steam plume. These pressure oscillations have a significant impact on the noise level generated during the injection process as well as the potential of damage to injection and process equipment. Simpson and Chan [24] were among the first to perform experiments in a stagnant pool. They investigated the pressure oscillation profiles through a range of injection diameters from 6.35 to 22.2 mm, pool temperatures from 25 to 64°C, and steam mass fluxes from 147 to 333 kg/m^{2}s. Pressure oscillations at frequencies in the range of 100-500 Hz were observed, with higher frequencies occurring at lower pool temperatures and smaller diameters. Pressure oscillation amplitude increased with increasing pool temperatures, tube diameters, and steam mass flux.

Qiu et al. [27] defined two dominant frequencies generally found during steam injection, which they referred to as the first and second dominant frequency. These were attributed to the periodic variation of the main steam plume, and the generation and disappearance of steam bubbles, respectively. They likewise showed that these frequencies decreased as the pool temperature increased, as shown in Fig. 7.

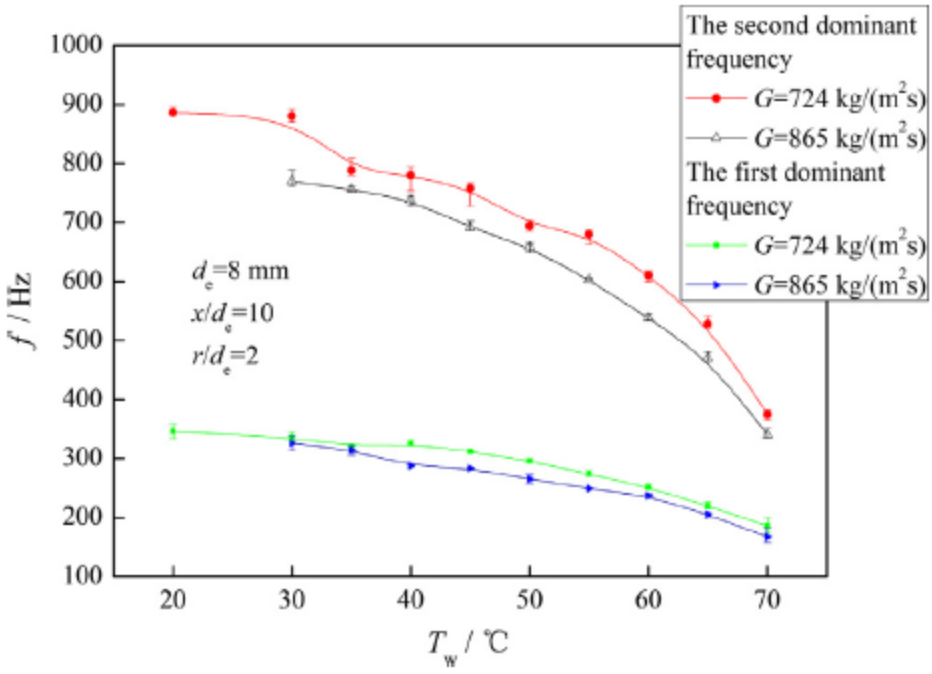

Figure 7. Dominant plume frequencies as a function of pool temperature. The first dominant frequency is the oscillation of the steam plume while the second dominant frequency is the generation and disappearance of bubbles.

Qiu et al. [31] subsequently investigated the propagation of pressure oscillations into the surrounding fluid. They found that oscillation amplitude increased along the plume length and attenuated with increasing distance from the steam plume end, becoming attenuated by 90% at a dimensionless distance (distance/exit diameter) of 100. Hong et al. [26] investigated the dominant frequency associated with condensation oscillation (related to the oscillation of the steam plume during condensation) and found it to be within the range of 50-500 Hz, decreasing with increased pool temperature and steam mass fluxes above a specific threshold. Like Qiu et al. [27], Chong et al. [29] found a second dominant frequency generated by steam bubble oscillations on the order of 600-1400 Hz. Tang et al. [33] identified dominant frequencies on the order of 150-300 Hz that were due to the periodic variation of the steam plume and frequencies greater than 7000 Hz that were related to the collapse of microbubbles from the steam plume in a subcooled pool. The frequencies reported in these works vary by flow regime, steam injection environment, and nozzle geometry and are noticeably different from the ones reported here.

Researchers have combined pressure oscillation measurements with high-speed imaging to help with the identification of flow regimes. Xu et al. [32] measured the pressure variation for chugging, condensation oscillation I, condensation oscillation II, and stable steam condensation regimes while also obtaining high speed videos of these phenomena. This work allowed these regimes to be identified with a combination of visual and pressure fluctuation data. Chugging was characterized by high amplitude and low frequency pressure pulses, condensation oscillation I exhibited organized pressure oscillations on the order of 50 kPa, condensation oscillation II exhibited more disorganized oscillations around 25 kPa, and stable condensation had low-amplitude oscillations. More studies of this type are required to improve the identification of the different regimes of direct-contact condensation.

3. Materials and Methods

3.1 Test Facility

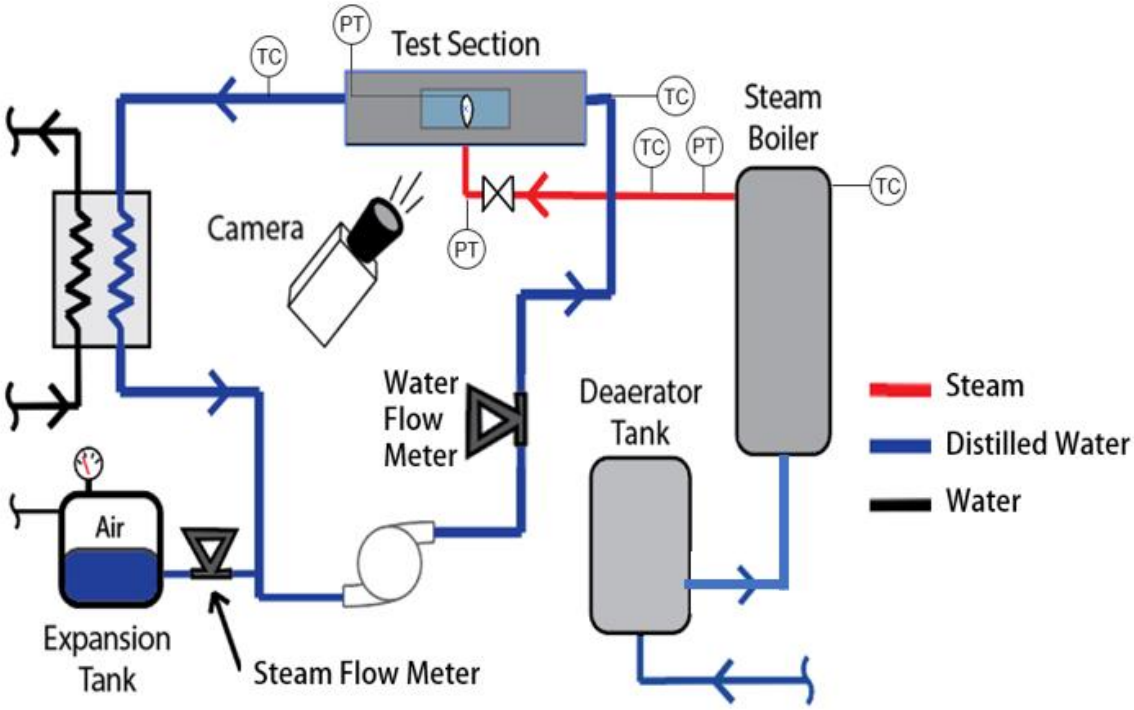

Figure 8. Experimental apparatus schematic showing major piping and components.

The overall schematic diagram of the experimental apparatus is shown in Fig. 8. Saturated steam is produced in a 48 kW electric boiler and sent through thermally-insulated pipes to the nozzle inlet, where a ball valve is used to stop or start steam injection. A deaerator tank is used to feed the boiler to reduce the amount of air entering the steam line during injection. Steam is occasionally bypassed to this tank in order to heat the incoming water. During normal operation, steam is injected vertically into the process water into a test section that allows optical access. Saturation temperature and pressure is controlled based on a temperature measurement at the exit of the steam boiler, and a resistive heating wire installed on the outside surface of the steam line provides additional heat to make the steam slightly superheated. Steam mass flow rate is measured using a Coriolis flow meter on the water process side of the loop that

measures the outflux of water to a bladder tank that is being offset by the influx of steam during steady state operation. Water is pumped around the process water loop using a single speed centrifugal pump. Process water flow rate is controlled using a bypass valve around the pump and a throttle valve. Water temperature is controlled by a parallel flow heat exchanger that is cooled using building water. The temperature setpoint of the process water is maintained through a flow restriction valve on the cold water side of the heat exchanger. During testing, process water was switched from this building water to a distilled water supply in order to reduce corrosion and fouling of the test loop. A picture of the test section is shown in Figs. 9 and 10, and each major component is explained in further details in the following sections.

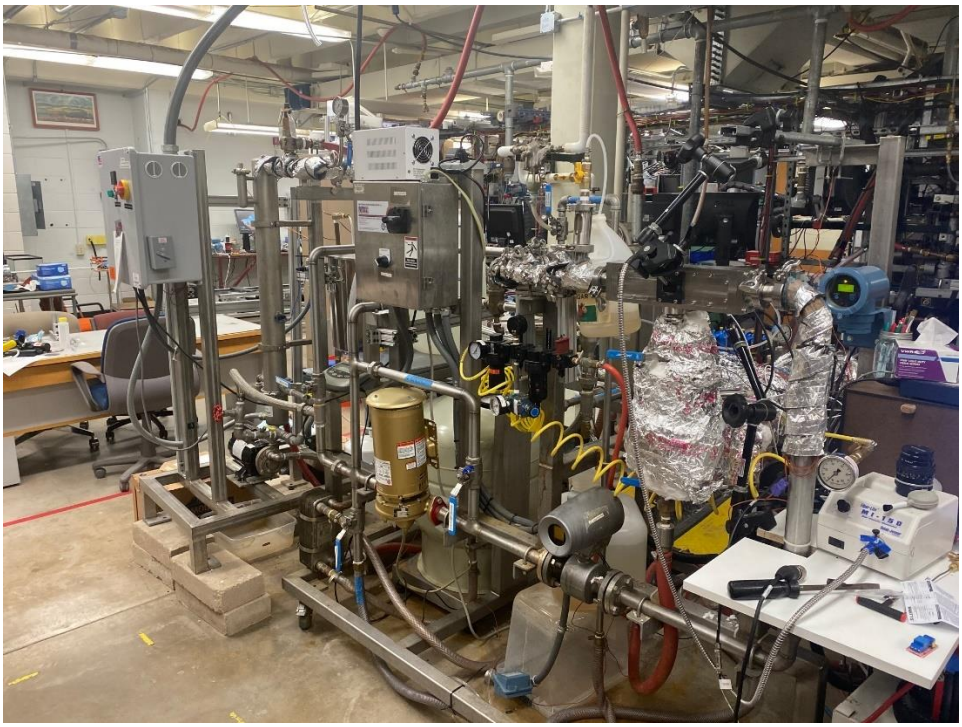

Figure 9. Front view of testing facility

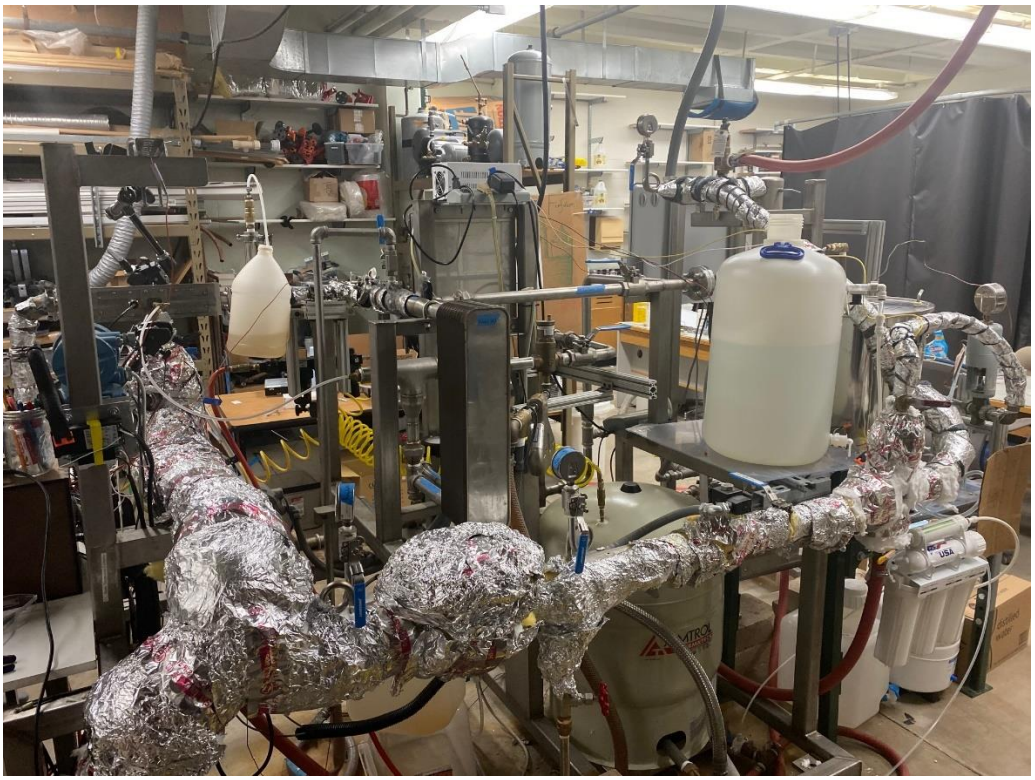

Figure 10. Rear view of testing facility

3.2 Process Collection and Processing

Process collection is defined as collecting data related to process parameters like water temperature, pressure, volumetric flow rate, or mass flow rate that are inherent to the operation of the experimental loop. These values are used to ensure that the system is at steady state and indicate any abnormalities that may occur during testing.

3.2.1 Steam Generator

An Infinity Fluids 480 V, 48 kW electric boiler is used to supply saturated steam to the experimental loop. The outlet temperature of the boiler is maintained by a PID temperature controller interfaced with a type K thermocouple. The accuracy of the thermocouple is ±1.0°C, corresponding to a saturation pressure accuracy of ±2.5 psi under normal steam injection conditions. A liquid over-pressure safety valve located at the base of the boiler opens to drain at 100 psig. The steam generator can produce steam pressures up to

95 psig, and an emergency blow off valve set to 125 psig is located at the steam outlet to exhaust excess steam to a drain stack located behind the experimental loop. A feed pump supplies water from the deaerator tank to the boiler, and a float switch at the top of the boiler maintains a nearly constant water level that completely submerges the heating coil by turning the feed pump on and off. An override switch on the boiler control panel allows manual operation of the feed pump, which is used to supply hot water from the deaerator tank to the process water loop for testing. A set of yellow ball valves switch the flow between boiler feed mode and process water feed mode. A gate valve between the boiler feed pump and the process water loop is used in order to control the pressure output from the pump. Fig. 11 shows the steam generator, boiler control panel, and feed pump valve system.

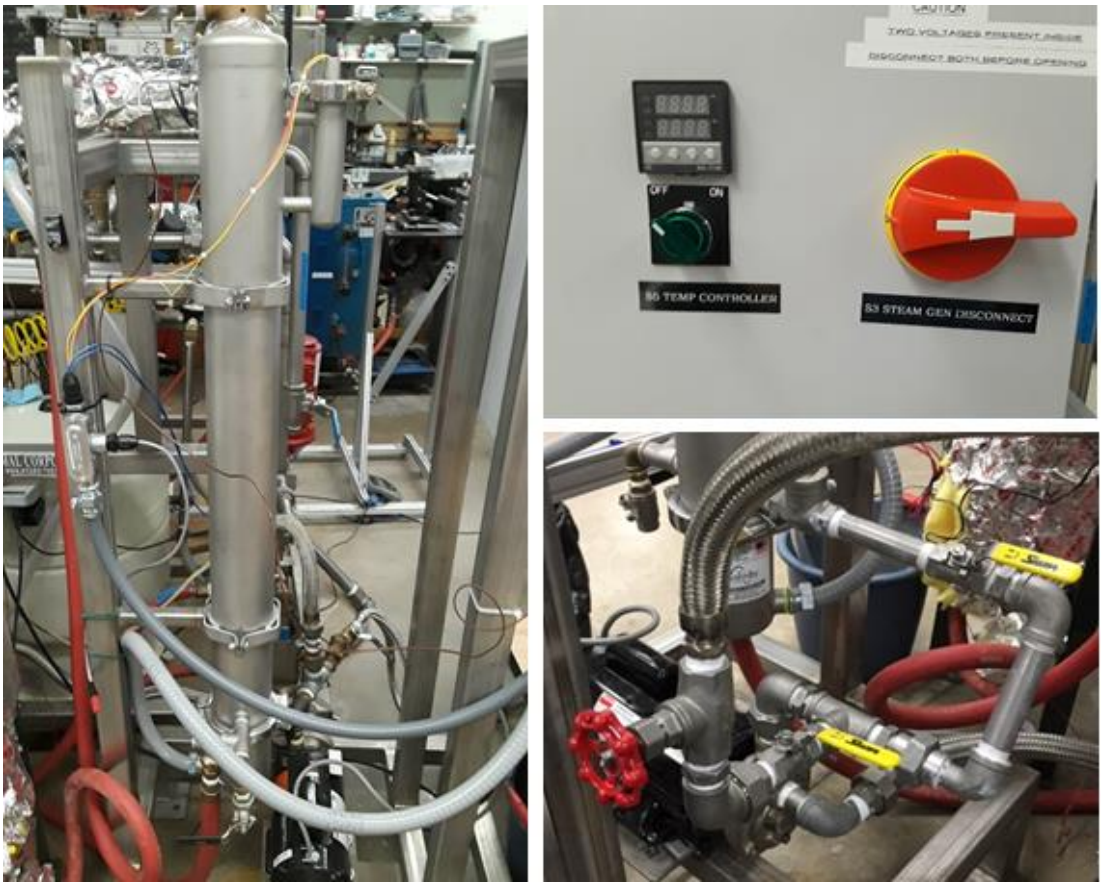

Figure 11. Steam generator system (left), control panel with temperature controller (top right), and feed pump valve control system (bottom right)

3.2.2 Steam Supply Line

Fiberglass insulation and aluminum foil covers all steam supply lines to prevent condensation and heat loss to the ambient environment. Approximately 5 feet of steam line is wrapped in 1.2 kW resistive heating wire in order to provide additional heating to superheat the steam by about 1-2°C. Insulation from this point forward is mineral wool due to the increased temperature of the heating wire. The heating wire is controlled by an additional PID temperature controller interfaced with a type T thermocouple that is in direct contact with the outer diameter of the steam supply line. The outer temperature is set to 200°C, about 35°C above steam temperature, in order to provide the 1-2°C of superheating. Ensuring that superheated vapor is entering the test section allows for thermodynamic property determination using temperature and pressure.

Because saturation temperature is set by the steam generator, the steam pressure is maintained by the generator. Steam pressure is measured just before injection using a Baumer high temperature pressure transmitter (0-1.586 MPa, ±0.25% FS). Due to the additional heating from the resistive heat wrap, a type T thermocouple (±1.0°C) is placed near this pressure transducer to measure the local thermodynamic state immediately prior to injection. The amount of superheat is calculated as this temperature reading minus the saturation temperature corresponding to the pressure reading from the transducer.

3.2.3 Process Expansion Tank and Pressure/Mass Flow Measurement

An Amtrol Therm-X-Trol ST-60V expansion tank is connected to the process water loop to maintain a relatively constant pressure in the test section over time. A compressed air supply with a pressure regulator controls the pressure inside the expansion tank. A schematic of the expansion tank is shown in Fig. 12. When the pressure in the experiment decreases below the regulator set point, air is pushed into the top of the expansion tank, increasing the pressure of the system. When the pressure of the loop rises above the setpoint or when extra mass is added to the system through steam injection, air is relieved through the pressure regulator, and the expansion tank holds the excess water. The experimental loop has

a volume of about 2 gallons. The expansion tank provides an additional volume capacity of 34 gallons, allowing for steam to be injected into a constant pressure environment for an extended period of time.

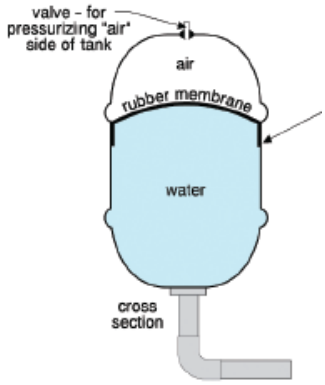

Figure 12. A cross-sectional schematic of the expansion tank used to maintain constant pressure in the experimental loop

The process water loop pressure immediately before the steam injection point is monitored by an SSI Technologies P51-100-G pressure transducer with a measurement range of 0-100 psig and an accuracy of ±1% full scale.

The steam mass flow is measured indirectly by measuring the mass flow rate of liquid water entering the expansion tank. Due to the constant pressure maintained by the expansion tank, the volume of water contained in the process loop must be relatively constant, and thus mass must also be relatively constant due to the incompressibility of the liquid water. A CMF010M Emerson micro-motion Coriolis mass flow meter with an accuracy of ±0.1% is installed on the branch leading from the process water line to the expansion tank, shown in Fig. 13. Any water that is added to the loop through steam injection must therefore pass through this mass flow meter. This method of measuring the steam mass flow works well when averaged over long periods of steady state operation of the facility. The mass flow measurement was validated by Brennan [38].

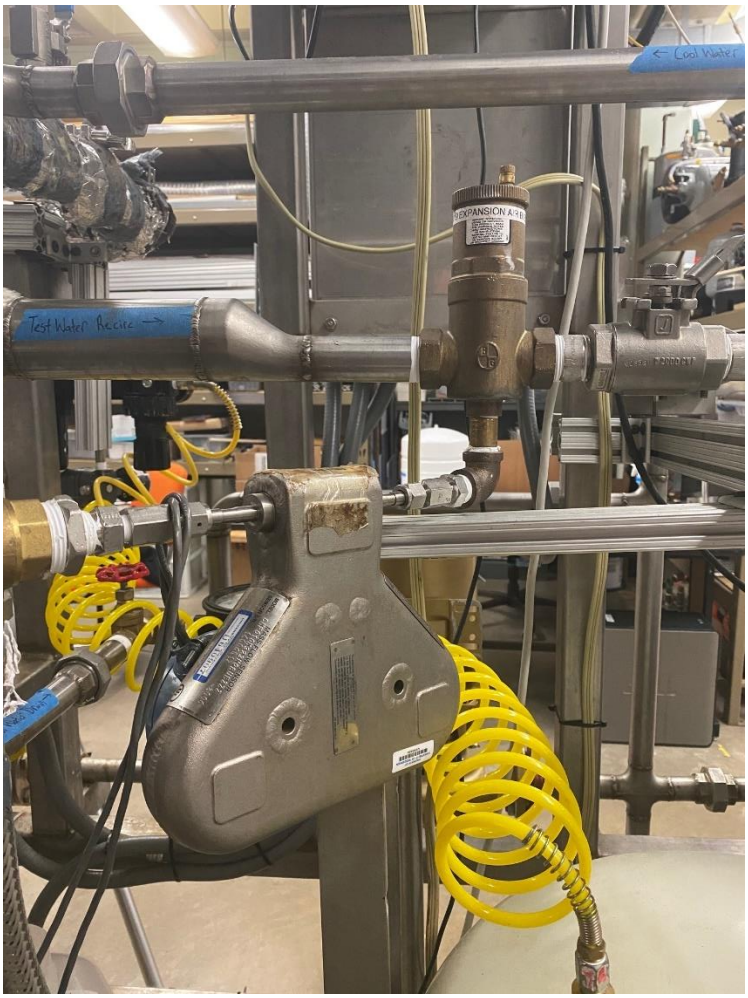

Figure 13. Mass flow meter installed on branch of process loop leading to expansion tank

3.2.4 Steam Deaerator Tank

A deaerator tank is installed before the steam boiler to remove dissolved gases from the steam line for steam injection and initial process water filling. Currently, the water is heated by a branch of the steam that is generated by the boiler. A thermostatic valve allows steam to be injected into the tank until an internal temperature of 85˚C is reached, at which point the valve will close to prevent boil-off of the tank water. The tank was previously filled with building water using a solenoid valve and float switch to maintain water level. During testing, it was found that the initial deaerator tank had significant rust damage internally. Therefore, a new stainless steel tank was installed, and only distilled water was used in the loop to prevent further corrosion. Both tanks are shown in Fig. 14.

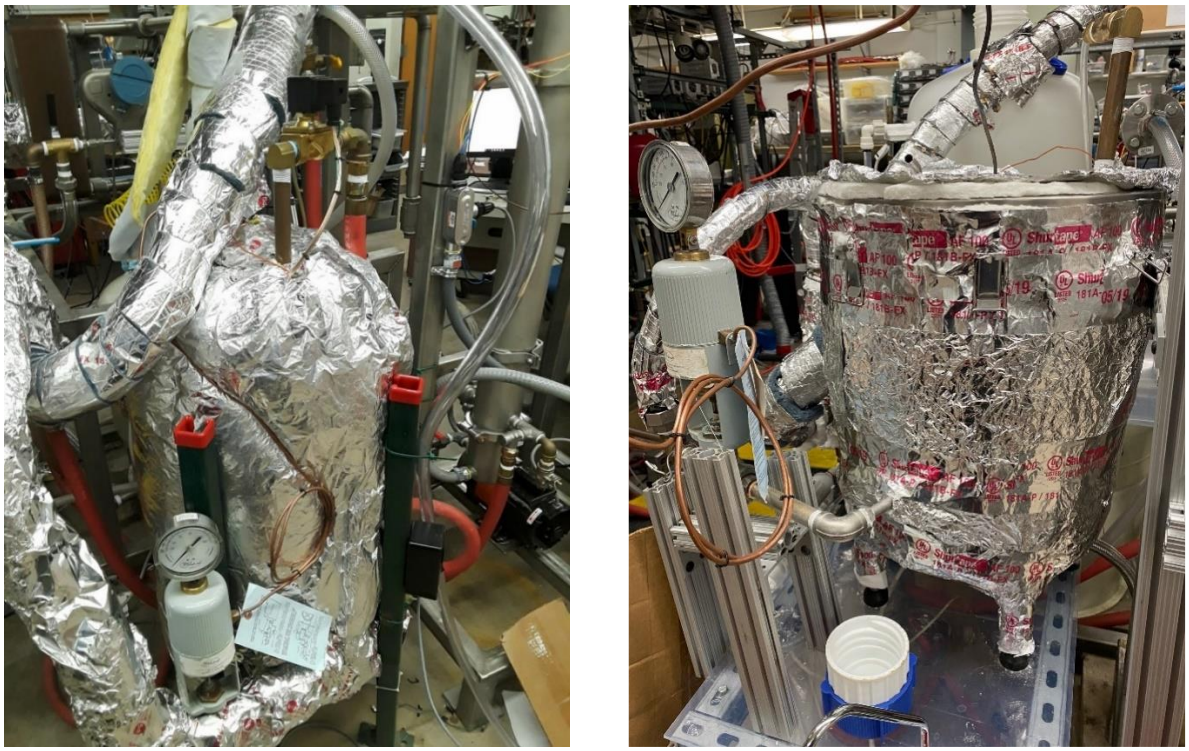

Figure 14. Initial (left) and current (right) deaerator tanks. The tanks are wrapped in insulation to further prevent heat loss to the environment.

Deaerating the water used in this experiment is important for several reasons. Removing oxygen dissolved in the water limits the amount of corrosion in the steam piping and equipment. Dissolved gases can obscure video collection and skew data processing. Published literature and studies performed by Hydro-Thermal Corporation also indicate that the amount of air in the process water has a significant effect on the stability of the condensation process and the noise. It was found during testing that steam being injected to the deaerator tank at the same time that steam is being injected into the loop had an impact on the inlet pressure of the steam. As such, the deaerator tank was heated occasionally between trials but not maintained at a constant high temperature during operation where data collection was occurring. This could be improved by insulating the tank and installing cartridge heaters that can maintain a high temperature independent of steam input.

3.2.5 Process Water Circulating Pump and Water Flow Measurement

Initially, a Bell & Gossett 90-4T centrifugal pump rated for high temperature was used to provide circulation within the test section. This pump could produce a flow rate up to 20 gal/min. During testing, it was found that the interior of the pump had significant corrosion; therefore, it was replaced with a Bell & Gossett e-90 1.25AAB centrifugal pump. A VFD had to also be installed to slow the pump speed to prevent cavitation at the outlet of the pump. With this VFD, the maximum flow rate was maintained at 20 gal/min. The flow rate for both pumps is manually controlled by a flow restriction valve and pump bypass recirculation loop. Both pumps are shown in Fig. 15.

Figure 15. Initial (left) and current (right) circulation pumps. A bypass loop runs above the pump and is the main source of flow control.

A Toshiba GF630 electromagnetic flow meter is installed at the outlet of the circulation pump to measure the process water volumetric flow rate, shown in Fig. 16. Flow meter specifications include a range of up to 75 gal/min and an accuracy of 0.2%. The lining of the water flow meter limits the maximum process water loop temperature to approximately 93˚C, but the maximum temperature for data collection is capped at 80˚C to prevent possible damage to the loop

Figure 16. Electromagnetic flow meter used for water volumetric flow rate collection

3.2.6 Process Water Temperature Control and Measurement

Process water loop temperature is maintained by a heat exchanger connected to a lab water supply line at 12-19˚C (depending on the time of year), as shown in Fig. 17. The flow rate of lab water running through the cold side of the heat exchanger is used to the offset the increase in process water temperature due to the injected steam. By manipulating this flow rate during steam injection, a pseudo-steady state can be achieved for the process water temperature. A gate valve is currently used to manually adjust this flow rate, but this system could be improved by introducing a PID control valve system based on the inlet water temperature of the test section. Two type E thermocouples with an uncertainty of ±1.7°C are installed at the before and after the visualization test section to determine inlet and outlet process water temperatures. The outlet thermocouple is located far enough away from the site of steam injection to provide complete condensation of the steam.

Figure 17. Heat exchanger used to cool process water. Process water is on the left and cooling water is on the right.

3.2.7 Process Variable Data Processing

All process conditions (steam temperature, steam pressure, steam mass flow rate, process water pressure, process water inlet and outlet temperature, process water volumetric flow rate) are acquired at 10 Hz on a NI cDAQ-9178 chassis with a NI 9207 voltage and current module and NI 9211 thermocouple voltage module for 60 seconds to ensure quasi-steady state. Because the process water temperature is the most difficult parameter to control, it is the limiting factor for steady state. Thus, steady state for data collection is defined as the process water temperature changing by less than 0.5°C from the desired temperature for a period 60 seconds.

A LabVIEW VI was created to visualize, process, and save the process data in a .csv file format. Offsets in the process data instrumentation are accounted for at the beginning of each day of data collection by referencing ambient pressure and temperature of the lab. The experimental loop is left open

to the environment overnight in order to acclimate sensors to ambient conditions by the time these offsets are taken. Ambient files with these offset values are collected each day for reference.

3.3 Visualization Test Section

A visualization test section is installed in the loop in order to record the steam plume activity during steam injection, shown in Fig. 18. The section is made of 316 stainless steel and designed for a continuous 100°C temperature exposure and 100 psig internal pressure. A flow straightener is installed at the entrance of the test section to improve the uniformity of the flow entering the steam injection site.

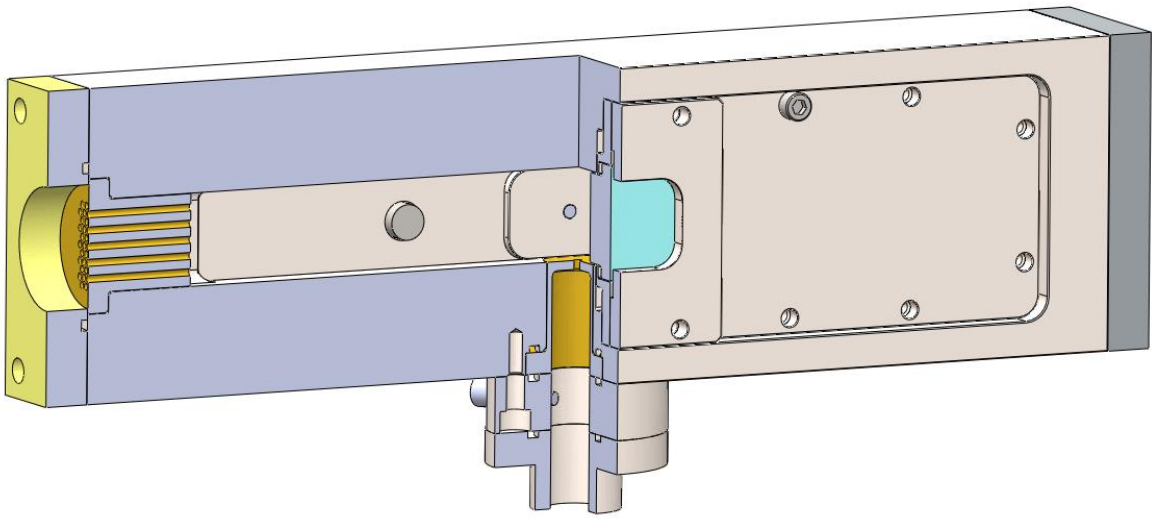

Figure 18. CAD model of the visualization test section and the site of steam injection. Superheated steam is injected vertically through a brass nozzle into a cross of liquid water traveling from left-to-right.

Previous versions of the test section were designed with both front and back windows made of fused quartz for optical access. In this version the back window is replaced with a stainless steel backplate for pressure oscillation measurements of the steam plume. The backplate was spray painted black and allowed to dry for 24 hours before installation in order to prevent reflected light from corrupting plume visualization. Oscillations induced by the unstable steam plume can still erode this coating over time.

The test section is designed to allow easy insertion and removal of brass nozzle plugs to test different nozzle geometries. An example brass plug is shown in Fig. 19. A large diameter entrance section is included before the nozzle to simulate low velocity entrance conditions. Nozzle dimensions will be explained in more detail in subsequent sections.

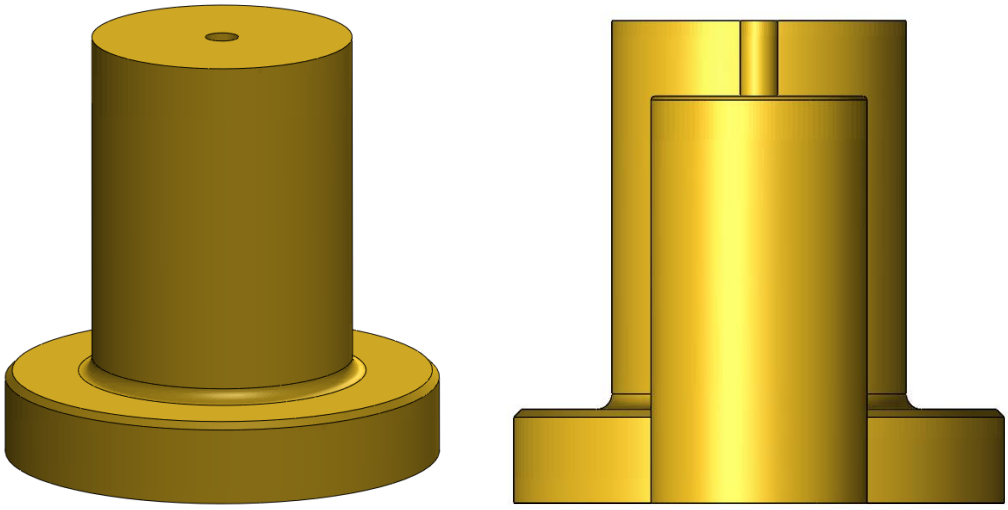

Figure 19. Example of brass nozzle plug, exterior (left) and internal (right) geometry. A large entrance region is included before the much smaller nozzle injection diameter.

3.4 High Speed Process Collection and Processing

In addition to process conditions maintained throughout the loop, three 'high speed' variables are also collected at the site of steam injection: inlet pressure oscillations, outlet pressure oscillations, and test section acoustic noise.

3.4.1 High Speed Pressure Oscillation Measurement

Pressure at the inlet and outlet of the nozzle are recorded at a higher speed than other process variables in order to determine the frequency and amplitude of pressure oscillations associated with the steam plume oscillations. A Kulite XTME-190LM-35BARA (0-3.5 MPa, ±1.0% FS) and XTM-190S-500A (0-3.45

MPa, ±1.0% FS) high speed dynamic pressure transducer is installed before the nozzle plug and in the backplate of the visualization test section, respectively. They are subsequently referred to as the inlet and outlet pressure transducers. The transducers are specifically rated for higher pressures than others in the test section and offset from the steam injection path in order to further protect them from damage associated with the pressure oscillations induced by steam instability, as shown in Fig. 20. Three pressure transducers have been overloaded and broken previously, leading to this installation technique. Due to these precautions associated with their installation, the amplitude values that are recorded should be taken as a minimum value and may be much higher at the direct site of steam injection. Two Kulite KSC-1 signal conditioners are used to amplify and filter the resultant millivolt outputs from the transducers.

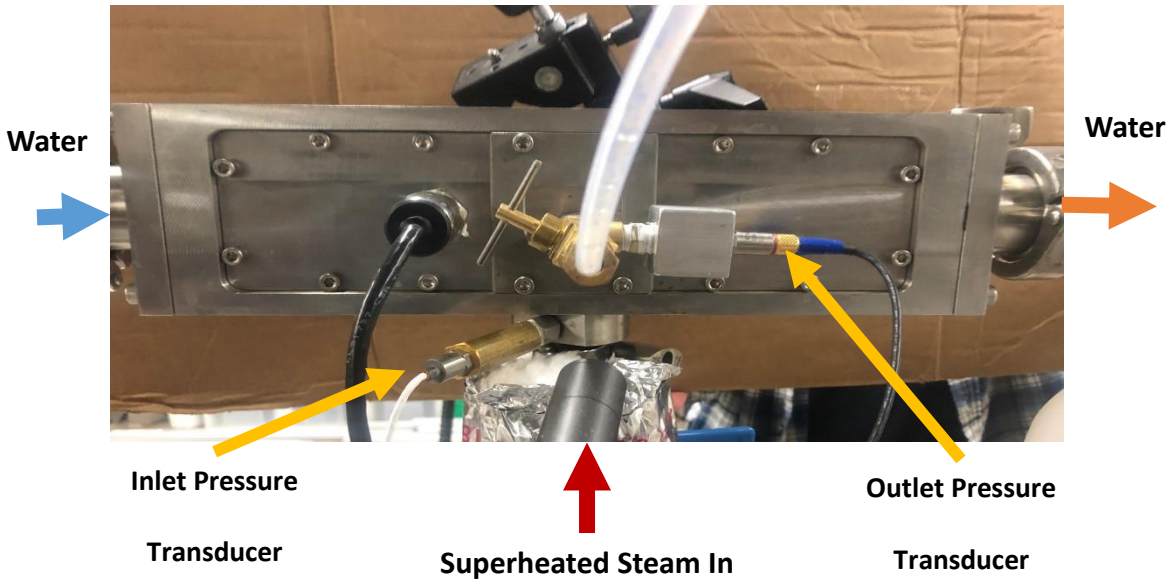

Figure 20. Locations of inlet and outlet high speed pressure transducers are offset from steam injection path to prevent damage from oscillation induced by plume instability

3.4.2 Audio Measurement

Audio data was collected using an Audio-technica AT3526 microphone and Symetrix 302 Dual Microphone Preamplifier. The microphone is placed approximately 5 inches from the test section to measure noise produced by the test section, as shown in Fig. 21.

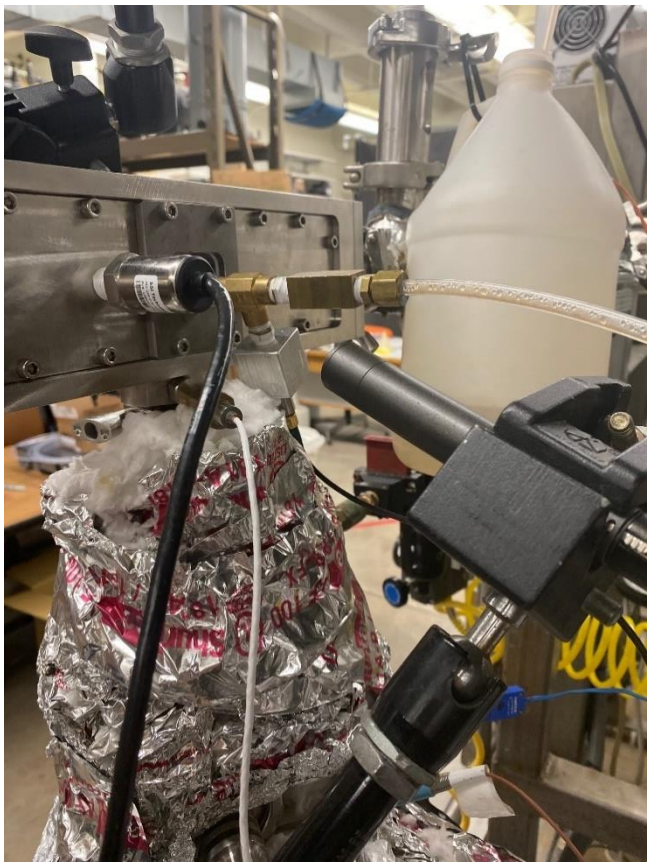

Figure 21. A microphone is placed behind the test section to record environmental noise produced by the test section

3.4.3 High Speed Data Processing

Pressure oscillation and audio measurements are collected at 40 kHz for 10 seconds on a NI cDAQ-9178 chassis with a NI 9215 voltage module. A separate .csv file is created in the LabVIEW collection program to save these data values.

During testing, it was noted that the inlet pressure transducer was significantly affected by the steam temperature. To counteract this effect, a special calibration procedure was used for this transducer. A solid nozzle plug was installed in the test section to introduce steam to the transducer without undergoing the normal oscillations of steam injection, and saturated steam conditions of 140-166°C were collected and referenced to the process steam pressure transducer. Additionally, the process water loop was used in

the calibration process. Process water pressures of 10-80 psig and temperatures of 20, 40 and 50°C were collected and referenced to the process water pressure transducer. These trials were then fit to a calibration curve using multiple linear regression with the regress function in MATLAB of the form:

$$Inlet\ Pressure\ =\ C_1V\ +\ C_2T\ +\ C_3VT + C_4$$

where V is the output voltage from the pressure transducer and T is the average temperature surrounding the pressure transducer (taken as the steam process temperature during injection). C_1, C_2, C_3, and C_4 are calibration constants, found to be 30.6859 psi/V, 66.9238 psi/°C, 0.0184 psi/(V°C), and -0.0138 psi, respectively. After this calibration, the inlet pressure was found to be accurate to ±2.1 psi of nominal pressure values. Fig. 22 shows an example of uncompensated and compensated inlet pressure measurements.

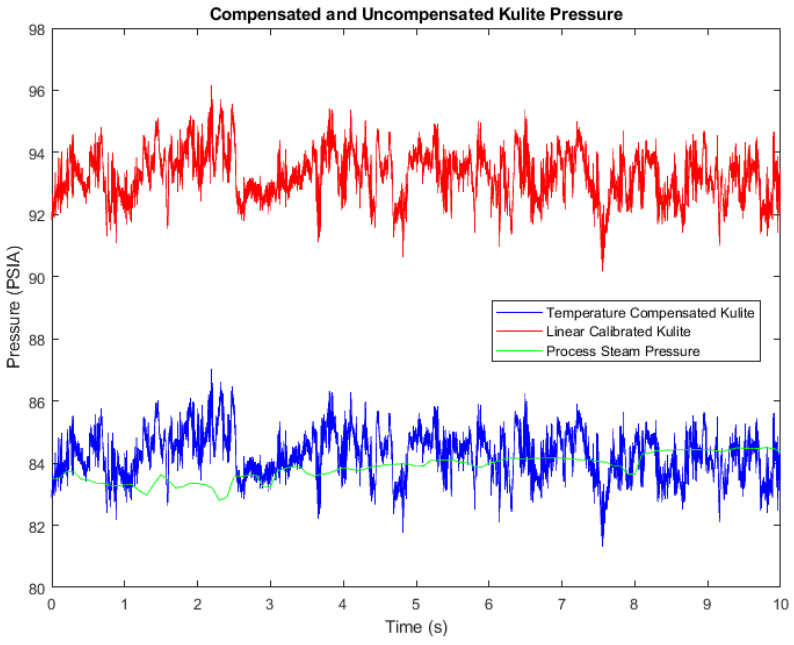

Figure 22. Uncompensated (red) and compensated (blue) high speed steam inlet pressure measurements against process steam pressure measurements (green)

3.5 High Speed Video Collection and Processing

3.5.1 Video Collection

High speed videos are collected by a Phantom V311 camera using a Phantom Camera Control software application that is specific to Phantom cameras. A Nikon Micro-Nikkor 55mm macro lens is installed on the camera to provide the best images. The V311 camera is capable of video outputs of 3 billion pixels/second. Thus, a frame rate of 3250 fps can be collected at a video resolution of 1280 x 800 pixels. Higher frame rates can be achieved at the cost of lower video resolutions. Videos were collected at 80,000 Hz for one second in order to capture at least 10 images per cycle of high frequency steam plume oscillations. This coincides with a resolution of 128 x 200 pixels.

The exposure time of each image is 11.431 microseconds. Thus, a large amount of light is needed to illuminate the plume in order to allow reasonable images with the Phantom camera. A Dolan-Jenner MI-150 Fiber-Lite fiber optic illuminator was used to focus light onto the steam plume and provide crisp images for processing. An image of the camera and fiber optic light is shown in Fig. 23.

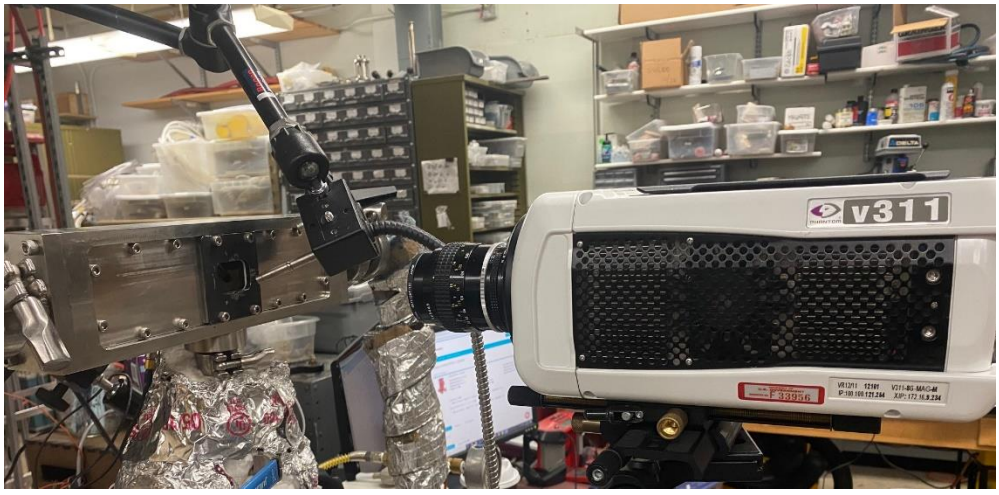

Figure 23. The Phantom V311 high speed camera and Dolan-Jenner MI-150 Fiber-Lite fiber optic cable pointed at the test section for data collection. The fiber optic cable is not turned on.

It was found during testing that the original images taken by the camera showed signs of streaking. The current session reference (CSR) option in the PCC software can be used to counteract this effect. The lens cap is placed on the camera to provide a dark environment in which all pixel intensity values should be near zero. Taking this image as the reference, any streaks that showed non-zero values were thus removed after CSR. Image qualities were much better after applying this process.

A camera trigger signal was wired to the same NI 9215 voltage module used for high speed pressure and audio measurements. While the camera is in the pre-save state in the PCC software, a voltage signal of 5V is produced by the camera. When video collection is triggered, this voltage drops to ~0.25V. Thus, pressure and video measurements can be synchronized using this change in voltage. While it was not possible to trigger camera and other data collection at the same time, this hurdle was overcome by collecting the process and high speed measurements in LabVIEW and then immediately collecting the video in the PCC software. The drop in voltage was then parsed through in the 10 second high speed data, and the time corresponding to this drop was used as the reference to sync video and pressure measurements.

Each video is output as a 3.908 GB .cine file, a Phantom proprietary file type that contains detailed information about the video capture, frame rate, exposure time, and other collection parameters. Due to this, any analysis using this file type is limited to viewing in the PCC software. Conversion to 16-bit .tif files using the batch convert function in the PCC software allows further analysis of plume images in MATLAB. Conversion can be run overnight after a day of testing in order for images to be processed the next day.

3.5.2 Video Processing

MATLAB is used to convert each high speed image into usable plume areas, heights, and widths. Since images are read as 16-bit greyscale, each pixel can have an intensity between 0 and 65,535. An intensity value of 0 corresponds to completely black while 65,535 means a completely saturated pixel. The steam plume captured in each image shows edges that decrease from bright, nearly saturated pixels to

those of zero intensity, as shown in Fig. 24. Choosing the intensity value that determines the ‘edge’ of the steam plume for analysis is open to interpretation and somewhat arbitrary. The image consists of the core steam plume with an outer mixing region of lesser intensity pixels. Determination of how much of this ‘mixing’ region is included determines the size for plume measurements.

While the intensity values of the plume may be interesting to analyze, the plume is binarized in order to collect the number of pixels that are plume rather than not plume. An intensity filter is used for this purpose to discard intensity values that fall below a certain threshold. A simple greater than logical statement is used to calculate steam vs no steam based on this threshold value.

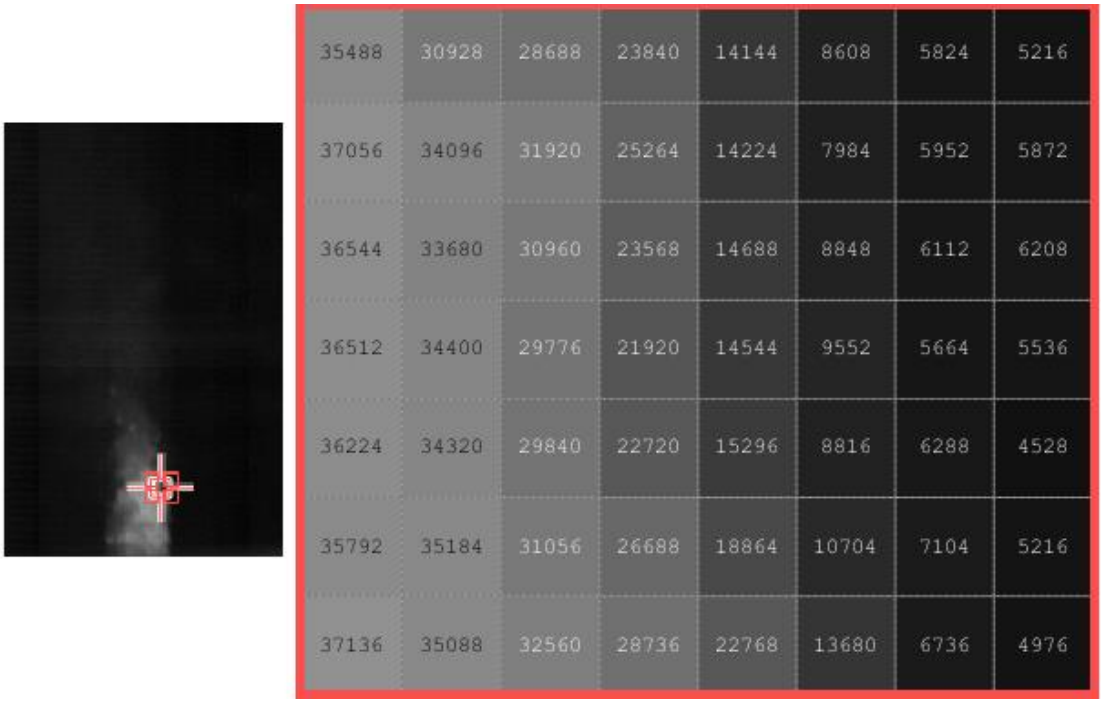

Figure 24. Intensity values shown for a representative steam plume image. Higher values correspond to brighter pixels.

Because lighting and camera position may change between tests, a percentage threshold value is used rather than one that is an absolute value. This approach alleviates the bias where images with better lighting may have larger calculated plume areas. A threshold percentage of 30% is used for the data reported here. In order to determine the threshold value based on this percentage, the first plume image is

extracted to determine the minimum and maximum intensity values that are present in the image. The corresponding absolute threshold value is then:

$$Threshold\ value = Min\ Image\ Intensity + 0.3 * (Max\ Image\ Intensity - Min\ Image\ Intensity)$$

The converted image will therefore look like the one shown in Fig. 25.

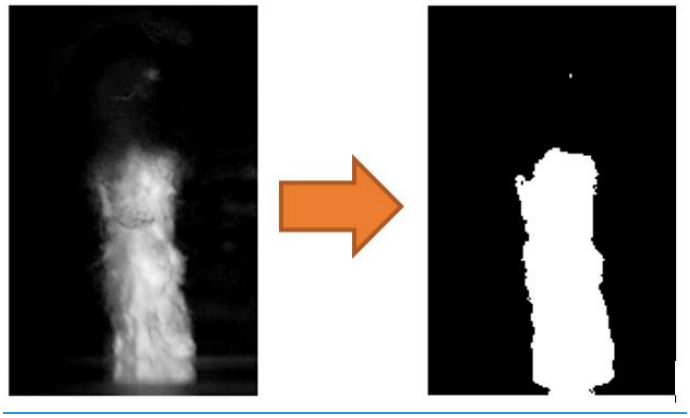

Figure 25. A raw steam plume image before (left) and after (right) thresholding

The MATLAB nnz function then counts the amount of nonzero values in the image. Using the entire image array, the steam plume area can be computed. Examining only certain rows or columns will result in plume widths or heights, respectively. These measurements, however, are in terms of pixel number rather than any physical unit.

In order to compare images between trials on different days, a scaling factor needs to be introduced based on an artifact of known distance located in the viewing frame. The backplate hole leading to the outlet pressure transducer which has an inner diameter of 0.188 inches was chosen as this artifact for testing, as shown in Fig. 26. This reference image is collected at the end of every data collection day and input into FIJI/ImageJ in order to determine the scaling factor. A circle overlay is fit to the image and added as a selection for measurement. The Feret diameter, an image processing measure similar to measuring the diameter of an object physically with a caliper, is then computed from this circle overlay,

providing the number of pixels corresponding to this inner diameter, shown in Fig. 27. The image scaling factor is thus this value divided by 0.188 inches. Typical scaling factors obtained this way for different trials range from 215 to 300 pixels/inch. Plume heights and widths are found by dividing the number of pixels found by this scaling factor while plume area is found by dividing the number of pixels by this scaling factor squared. While it is assumed that the plume is quasi-axisymmetric, plume volumes are not computed.

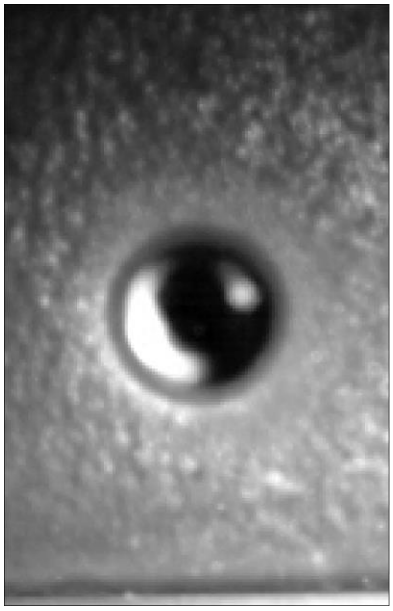

Figure 26. Hole in the test section backplate leading the outlet pressure transducer. This is usually not seen when running at higher frame rates.

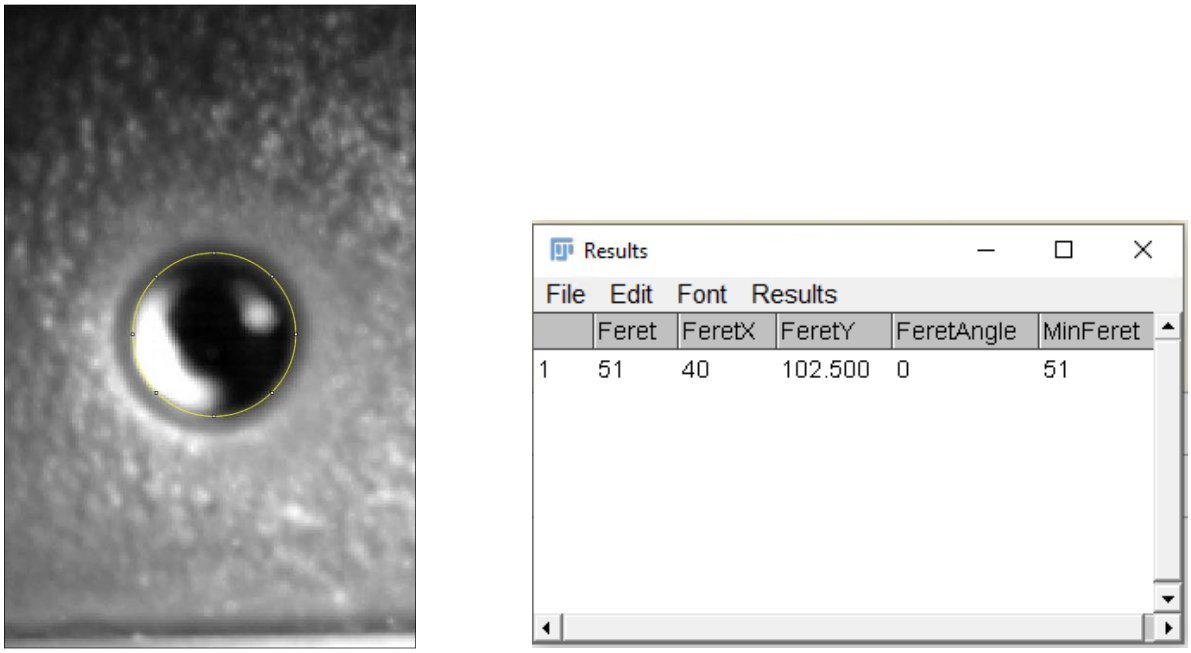

Figure 27. The circle overlay placed around the inner diameter in FIJI (left) and the corresponding Feret diameter calculated by FIJI (right)

3.6 Power Spectral Density Analysis

The important measured characteristics of plume area and pressure oscillations are the spectral content, specifically the amplitudes and frequencies at which they occur. This can be traced back to physical phenomena in the plume that may be tied to large (potentially damaging) amplitudes or to frequencies close that might be to the natural frequencies of equipment in the process line. The power spectral density (PSD) of the plume measurements, pressure oscillations, and audio signal is performed using the pwelch function in MATLAB with default window and overlap values. This function estimates the mean-square value per frequency of these signals normalized to a single hertz bandwidth, determining the frequencies that dominate above the noise level of the signal. It is best used to characterize broadband random signals, allowing signals to be compared independent of spectral resolution.

PSDs are reported using the decibel scale for easy visualization of data. The decibel scale is computed as:

$$dB = 10 * \log_{10} \frac{P_{value}}{P_{ref}}$$

where dB is the decibel scale value, P_{value} is the unscaled output value of the PSD, and P_{ref} is a reference value for scaling purposes, used here as $10^{-12}\ \frac{in^4}{Hz}$, $10^{-6}\ \frac{kPa^2}{Hz}$, and $20^{-6}\ \frac{V^2}{Hz}$ for the image area, pressure oscillation, and audio signal, respectively. The PSD is also adjusted for noise in the signal by smoothing the spectrum using a 200 point moving average with the 'rloess' method in MATLAB. The 'rloess' method is especially useful in that it removes significant outliers, preventing them from corrupting the spectrum smoothing method. The spectral resolution for pressure and audio measurement is 0.1 Hz, and the image spectral resolution is 1 Hz. These resolutions are much smaller than the separation between of peaks seen in spectrum.

In order to determine if a peak meets significance, the findpeaks function is used in MATLAB with a minimum prominence value of 3 dB, corresponding to roughly at least a doubling of power in the signal from the peak to the surrounding values in the PSD. A measure of the prominence of a peak could also be used to determine whether a peak is a sharp or broadband noise in the signal, but this is not explored here.

3.7 X-ray Scanning of Nozzle Geometry

All nozzles discussed in this work are examined by a 450 kV industrial x-ray system at the University of Wisconsin – Madison to better understand and visualize the internal geometry of the nozzle. The x-ray system was built by VJ Technologies (Bohemia, NY) and includes a 1500 W Comet x-ray source, a 1621 Perkin-Elmer scintillation detector, and a rotating stage to facilitate computed tomography scans. The detector has 2048 x 2048 pixels which are energized over an "integration period" chosen by the operator. Several frames are collected before the stage rotates to the next position. Frame averaging reduces noise from x-ray scatter and thus enhances the clarity of the image.

The nozzles are positioned between the source and detector such that each pixel on the detector captures x-rays passing though roughly a 90 x 90 micron area of the nozzle. The voxel size, defined as the

size of each 3-D volume element in the CT reconstruction, is thus approximately 90 microns. Earlier studies with components in a similar scan configuration to the steam nozzles revealed CT image resolution/repeatability to be 120 microns per the ASTM 1695 - E qualification procedure.

Each nozzle scan takes 45 minutes. The full energy and fluence of the x-ray tube is utilized. The x-ray beam is hardened by an 1/8 inch of copper plates placed in front of the tube's aperture. Beam hardening shifts the energy spectrum to higher energies, which reduces scatter caused by low-energy x-rays. Each frame is integrated/captured for 500 ms, and 8 frames are averaged together before the stage moves to the next position. 800 projections are obtained by rotating the stage 0.45° after averaging eight of the detector captures.

Fraunhofer Institute's Volex software was used to capture the projections and reconstruct these projections into a 3-dimensional dataset. At this point, the reconstruction is imported into Volume Graphics Studio Max 3.4 for viewing, volumetric manipulation, and measurement of internal geometry.

4. Regime Classification

There have been many naming conventions used to describe the different regimes in the pathway of steam condensation instability. Some are direct definitions of the overall shape of the plume, such as conical, hemispherical, or cylindrical. Others characterize what is happening to the plume over time, such as condensation oscillation or chugging. According to the literature, each regime occupies a region of water temperature and steam mass flux (or other parameters, if they are explored). Changing the temperature or steam mass flux will thus cause the steam plume to enter a new mode of steam injection. Typically, higher water temperatures and lower steam mass fluxes result in more unstable regimes. Synthesizing these definitions and observations and applying them to the plume observed in the experimental facility leads to four regime definitions proposed here: stable, condensation oscillation, unstable, and transition. Rather than mapping each regime by water temperature and steam mass flow,

here the regimes are mapped against water temperature and nozzle pressure ratio (exit pressure/inlet pressure). Each of these regimes will be described in detail below.

4.1 Stable Condensation Regime

The stable condensation regime typically occurs at low process water temperatures and low nozzle pressure ratios. This regime is the most desirable one because noise is relatively low due to the low pressure oscillations as the plume condenses smoothly into the process water. An example of a time trace of a stable steam plume is shown in Fig. 28. The steam plume tends to form a conical shape with small fluctuations along the edges. These fluctuations are not considered significant when considering the shape of the plume.

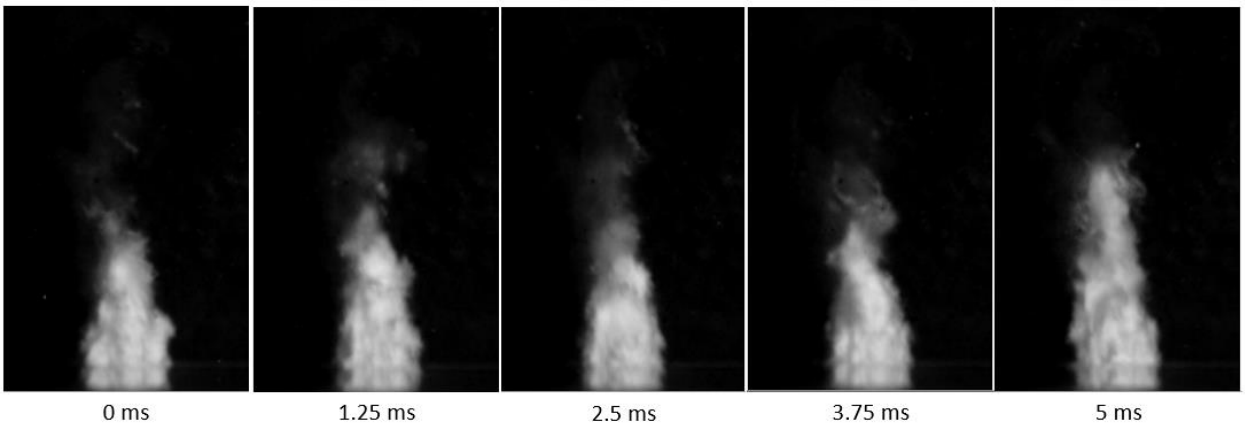

Figure 28. Stable steam plume undergoing direct contact condensation. The shape of the plume does not change significantly over time.

4.2 Condensation Oscillation Regime

When the steam plume approaches the instability point, the fluctuations within the plume become greater and the shape of the plume becomes less uniform. This transition can be accomplished by increasing the process water temperature or by increasing the pressure ratio of the system. These fluctuations smoothly increase on the path to instability. As such, it is sometimes hard to establish the

proper and precise boundary between stable condensation and condensation oscillation due to the somewhat arbitrary definition of what ‘significant fluctuations’ entails.

The boundary between condensation oscillation and the next regime, unstable, is much more distinct, except in cases where the transition regime comes into play. Later in the condensation oscillation regime, large waves form along the plume, coalescing into bubbles that do not ‘pinch’ away from the main plume. Unstable condensation is defined as the condition when these waves finally ‘break’. As such, the condensation oscillation regime may be described as a plume that is reacting violently to condensation yet still retaining a single, continuous shape, as shown in Fig. 29.

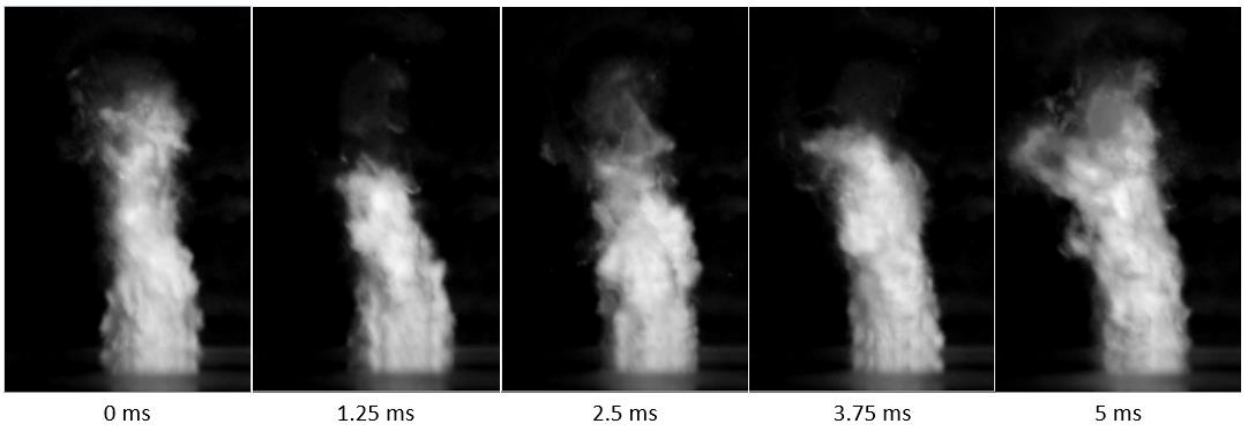

Figure 29. Steam plume undergoing condensation oscillation. The plume increases in size and does not maintain a consistent shape. The plume however is still a single, continuous structure.

4.3 Unstable Condensation Regime

The unstable condensation regime is both the most chaotic and most interesting regime. The single, continuous structures seen in the stable condensation and condensation oscillation regimes finally break down and diverges into a highly time-varying system involving the rapid formation and breakdown of bubbles from the main steam plume. Typically, this regime is encountered at high water temperatures where the degree of subcooling is very low or at high pressure ratios above the critical pressure ratio of

0.546 for superheated steam. The unstable condensation this regime produces a high and very unpleasant screeching noise and causes severe pressure oscillations that can pose a safety hazard for workers and process equipment alike. It is necessary to wear hearing protection in order to collect trials in this regime. Fig. 30 shows the process of many bubbles forming and collapsing in the unstable regime.

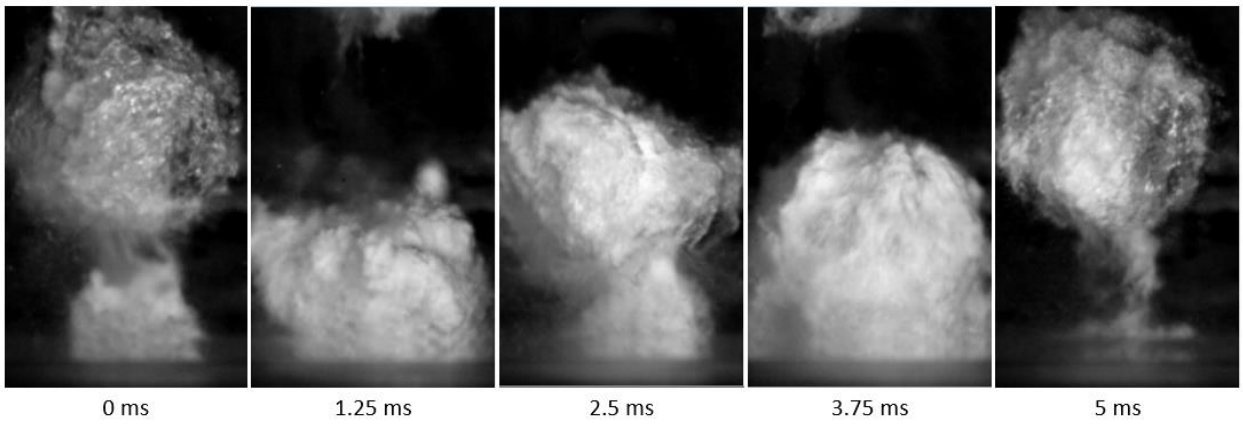

Figure 30. Steam plume in the unstable regime. Note that this is not a single bubble, but many forming and collapsing over this time period.

4.4 Transition Regime

While the steam plume transitions from condensation oscillation to unstable condensation, the plume will sometimes pull out of the bubbling of the unstable regime and return to the single, severely fluctuating plume associated with the condensation oscillation regime. This ‘flip-flopping’ as it was previously described by a previous grad student [38] is the defining trait of the so-called transition regime. The number of transitions can range from multiple times a second, to just once or twice a second, to situations where the time between transitions is longer than the second of video captured. It is still unknown why the plume can go into and out of the unstable regime during this time period. An example of this switching is shown in Figure 31.

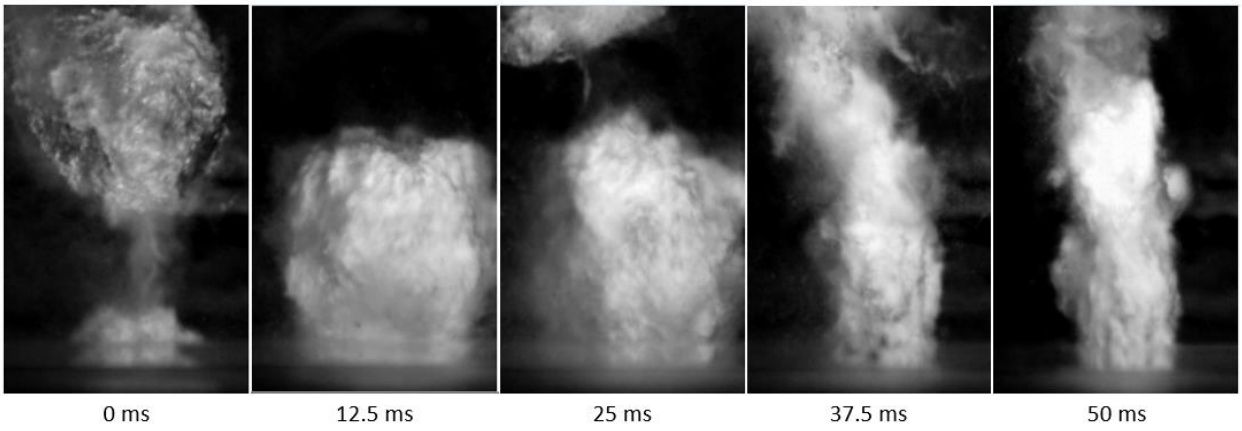

Figure 31. Steam plume undergoing the transition regime between unstable (left) and condensation oscillation (right). Note that the time shown is much longer than other examples due to the longer time between transitions.

4.5 Comparison to Literature Regimes

Many regime definitions have been proposed in the literature, and it is sometimes hard to consolidate them into a cohesive naming convention. The four definitions proposed above help establish the behavior observed for the specific nozzles that are used in the experimental facility. In order to better define these regimes relative to those proposed in the literature, Appendix B explores how literature regime definitions would map onto these four regimes.

5. Baseline Geometry Analysis – 1S Nozzle

The baseline geometry for the plume stability analysis is a simple straight-bore nozzle with an inner diameter of 0.096 inch. The length to diameter (L/D) ratio of the nozzle is maintained at 1 in order to compare results to those found by previous grad student Max Brennan [38]. This set of geometric parameters are also consistent with those used in the project sponsor's industrial process heating applications. This nozzle is referred to as the 1S nozzle for being a 'straight' nozzle (S) with a L/D ratio of 1. A schematic of the nozzle is shown in Fig. 32.

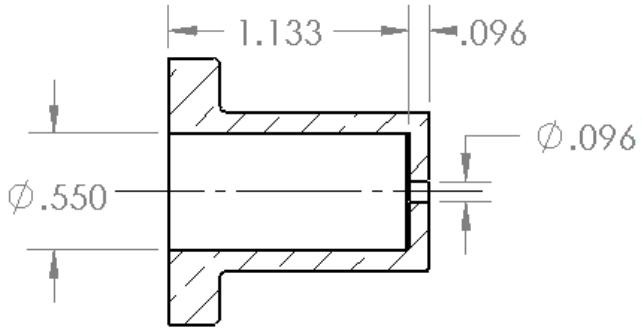

Figure 32. Schematic of the '1S' nozzle (all dimensions are in inch)

Data was obtained over a range of process water temperatures at a pressure ratio of 0.472 (water pressure = 25 psig, steam pressure = 70 psig) and a fixed process water flow rate of 15 gpm; data was collected from 25 to 80°C in increments of 5°C.The nozzle is expected to encounter all of the previously discussed regimes within this range as the temperature is increased. PSDs of the steam plume area and outlet pressure suggest that the dominant frequencies associated with the plume shape oscillation depend on the regime associated with the process. As the temperature of the process water is increased, the magnitudes of these oscillations increase while the dominant frequencies tend to decrease.

5.1 Stable Regime

The 1S nozzle remains within the stable regime from 25°C until about 50°C. Due to the fact that the stable regime is classified by minimal fluctuations in the steam plume, the dominant frequencies in this regime do not exhibit sharp peaks and have more of a broadband structure in the 5000-7000 Hz range for the steam plume area; the center of this frequency band lies between about 5400-6650 Hz. These stable plume oscillations are mostly associated with variations in the width of the plume near its tip as well as fluctuations in the plume height. These frequencies likewise shown up in the outlet pressure PSD with the same relative intensity as the oscillations of the plume. An example of the steam plume area and outlet PSD is shown in Fig. 33.

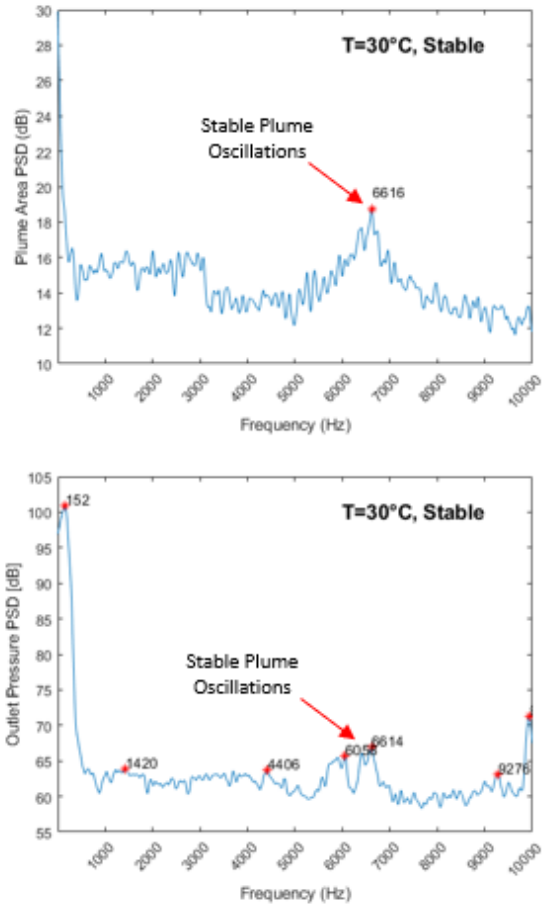

Figure 33. Steam plume oscillations (top) and resultant outlet pressure oscillations (bottom) of a stable steam plume

5.2 Condensation Oscillation Regime

When the process water approaches about 50°C, the plume fluctuations start to increase in intensity and reduce in frequency, as shown in Fig. 34. These fluctuations are typically between 3600-4500 Hz and can be attributed to the more severe fluctuations noticed in the steam plume as it contracts and expands during the condensation process, here called the primary plume width oscillations. Another peak of higher frequency shows up starting around 60°C and is centered around 7800-8400 Hz; these peaks are related to fluctuations closer to the tip of the plume, here called the secondary plume width oscillations. When

looking at the outlet pressure PSD, these primary plume width oscillation frequencies likewise show up with a sharp intensity, but the secondary plume width oscillations do not show up with the same intensity.

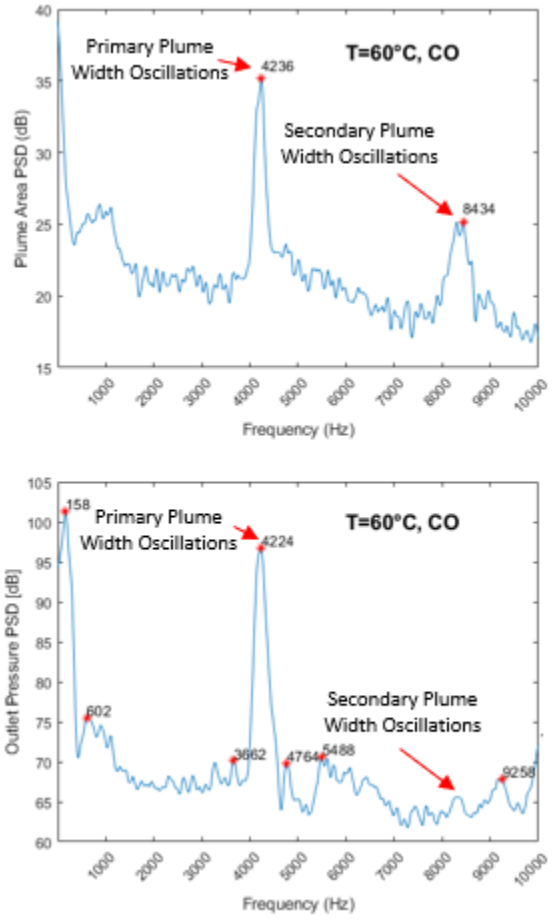

Figure 34. Steam plume oscillations (top) and resultant outlet pressure oscillations (bottom) within the condensation oscillation regime

5.3 Transition Regime

Once the process water reaches approximately 70°C, the steam plume undergoes the 'switching' from condensation oscillation to unstable and back that is characteristic of the transition regime. The spectral content of the outlet pressure and steam plum area becomes very rich at this point, as shown in Fig. 35. Since two regimes show up, some features of both show up in the power spectral density plots. Major frequencies found in this regime include 1070 – 1470 Hz, 1890 – 2960 Hz, and 3480 – 3740 Hz.

Frequencies between 1000 – 3000 Hz can be attributed to the formation and destruction of bubbles while the plume is unstable. The 1070 – 1470 Hz frequencies are attributed to the formation of so-called ‘double bubbles’ in which one bubble formation is rapidly followed by a successive bubble that absorbs the first bubble and then breaks down. The higher frequency of 1890 – 2960 Hz is caused by the formation and breakdown of a single bubble on the video screen. Frequencies of roughly 3500 - 4000 Hz remain and are associated with the primary plume width oscillations associated with the condensation oscillation regime. Examination of the associated outlet pressure measurement shows pressure oscillations at the outlet of the nozzle that are near the bubble formation and breakage frequency of 1900 Hz and the primary plume oscillations of 4000 Hz involved with the transition regime.

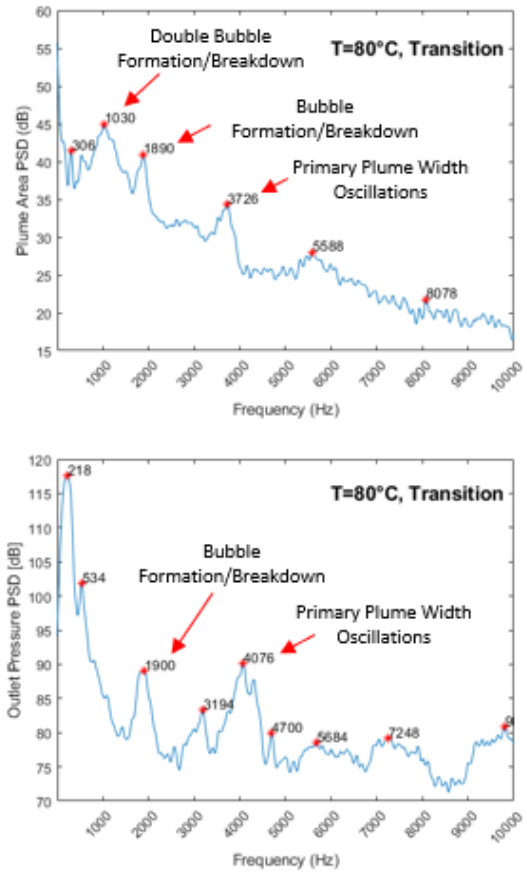

Figure 35. Steam plume oscillations (top) and resultant outlet pressure oscillations (bottom) within the transition regime

5.4 Pathway to Instability

Figures 36 and 37 show the pathway to instability of the 1S nozzle as the process water temperature is increased. High frequencies are observed when the plume is stable, but these frequencies shift lower and lower as the next regime is approached. Likewise, peak amplitudes and broadband noise increase continuously as instability is approached. It can be inferred from this trend that, as the steam condensation becomes more unstable, the plume area fluctuations grow and the frequencies associated with this oscillation will decrease until they reach unstable values.

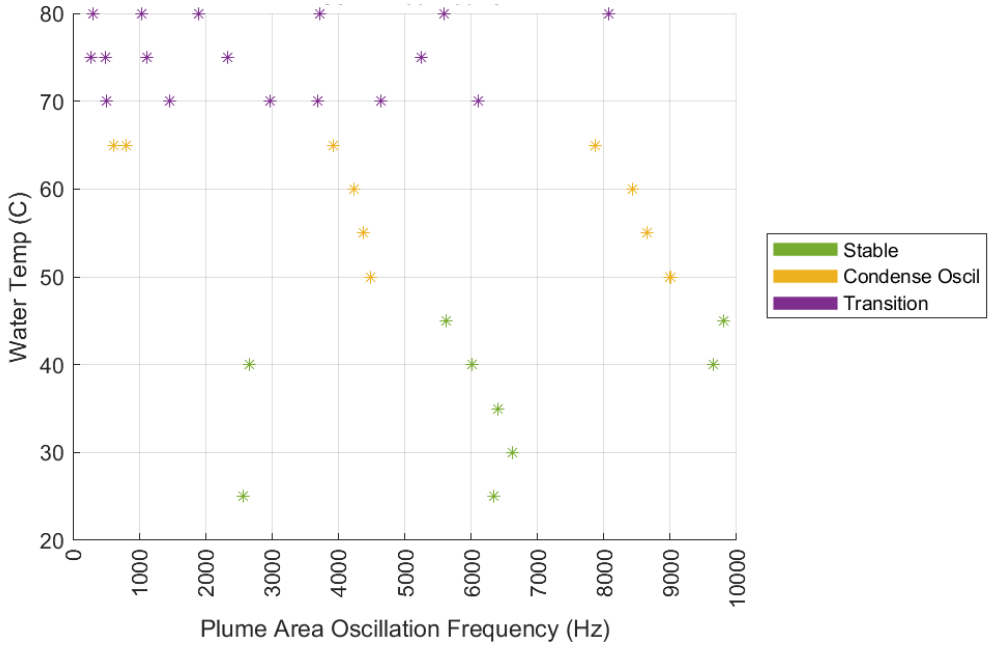

Figure 36. Map of major 1S plume area frequencies as a function of process water temperature. The dominant frequency of the stable and condensation oscillation regime decreases until a burst of frequencies appear in the transition regime.

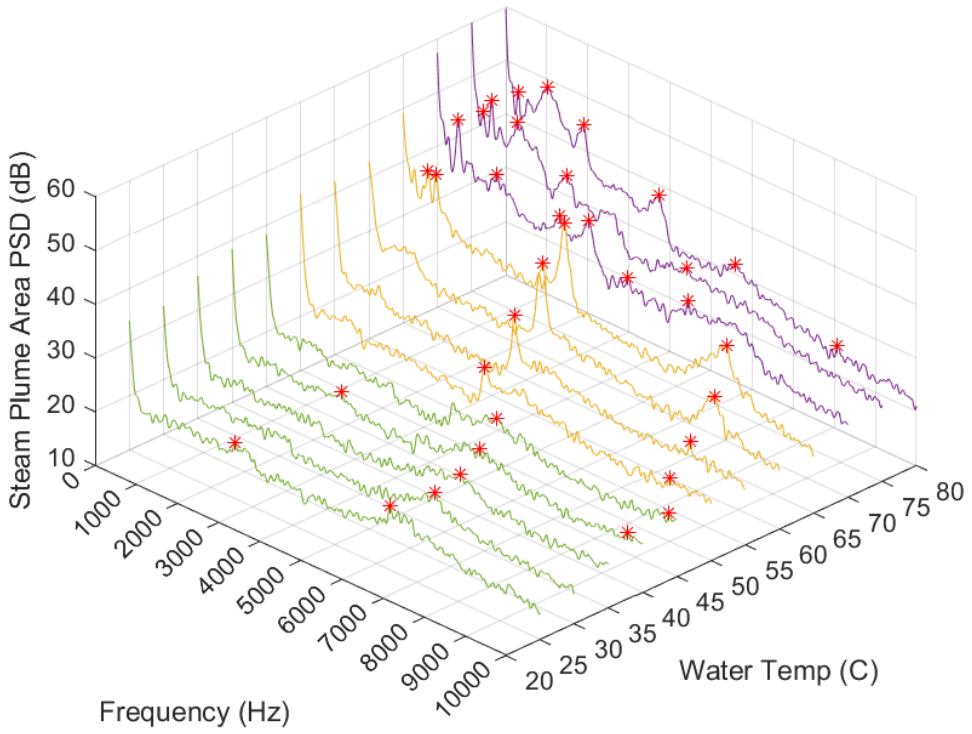

Figure 37. Waterfall plot of the 1S plume area PSD as a function of water temperature at a pressure ratio of 0.472 (water pressure = 25 psig, steam pressure = 70 psig). Green is the stable regime, yellow is the condensation oscillation regime, and purple is the transition regime. Frequencies follow a decreasing trend while amplitudes increase as water temperature is increased.

5.5 Oscillation Frequencies as Compared to Literature

Other researchers have attempted to circumvent the problem of differing injection parameters and environments by proposing predictive correlations for the dominant frequencies encountered during the condensation process. These predictive correlations are compared to the measured plume oscillation frequencies for the 1S nozzle, described in the previous section. Researchers have provided predictive correlations for the frequencies generated by plume oscillations, referred to as the first dominant frequency [27], as follows:

Damasio et al. [25]:

$$St = 0.001196 \cdot (Ja)^{1.0849} \cdot (Re)^{0.9389} \cdot (We)^{-0.767} \quad (1)$$

Simpson & Chan [24]:

$$St = 0.011 \cdot (Ja)^{0.72} \cdot (Re)^{0.25} \quad (2)$$

Arinobu [1]:

$$f = \frac{800 \cdot V}{d_e} \cdot \left[\frac{c_p \cdot \Delta T}{h_{f_g}}\right]^{1.4} \quad (3)$$

where *St* is the density weighted Strouhal number, $f d_e \rho_l / (\rho_s V)$, f is the plume oscillation frequency, d_e is the exit diameter of the injection nozzle, ρ_l is the density of the water, ρ_s is the density of the steam, and V is the exit velocity of the nozzle. *Ja* is the Jacob number, $\rho_l c_p \Delta T / \left(\rho_s h_{f_g}\right)$, ρ_l and ρ_s are defined previously, c_p is the heat capacity of the water, ΔT is the degree of subcooling of the water, and h_{fg} is the latent heat of vaporization of the water. *Re* is the steam Reynolds number, $\rho_s V d_e / \mu$, where ρ_s, V, and d_e are defined previously and μ is the viscosity of the steam. *We* is the Weber number, $\rho_s V^2 d_e / \sigma$, where ρ_s, V, and d_e are defined previously and σ is the surface tension of the water.

Experimentally measured plume oscillation frequencies (connected by solid lines) and the associated predicted frequencies (connected by dashed lines) at the same test conditions are shown in Fig. 38 as a function of water temperature. All predictions fall well below the experimental results.

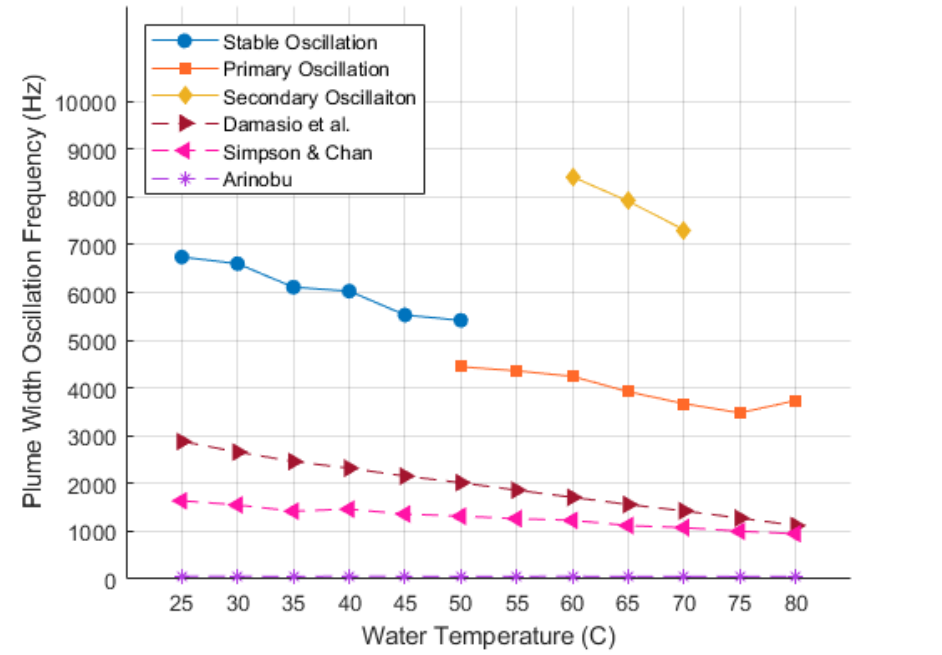

Figure 38. Comparison of experimental and predictive frequencies of plume width oscillations (data are connected by solid lines while predictions are connected by dashed lines)

Correlations have also been suggested for the bubble formation and breakdown frequency, referred to as the second dominant frequency [27]:

Qiu et al. [27]:

$$St = 2.2 \times 10^{-6} \cdot (Ja)^{0.94} \cdot (Re)^{3.19} \cdot (We)^{-2.92} \tag{4}$$

Chong et al. [29]:

$$\mathrm{f} = \frac{1}{2 \cdot \pi R_0} \sqrt{3 \cdot \mathrm{n} \frac{P_l}{\rho_l}} \tag{5}$$

Chen et al. [30]:

$$St = 2.2 \times 10^{7} \cdot (Ja)^{0.44} \cdot (Re)^{-1.21} \cdot (We)^{-0.14} \cdot \varepsilon^{-0.61} \tag{6}$$

where the parameters *St*, *Ja*, *Re*, and *We* are defined as previously, with *f* now being the bubbling frequency. ε is additionally the absolute pressure ratio, P_l/P_s, P_l is the water pressure, P_s is the steam pressure, *n* is the

polytropic index (here taken to be isentropic), and R_o is the initial bubble radius (here taken to be the largest bubble radius).

As shown in Fig. 39, the predictions of Qiu et al. [27] and Chong et al. [29] are consistent with experimentally measured frequencies, but the prediction from Chen et al. [30] differs significantly. The correlations tend to match the "double-bubble" frequency more closely than the frequency associated with a single bubble formation and breakdown. It is unclear, however, if these predictions are meant to match this double bubble frequency, since this phenomenon was not mentioned by the authors.

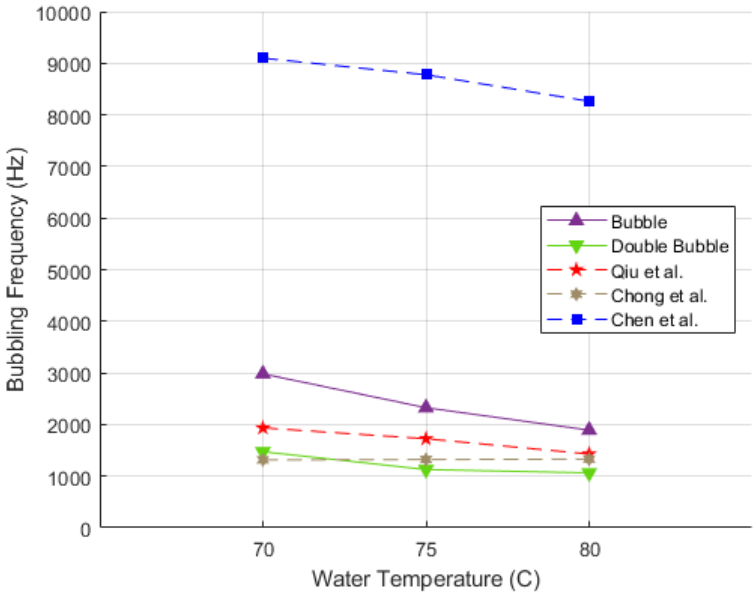

Figure 39. Comparison of experimental and predictive frequencies of bubbling frequencies

Table 1 summarizes the testing environments that were used to develop the correlations. Notice that all predictions were performed in stagnant pools with nozzle diameters larger than the one under study and at smaller steam mass fluxes. This change in environment could be a source of error in the predictions.

Table 1. Comparison of injection environments for predictive correlations in the literature. The last row is the injection environment for results reported in this thesis.

Authors	Injection Environment	Steam Jet Orientation	Nozzle Diameter [mm]	Water Temp [C]	Steam Mass Flux [kg/m*s]
Arinobu [1]	Stagnant	Vertical downward	16.1, 27.6	20-92	5-100
Damasio et al. [25]	Stagnant	Vertical downward	6, 8, 10, 12	25-75	0-250
Simpson & Chan [24]	Stagnant	Vertical downward	6.35, 15.9, 22.2	25-65	147-333
Qui et al. [27]	Stagnant	Horizontal	8	20-70	186-865
Chong et al. [29]	Stagnant	Horizontal	8.1	20-60	400-800
Chen et al. [30]	Stagnant	Horizontal	CD Nozzle: D_{cr} = 8, D_e = 8, 8.8, 10.4, 12	20-65	400-800
Alden	Crossflow	Vertical upward	2.4	25-80	600-1000

6. Length/Diameter Ratio Study – 1S, 2S, 3S Nozzles

To compare the effect of nozzle geometry on plume stability, an initial study of L/D ratios of 1, 2 and 3 was carried out using straight nozzles. The results suggest that a L/D ratio of 2 is the best in terms of stability. Image scans of the internal geometry of the nozzle also highlight slight differences between nozzles that may also affect the pathway to instability.

6.1 2S Nozzle

A simple straight-bore nozzle with an inner diameter of 0.096 inch was tested that has a length to diameter (L/D) ratio of 2 (i.e., it has the same diameter as the 1S nozzle but the straight section is twice as long). This nozzle is referred to as the 2S nozzle for being a ‘straight’ nozzle with a L/D ratio of 2. A schematic of the nozzle is shown in Fig. 40.

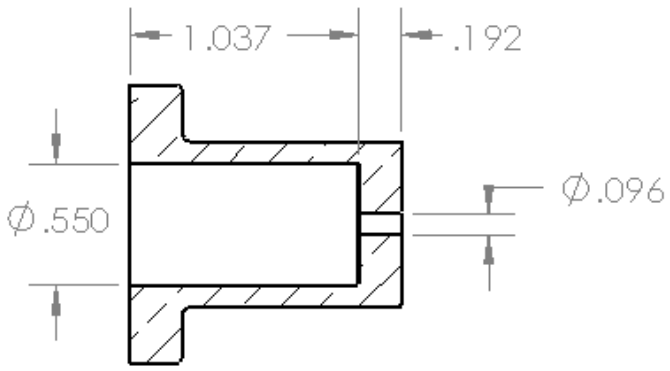

Figure 40. Schematic of the '2S' nozzle (all dimensions are in inch)

The process water temperature was varied from 25-80°C in increments of 5°C at a fixed pressure ratio of 0.472 (water pressure = 30 psig, steam pressure = 80 psig) and water flow rate of 15 gpm. The observed trends are similar to those found in the plume frequency for the 1S nozzle. High frequency stable plume oscillations fall to medium frequency condensation oscillation peaks before many peaks are found in the transition regime. However, the point at which these transitions occur happened later (i.e., at higher temperatures) in the test. Condensation oscillation becomes noticeable around 60°C, and the transition regime is not observed until around 80°C. The amplitude of these peaks and level of broadband noise of the plume area likewise increases as the process water temperature is increased. It is noted that a frequency around 3000 Hz is present in the nozzle as it approaches instability, but this frequency does not last once the condensation oscillation regime is reached. Figs. 41 and 42 show this pathway to instability for amplitude and frequency peaks for the 2S nozzle.

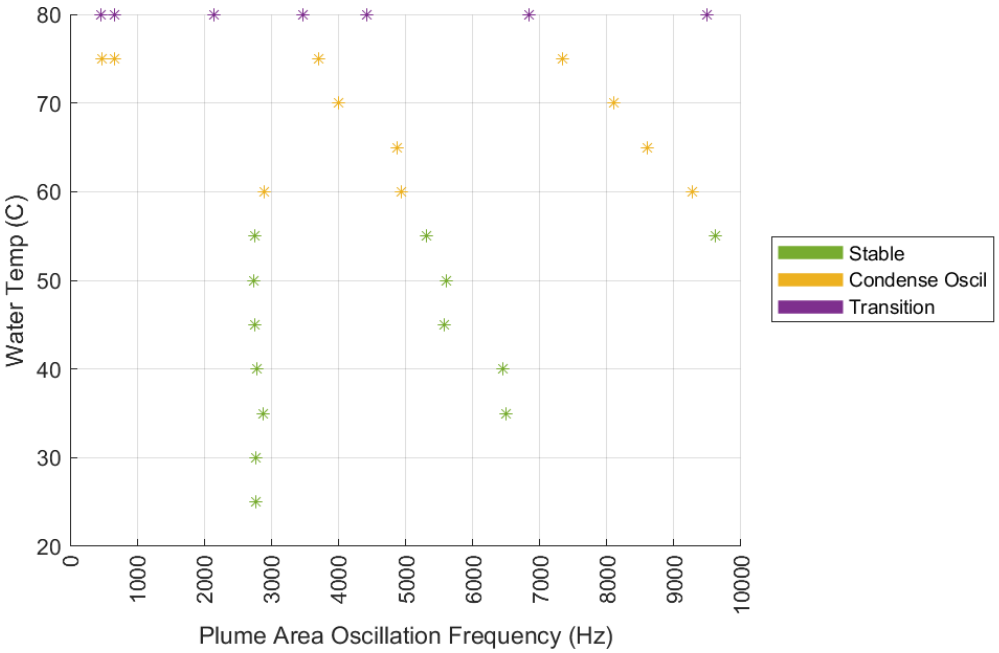

Figure 41. Map of major 2S plume area frequencies as a function of process water temperature. The dominant frequencies follow two decreasing ‘pathways’ to the transition regime with an additional dominant frequency holding around 3000 Hz throughout the stable regime.

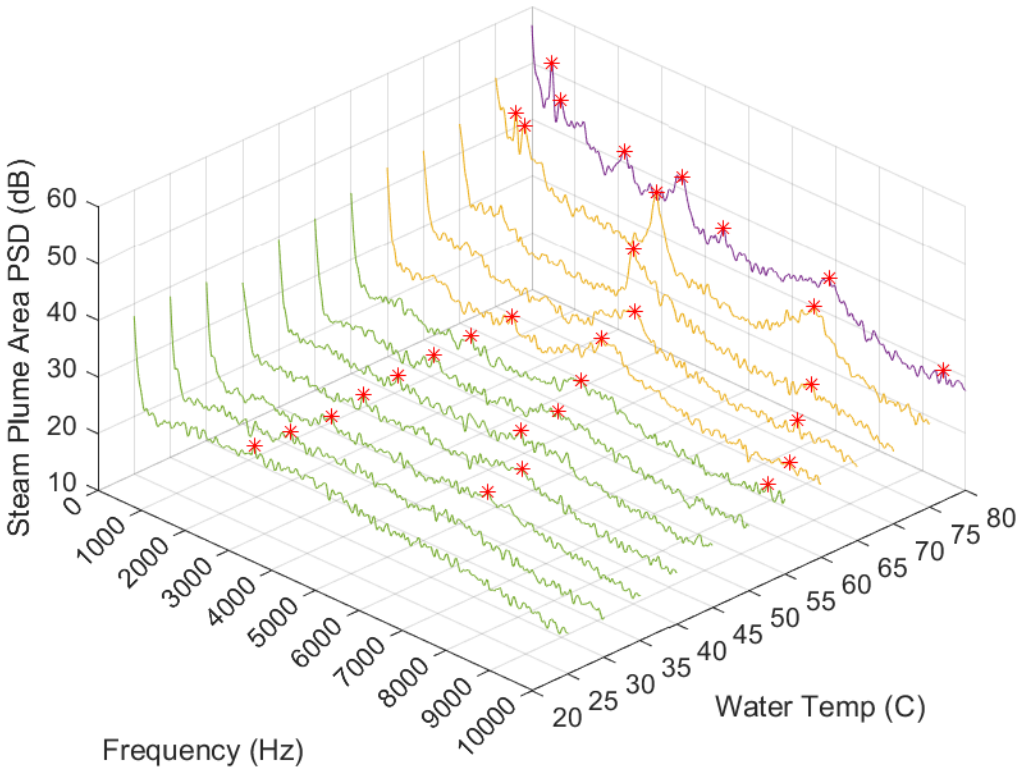

Figure 42. Waterfall plot of the 2S plume area PSD as a function of water temperature at a pressure ratio of 0.472 (water pressure = 30 psig, steam pressure = 80 psig). Green is the stable regime, yellow is the condensation oscillation regime, and purple is the transition regime. There is not a lot of activity observed in the PSDs until near the transition regime at high temperature, at which point the broadband structure of the spectrum rises quickly.

6.2 3S Nozzle

The 3S nozzle keeps the same simple straight-bore nozzle geometry with an inner diameter of 0.096 inch, but the length to diameter (L/D) ratio of the nozzle is increased to 3. This nozzle is referred to as the 3S nozzle because it is a ‘straight’ nozzle (S) with an L/D ratio of 3. A schematic of the nozzle is shown in Fig. 43.

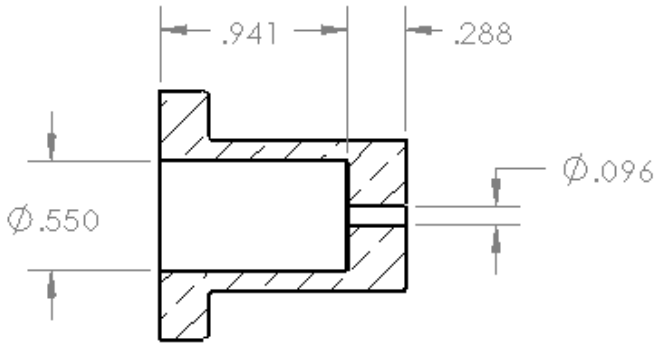

Figure 43. Schematic of the '3S' nozzle (all dimensions are in inch)

A test was carried out in which the process water temperature is increased from 25-80°C in increments of 5°C at a fixed pressure ratio of 0.472 (water pressure = 30 psig, steam pressure = 80 psig) and water flow rate of 15 gpm. In general, more activity is observed in the 3S nozzle than in the 1S or 2S nozzles. The high frequencies normally encountered in the stable regime are accompanied by lower frequencies of around 3000 and 1000 Hz, though they are all caused by changes in the plume width and height. The condensation oscillation regime, appearing at 55°C, and the transition regime, appearing at 65°C, are present for a smaller temperature range in the process water. The fully unstable regime is also present within the 3S nozzle, appearing at 70°C; this fully unstable regime was not observed in any of the other nozzles within this study. There are multiple frequency 'paths' found during the test as the temperature increases; each of these paths decrease in frequency and increase in amplitude as the instability is approached. This is a trend that was not found in the 1S and only partially observed in the 2S nozzle. Figures 44 and 45 show this pathway to instability for amplitude and frequency peaks for the 3S nozzle. It should be noted that the instability occurs most rapidly and early through the temperature sweep in the 3S nozzle.

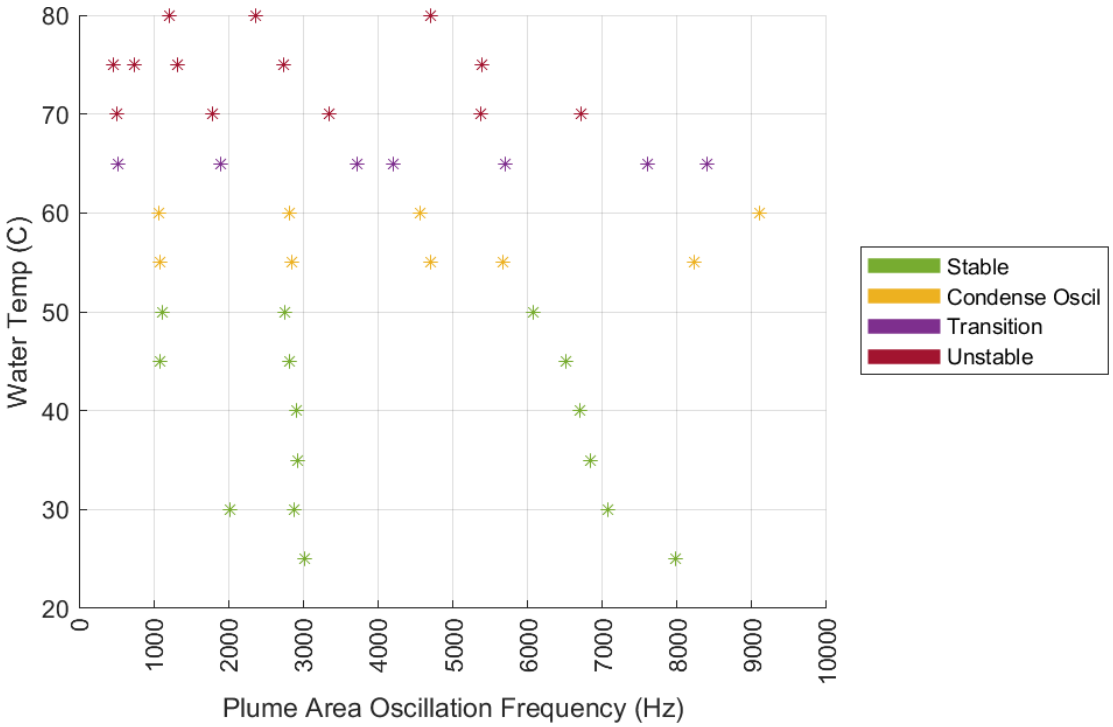

Figure 44. Map of major 3S plume area frequencies as a function of process water temperature. There are multiple frequency pathways as the process water is increased, culminating in fully unstable frequencies around 1000-3000 Hz and 5000 Hz.

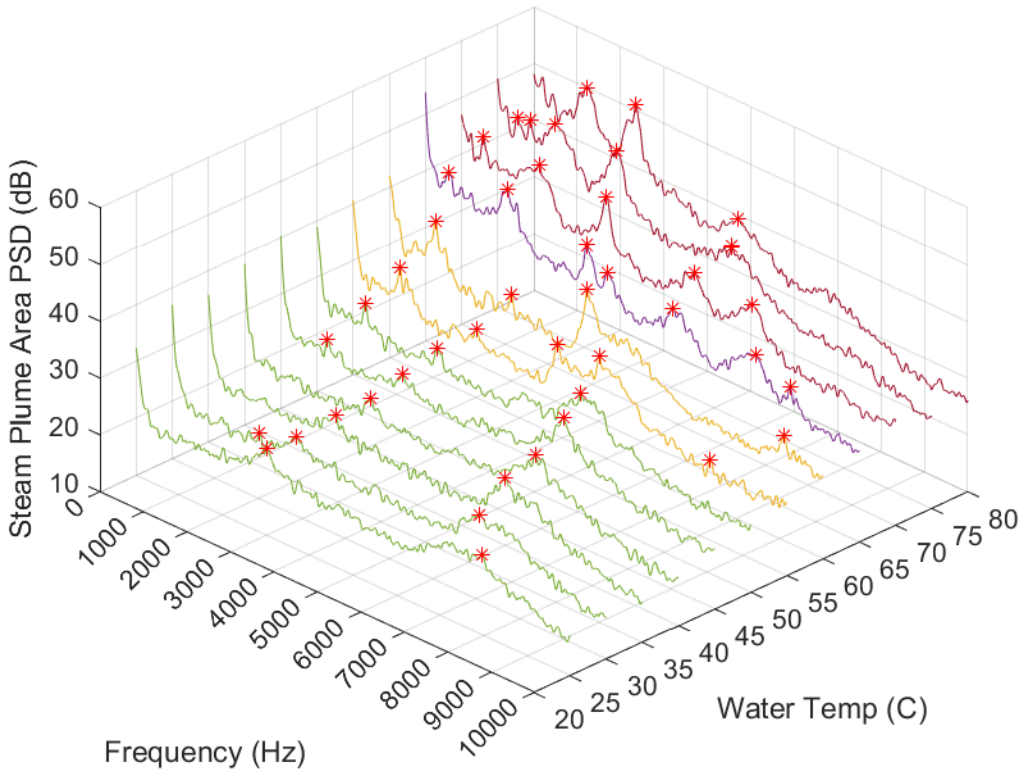

Figure 45. Waterfall plot of the 3S plume area PSD as a function of water temperature at a pressure ratio of 0.472 (water pressure = 30 psig, steam pressure = 80 psig). Green is the stable regime, yellow is the condensation oscillation regime, purple is the transition regime, and red is the unstable regime. A short condensation oscillation and transition regime precedes the fully unstable regime.

6.3 1S Nozzle

The 2S and 3S nozzles were run at the same pressure ratio (0.472) as the 1S nozzle but at a different pressure differential (30/80 vs 25/70, respectively). In order to ensure that this pressure differential change would not skew results, a temperature sweep was performed on the 1S nozzle at the same conditions as the 2S and 3S nozzles (PR = 0.472, water pressure = 30 psig, steam pressure = 80 psig, water flow rate = 15 gpm).

The observed trends are similar to those found previously for the 1S nozzle. Condensation is stable at low temperatures. The condensation oscillation regime is observed to begin around 50°C. The transition

regime where the plume begins to break down into bubbles occurs around 70°C. These regime changes are consistent with the previous temperature sweep.

Frequency data shown in Figs. 46 and 47 also aligns with the trend of the previous 1S nozzle temperature sweep. High frequency stable plume oscillations fall to medium frequency condensation oscillation peaks before many peaks are found in the transition regime. However, an additional frequency peak around 3000 Hz is also observed through the stable and condensation oscillation regimes, and the amplitudes of the peaks in the condensation oscillation regime are more muted than previously.

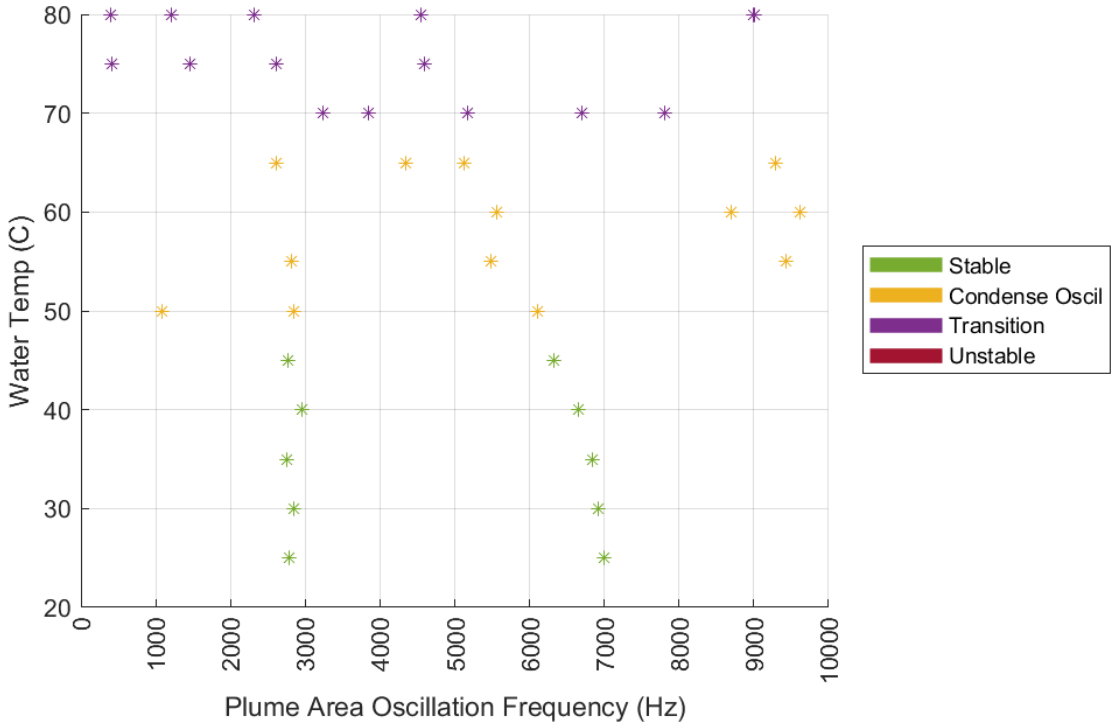

Figure 46. Map of major 1S plume area frequencies as a function of process water temperature at a pressure ratio of 0.472 (water pressure = 30 psig, steam pressure = 80 psig). While a frequency pathway can be observed running from 7000 to 2000 Hz as temperature is increased, an additional frequency is observed around 3000 Hz.

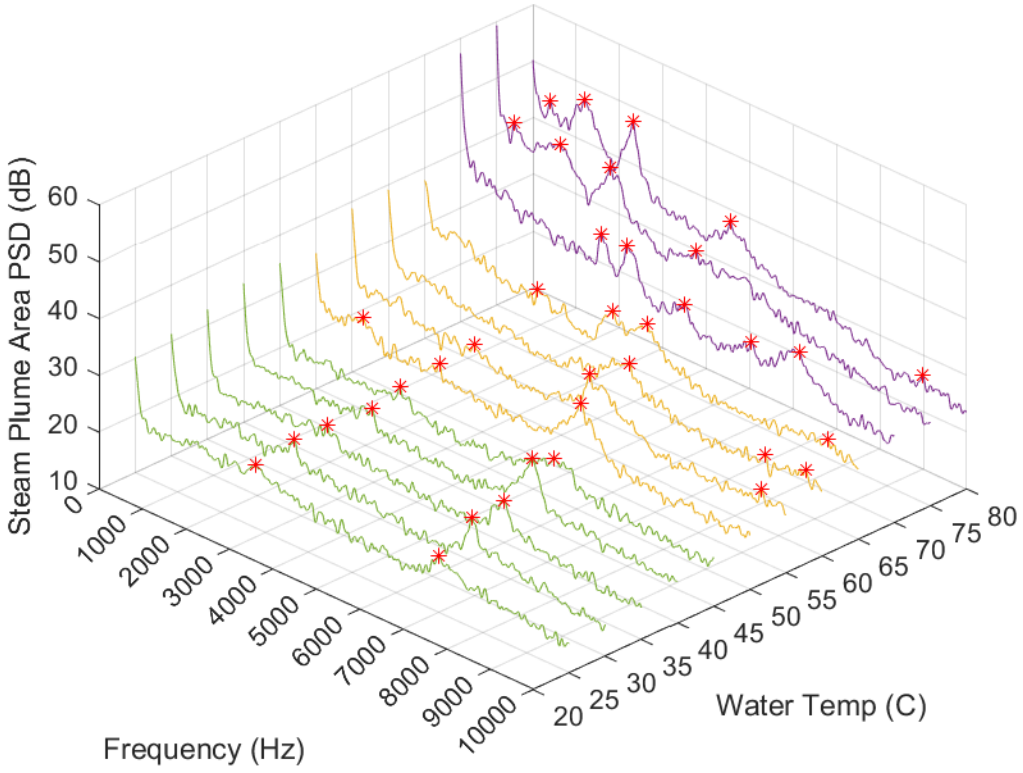

Figure 47. Waterfall plot of the 1S plume area PSD as a function of water temperature at a pressure ratio of 0.472 (water pressure = 30 psig, steam pressure = 80 psig). Green is the stable regime, yellow is the condensation oscillation regime, and purple is the transition regime. Peaks found within the condensation oscillation regime are more muted than the previous temperature sweep of the 1S nozzle.

While regime changes may occur at the roughly the same temperatures, it should be noted that the frequency magnitudes appear to shift between the 25/70 and 30/80 pressure ratio tests. Specifically, the peaks in the 25/70 pressure ratio plume area PSD occur at lower frequencies than their counterparts in the 30/80 pressure ratio plume area PSD, as shown in Fig. 48. Frequencies within the stable and transition regimes appear to shift by less than 1000 Hz, but those within the condensation oscillation regime appear have even greater shifts in frequency.

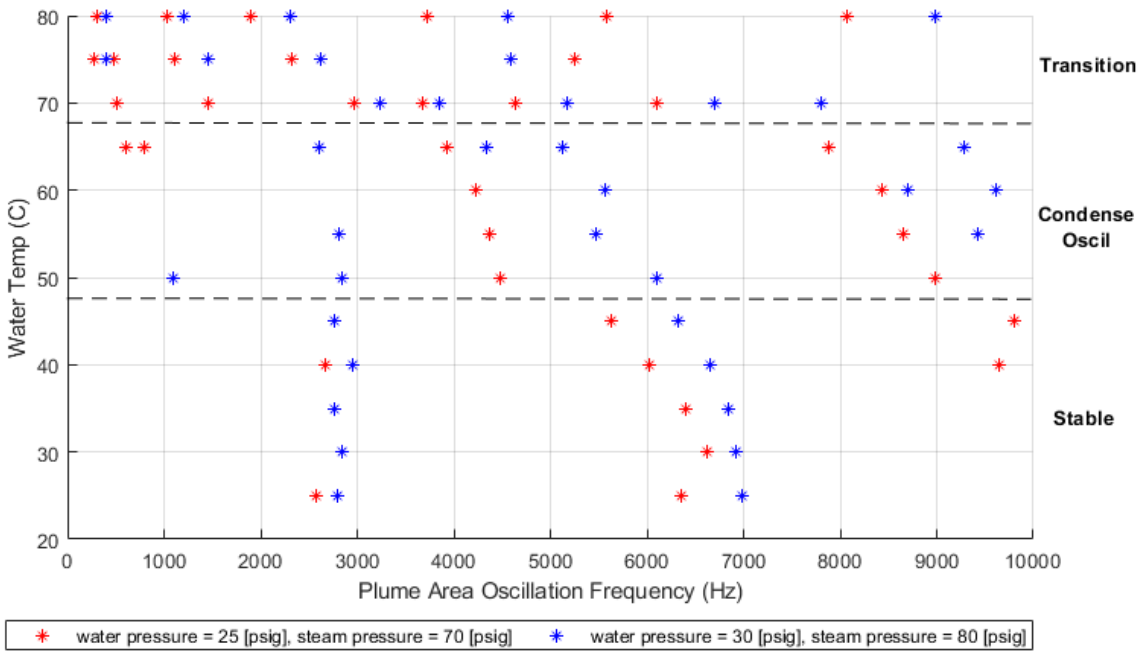

Figure 48. Comparing the major plume area frequencies of the 1S nozzle between pressure ratios of 25/70 psig and 30/80 psig. Frequencies observed in the 25/70 pressure ratio test (red) are consistently shifted lower than those observed within the 30/80 pressure ratio test (blue).

6.4 Comparison of Straight Nozzles

Figure 49 shows a comparison of the 1S, 2S, and 3S nozzles and suggests that the 2S nozzle is the best geometry in terms of the pathway to condensation instability at a nozzle diameter of 0.096 inch. Likewise, there is significant differences in the onset of instability between the three nozzles, with the 2S nozzle entering the transition regime around 75-80°C whereas the 3S nozzle enters the transition regime between 60-65°C and the unstable regime between 65-70°C. The 1S nozzle produces results between these two, entering the transition regime at 65-70°C and the unstable regime at 75-80°C. The introduction of the condensation oscillation regime follows this same trend with the length-diameter ratio of 2 being the last to enter this regime.

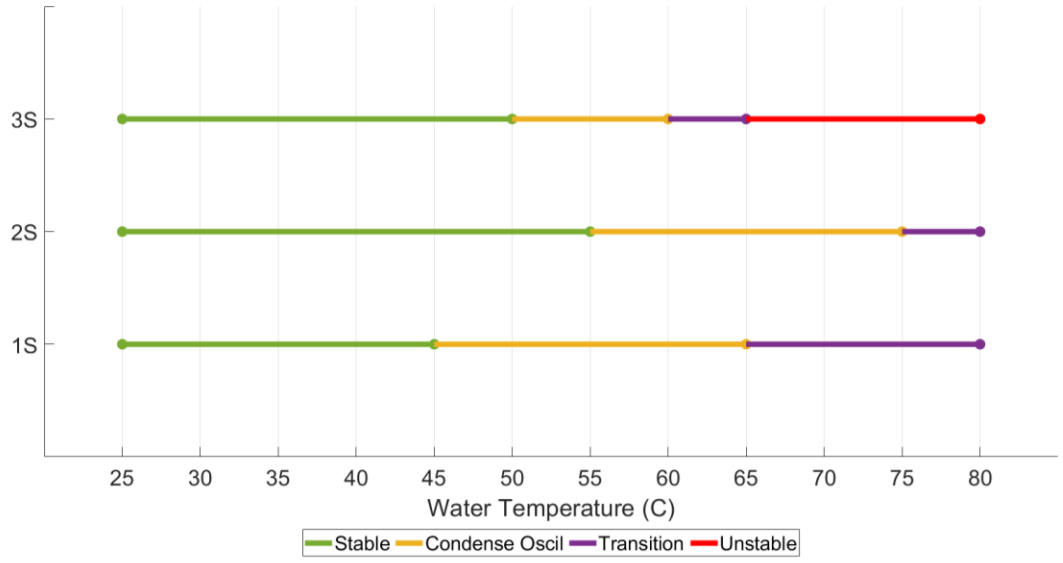

Figure 49. Regime map of condensation stability as a function of process water temperature and L/D ratio. All trials are collected at pressure ratios of 0.472 and water flow rates of 15 gpm.

X-ray scans of the 3 nozzles are shown in Figs. 50-52; these were collected to investigate whether any small defects that may have occurred during the manufacturing process could be influencing the results. Macroscopically, all three nozzles show good circularity and a relatively smooth channel for flow. The entrance to the 2S nozzle has a very slight chamfer while the 3S shows a very slight obstruction. It is unknown whether geometric deviations of this size could lead into relatively dramatic differences in the stability observed for these nozzles or if the L/D difference is the major explanation for these observed stability differences; it is assumed for now to be the latter rather than the former of these two. The next chapter describes relatively large effects in stability that are caused by defects in nozzle geometry

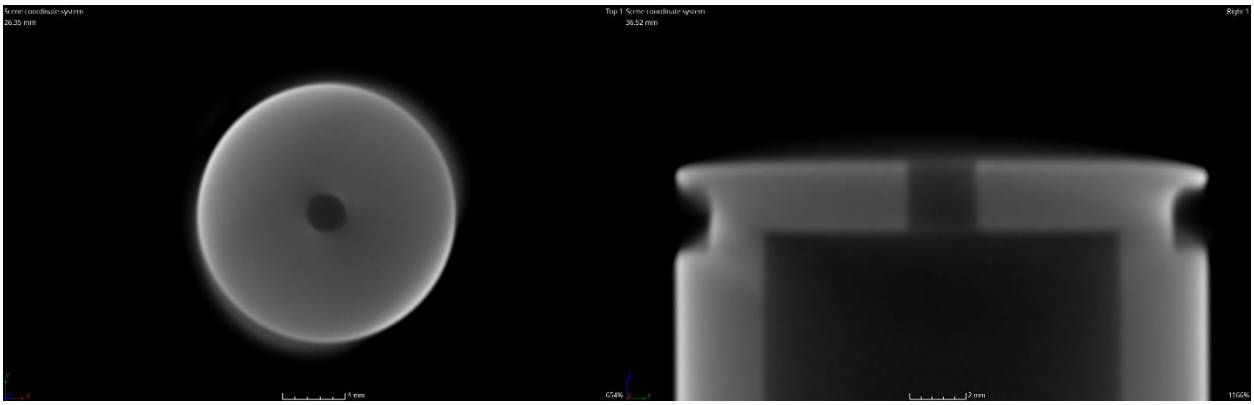

Figure 50. X-ray scan of the normal (left) and tangent (right) views of the 1S nozzle

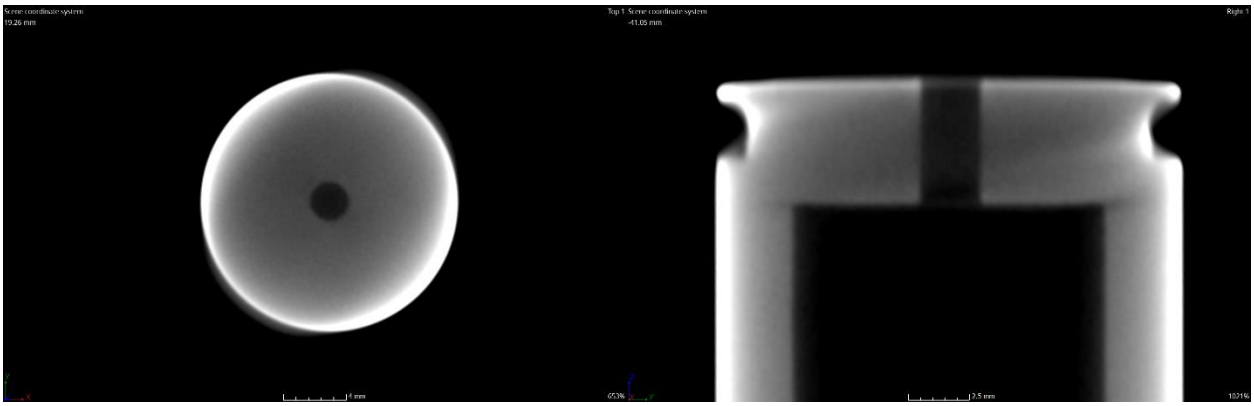

Figure 51. X-ray scan of the normal (left) and tangent (right) views of the 2S nozzle

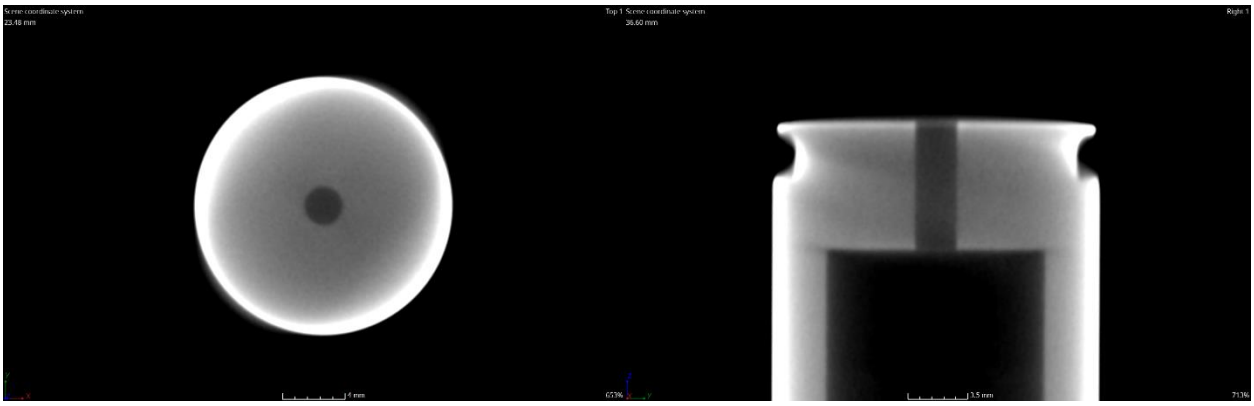

Figure 52. X-ray scan of the normal (left) and tangent (right) views of the 3S nozzle

7. Nozzle Defect Study – 2-2S, 2.5S, 2EC Nozzles

When trying to recreate the 2S nozzle in order to verify its performance, an interesting result was found inadvertently due to a defect in the manufacturing process. The new nozzle, referred to as 2-2S, was found to be significantly worse in terms of performance and stability, even though the nozzle geometry should was meant to be the same as the 2S nozzle. A similar, although slightly better, result was found in the 2.5S nozzle that was being used to further explore the L/D ratio effect of the nozzle. These findings lend credence to the hypothesis that very small changes to the nozzle geometry caused by the manufacturing process can have a large effect on the stability of the steam condensation process.

7.1 2-2S Nozzle

As mentioned previously, the '2-2S' nozzle has the same gross geometry as the 2S nozzle with an inner diameter of 0.096 inch and a L/D ratio of 2. Since it is a recreation of the 2S nozzle, it retains a '-2' designation in its naming convention. A detailed drawing of the nozzle for machining is shown in Fig. 53.

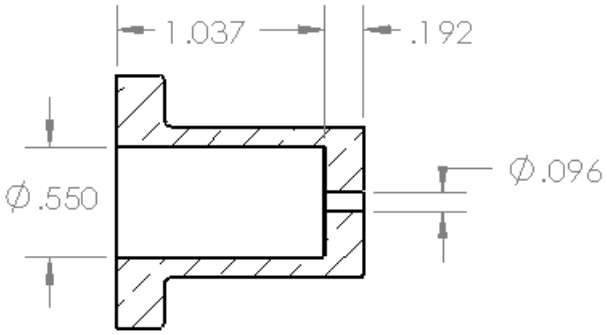

Figure 53. Drawing of the '2-2S' nozzle (all dimensions are in inches)

Data was taken by carrying out a temperature sweep of 25-80°C in increments of 5°C at a pressure ratio of 0.472 (water pressure = 30 psig, steam pressure = 80 psig) and a water flow rate of 15 gpm. Note that the frequency response and stability pathway is very different from the previous 2S nozzle that was

tested, as shown in Figs. 54 and 55. Instability is encountered immediately (i.e. at the lowest temperature tested), and the noise from the steam injection is extremely high (it can be heard from outside the lab area). The dominant frequency is between 2000-3000 Hz upon start up, but switches to a higher frequency, around 4000 Hz, once the water temperature reaches 45°C. This frequency then decreases as temperature is further increased until it reaches around 3000 Hz at very high temperatures. While frequencies between 2000-3000 Hz are also encountered in the 2S nozzle at low temperatures, it is unknown if these frequencies can be translated over to the 2-2S nozzle, i.e. positing that the lower frequency pathway becomes dominant in the 2-2S and causes the earlier instability would be only speculation for now. However, the lower dominant frequencies found in the 2-2S nozzle are normally found in much later temperatures when the plume is unstable in other nozzles.

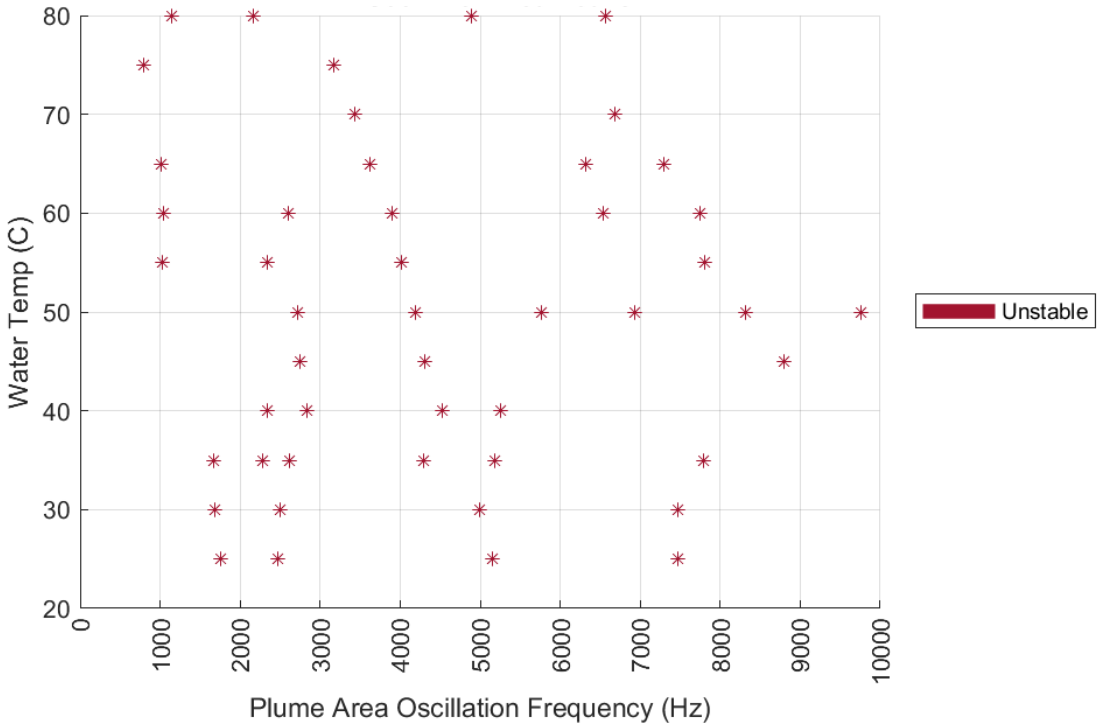

Figure 54. Map of major 2-2S plume area frequencies as a function of process water temperature. The nozzle is immediately unstable and shows frequencies around 1000-2000, 2500-3000, 3000-5000, and 6000-9000 Hz. The 2500-3000 and 3000-5000 Hz frequencies are the most prominent.

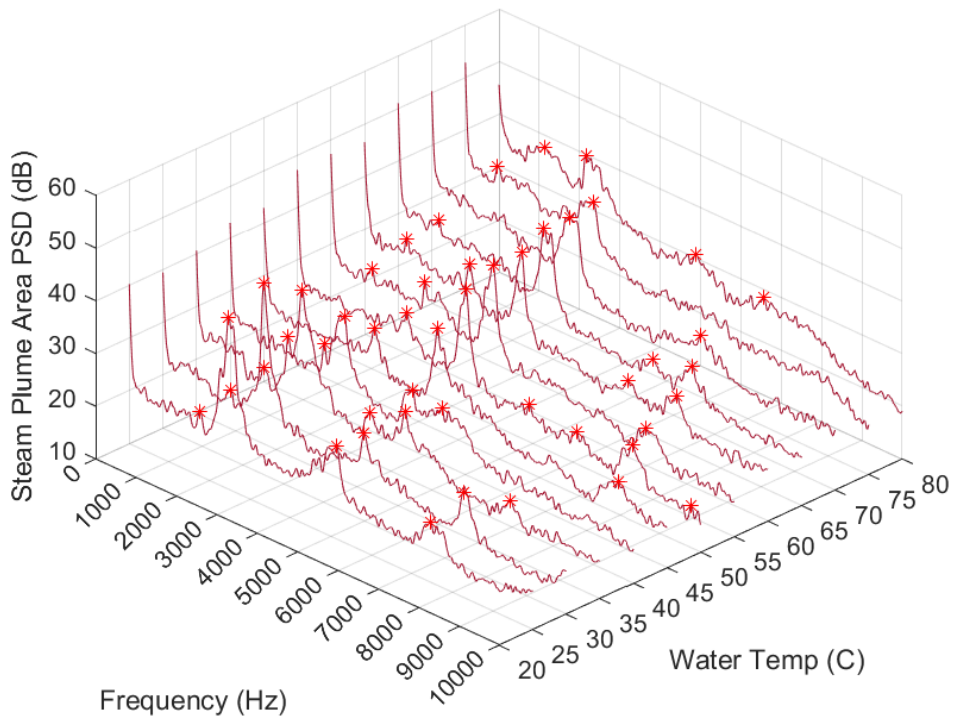

Figure 55. Waterfall plot of the 2-2S plume area PSD as a function of water temperature at a pressure ratio of 0.472 (water pressure = 30 psig, steam pressure = 80 psig). All temperatures are unstable (red).

An x-ray scan of the nozzle, shown in Fig. 56, highlights defects associated with the drilling process. These defects are on the order of 0.01 inches, about the thickness of your fingernail, and so may not be noticed immediately upon visual inspection. However, these deviations from the original 2S nozzle may lead to a different flow pattern through the nozzle and thus a much faster pathway to instability.

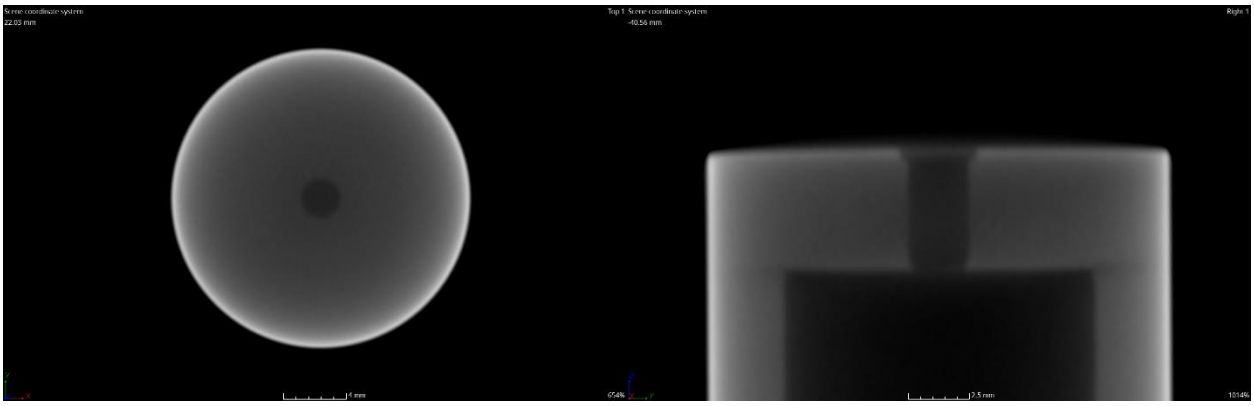

Figure 56. X-ray scan of the normal (left) and tangent (right) views of the 2-2S nozzle

7.2 2.5S Nozzle

This early-onset instability was also noticed in a second straight-bored nozzle that was meant to be used as another data point to further explore the L/D effect on stability. The 2.5S nozzle keeps the same simple straight-bore nozzle geometry with an inner diameter of 0.096", but the L/D ratio of the nozzle is set to 2.5 to provide an intermediate data point between the 2S and 3S nozzles. A schematic of the nozzle is shown in Fig. 57.

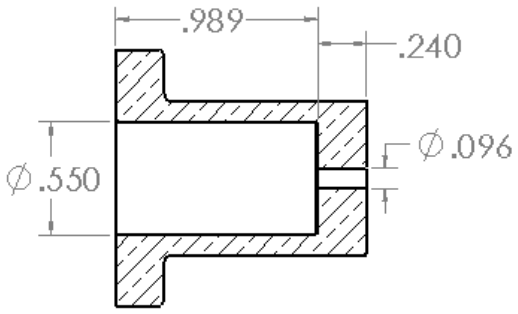

Figure 57. Schematic of the '2.5S' nozzle

Looking at Figs. 58 and 59, the 2.5S nozzle is able to proceed about halfway through the 25-80°C temperature sweep (PR = 0.472, water pressure = 30 psig, steam pressure = 80 psig, flow = 15 gpm) before going unstable. There is significant activity in the low temperature range, indicating that the sweep starts in the condensation oscillation regime rather than in the stable regime. Plume oscillations start around 7500 Hz at 25°C and steadily decrease to 6000 Hz before the plume enters the transition regime at 60°C. Like the 2-2S nozzle, there is a peak in frequency around 3000 Hz that is maintained through the increase in temperature.

The plume quickly enters and exits the transition regime around 60°C before fully entering the unstable regime at 65°C. Once the instability point is reached, the most significant frequency peaks drop to 2000 and 4000 Hz due to the plume collapsing into bubbles. These peaks steadily decrease to around 1200 and 2200 Hz, respectively, at 80°C.

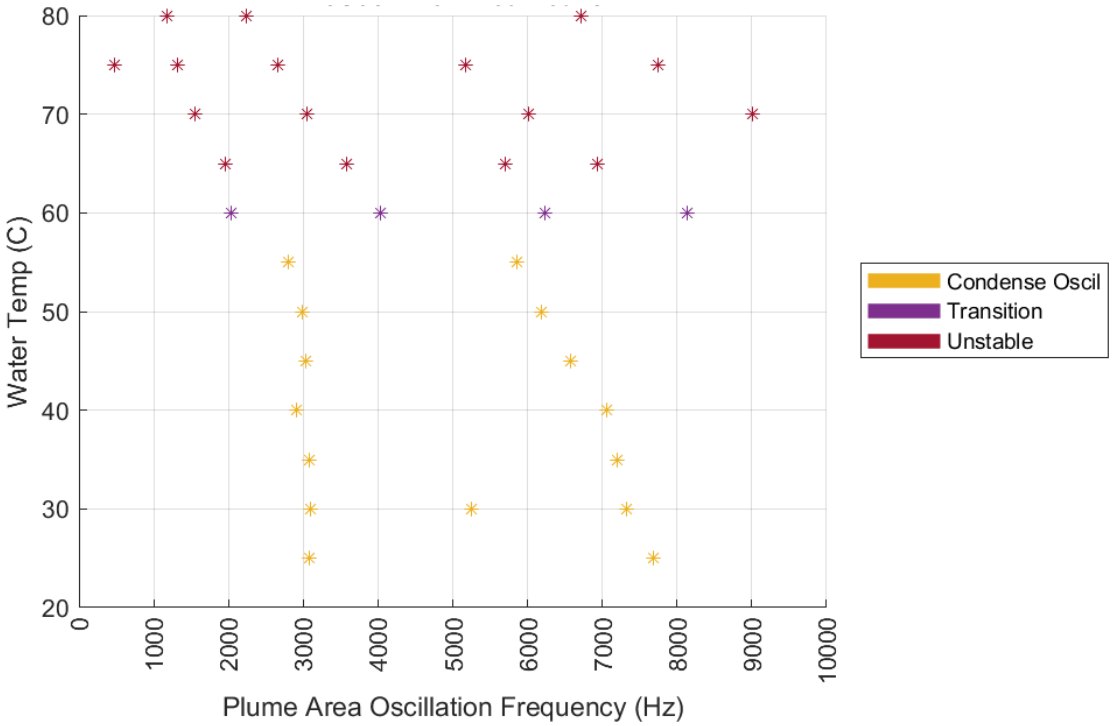

Figure 58. Map of major 2.5S plume area frequencies as a function of process water temperature. Two frequencies 'pathways', one at 3000 Hz and one at 6000-8000 Hz, are found in the condensation oscillation regime before blossoming to tracks around 1000-2000 Hz, 2000-4000 Hz, and 5000-9000 Hz in the transition and unstable regimes.

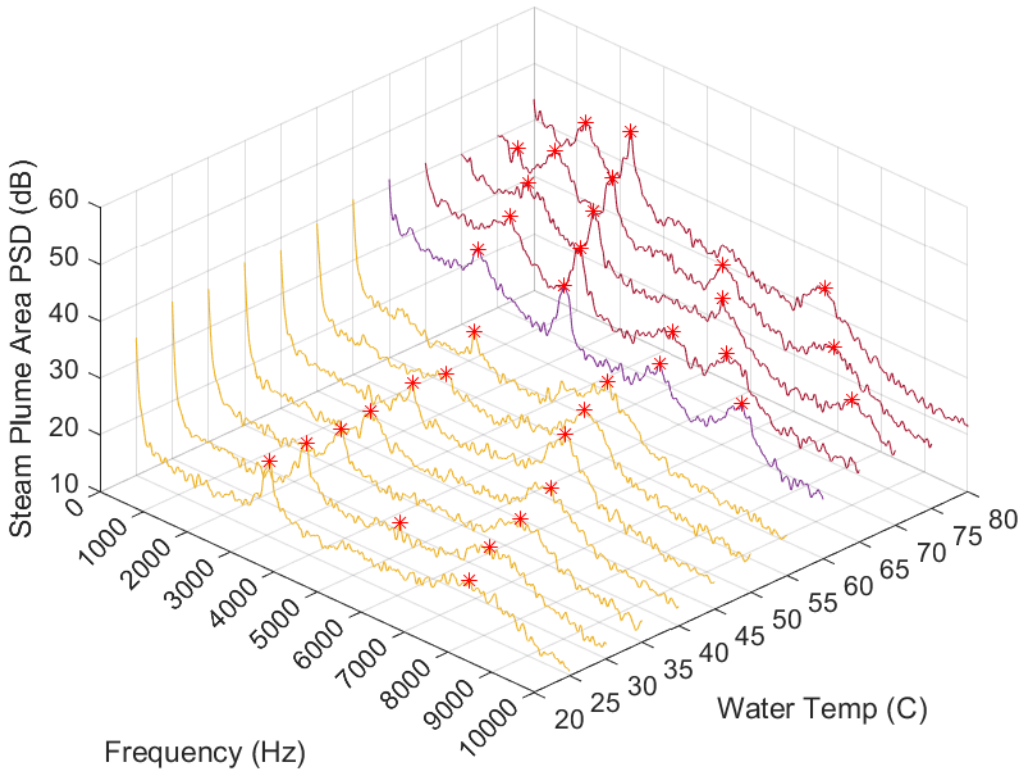

Figure 59. Waterfall plot of the 2.5S plume area PSD as a function of water temperature at a pressure ratio of 0.472 (water pressure = 30 psig, steam pressure = 80 psig). Yellow is the condensation oscillation regime, purple is the transition regime, and red is the unstable condensation regime. Significant peaks are found from the start of the test (i.e. low temperature) through the end (i.e. high temperature)

The x-ray of the 2.5S nozzle may explain this behavior. The scan shown in Fig. 60 does not show the drastic defects that can be observed in the 2-2S nozzle. However, there is a noticeable obstruction at the inlet of the nozzle. When comparing the 2.5S nozzle to other straight nozzle scans, this observation suggests that the leading edge of the nozzle plays a significant role in the onset of instability.

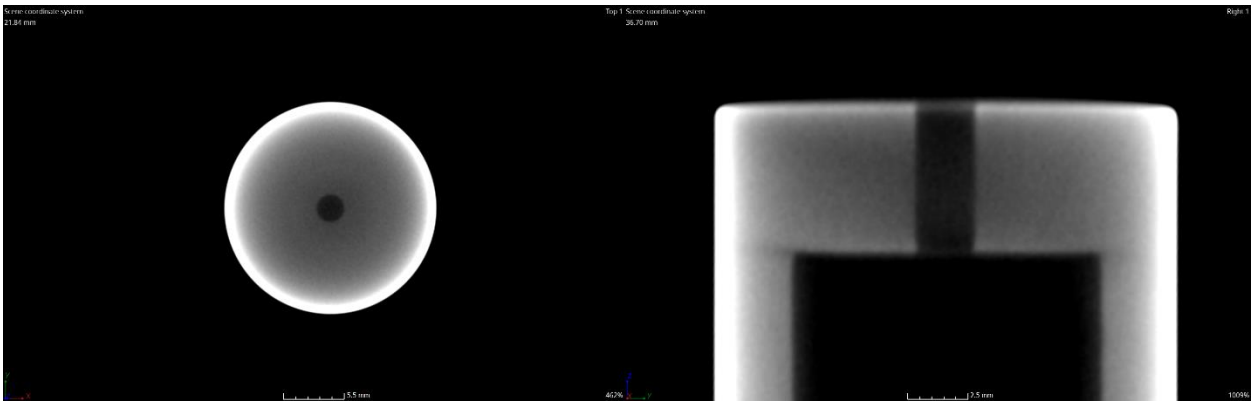

Figure 60. X-ray scan of the normal (left) and tangent (right) views of the 2.5S nozzle

7.3 2EC Nozzle

The 2-2S nozzle shows both an inlet obstruction and an outlet expansion in its x-ray scan. The 2.5S nozzle analyzed above shows another inlet obstruction. In order to understand the impact of the outlet expansion an outlet chamfer is added to a straight nozzle for testing purposes. In this way, the '2EC' nozzle was created. This nozzle has the same dimensions as the 2S nozzle for the straight section of the nozzle, but also has a 30° chamfer at the exit to simulate the divergence that was inadvertently created in the 2-2S nozzle. This nozzle is referred to as the 2EC nozzle because it has a straight L/D ratio of 2 with an external chamfer (EC) added during the machining process. A schematic of the nozzle is shown in Fig. 61.

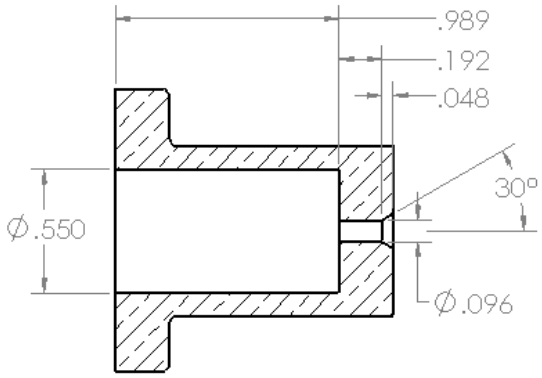

Figure 61. Schematic of the '2EC' nozzle (all dimensions are in inches)

Looking at Figs. 62 and 63, the 2EC nozzle is also able to proceed about halfway through the 25-80°C temperature sweep (PR = 0.472, water pressure = 30 psig, steam pressure = 80 psig, flow = 15 gpm) before becoming unstable. There is significant activity immediately upon starting the sweep, but the plume maintains a single structure. Thus, until about 55°C, the nozzle is in the condensation oscillation regime. Most plume frequency peaks are concentrated between 1000-4000 Hz, specifically around 1000, 2500, and 4000 Hz. The frequency peaks in the condensation oscillation regime also show large magnitudes relative to the noise level of the spectrum, especially when the instability is approached. Unlike other nozzles, there are no high frequency peaks (~6000-7000 Hz) noticed in the spectrum in this temperature range.

The plume does not enter a transition regime, instead proceeding directly to instability around 55°C. Once the instability point is reached, the frequency peaks from the condensation oscillation continue to reduce in frequency while the entire spectrum rises in magnitude as the temperature is further increased. The 1000 Hz frequency is gradually swallowed by the rising spectrum around 70°C. The only peak from the condensation oscillation regime to stay above the noise level throughout the sweep is the 4000 Hz frequency, which has been reduced to ~3500 Hz at the introduction of instability and ~2500 Hz at the end of the temperature sweep. A higher frequency of 7000 Hz is also introduced once the plume goes unstable. This decreases steadily to 5000 Hz by the end of the sweep as well. This pathway to instability is second worst of all the nozzles tested (only the 2-2S nozzle is worse), yet it maintains stability in the condensation oscillation regime for a significant amount of the sweep before finally collapsing.

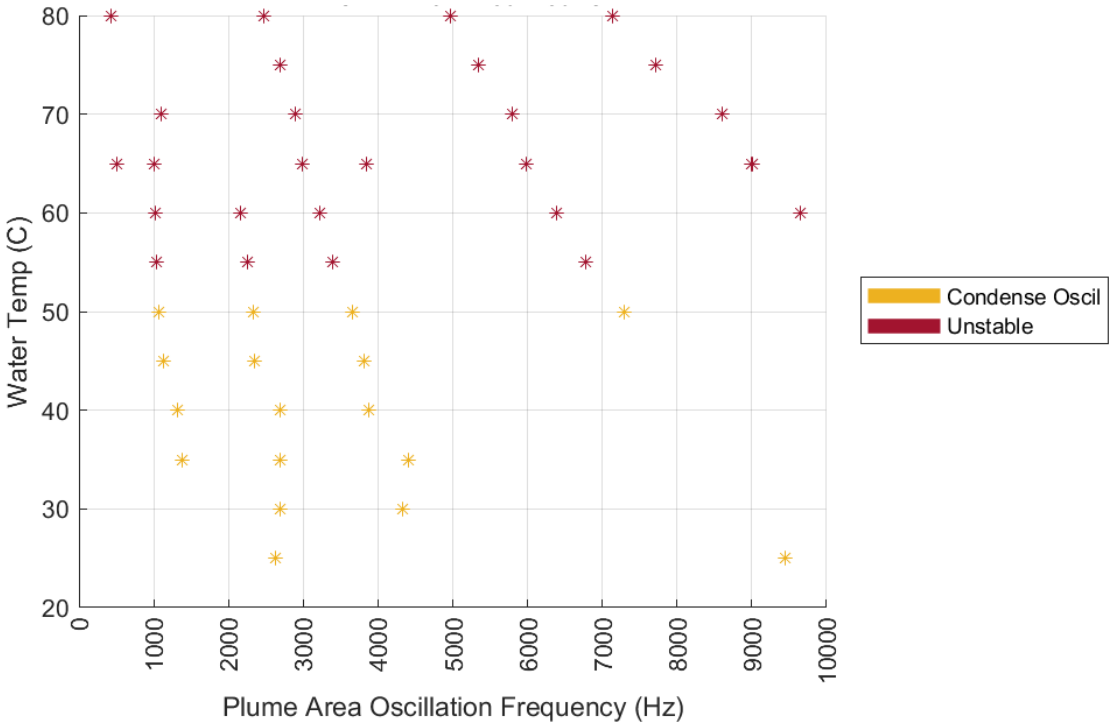

Figure 62. Map of major 2EC plume area frequencies as a function of process water temperature. Most of the activity is concentrated in the lower frequency range until the plume goes fully unstable, at which point higher frequencies become prominent as well.

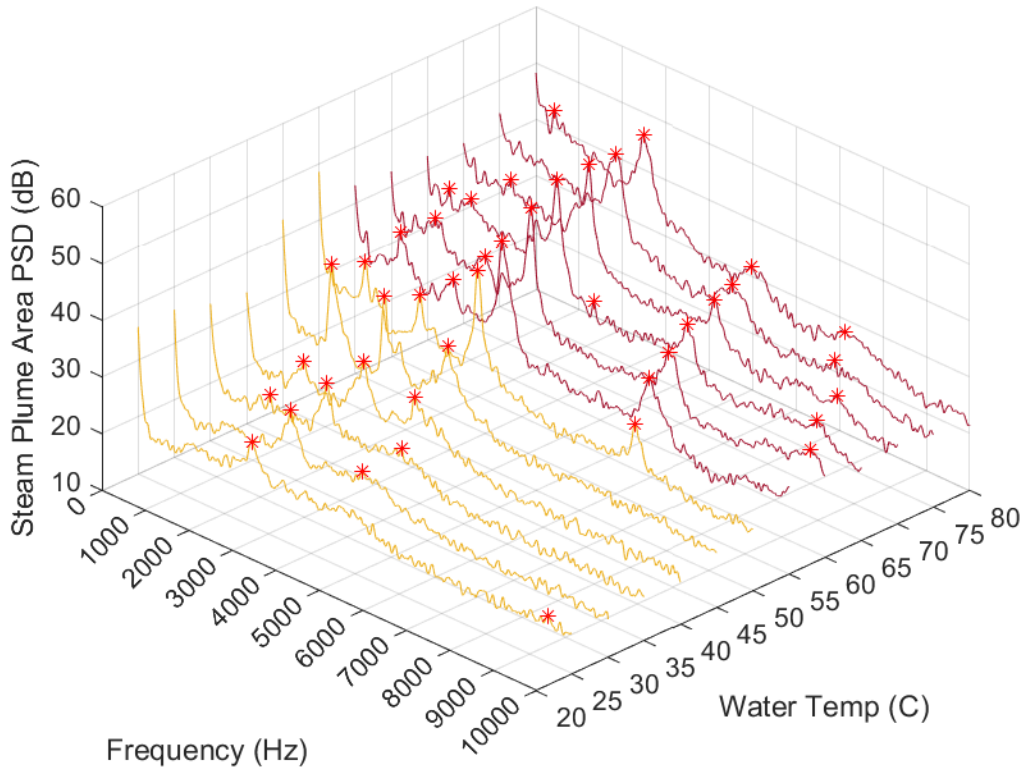

Figure 63. Waterfall plot of the 2EC plume area PSD as a function of water temperature at a pressure ratio of 0.472 (water pressure = 30 psig, steam pressure = 80 psig). Yellow is the condensation oscillation regime, and the red is the unstable condensation regime. Most activity is centered around 2000-4000 Hz. Higher frequencies are also observed when the plume becomes unstable.

An examination of the x-ray scan in Fig. 64 highlights the outlet chamfer of the 2EC nozzle. It is very similar to that of the 2-2S nozzle, but the inlet contraction is not present. Thus, the expansion at the outlet of the nozzle does reduce the stability of the nozzle, but not as much as it would when coupled with an inlet obstruction.

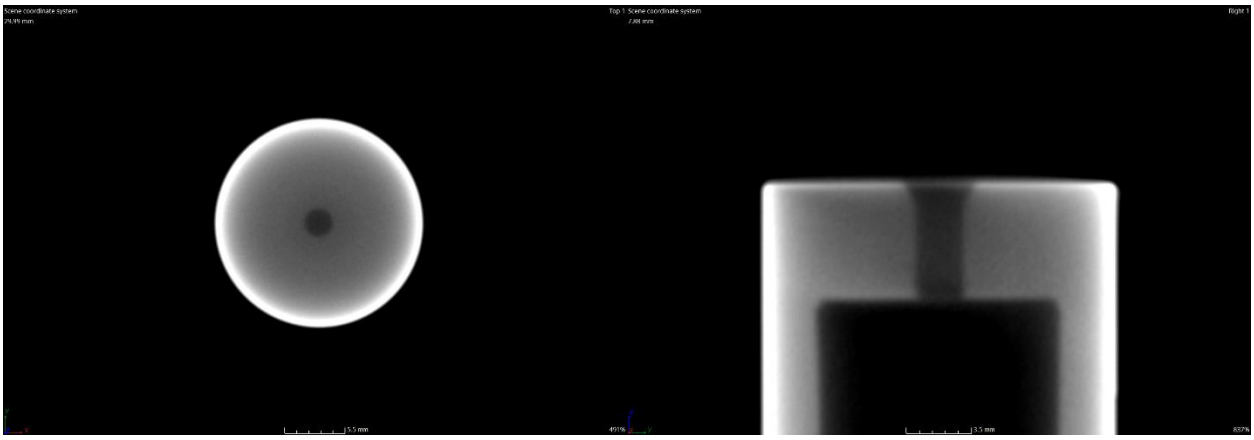

Figure 64. X-ray scan of the normal (left) and tangent (right) views of the 2EC nozzle

7.4 Comparison of Nozzle Defects

This chapter shows “what not to do” in terms of injection nozzle design. Each of the nozzles described above (2-2S, 2.5S, 2EC) exhibit a rapid path to instability during a temperature sweep, if they are not immediately unstable, as shown in the regime map of Fig. 65. The 2EC and 2.5S nozzles begin with significant oscillations in the condensation oscillation regime. The 2EC nozzle then breaks down into bubbling around 55°C, and the 2.5S nozzle has a short transition regime at 60°C before fully going unstable at 65°C. This early instability could be caused by the shape of the nozzle: the outlet expansion of the 2EC or the contracted leading edge of the 2.5S nozzle, respectively.

The 2-2S nozzle most clearly showcases the risk of a ‘defective’ nozzle. With an obstructed leading edge and an outlet expansion, both of these effects work together to produce the worst nozzle that was tested. The nozzle immediately goes unstable upon the injection of steam, which is completely opposite of the smooth, stable injection exhibited by the 2S nozzle.

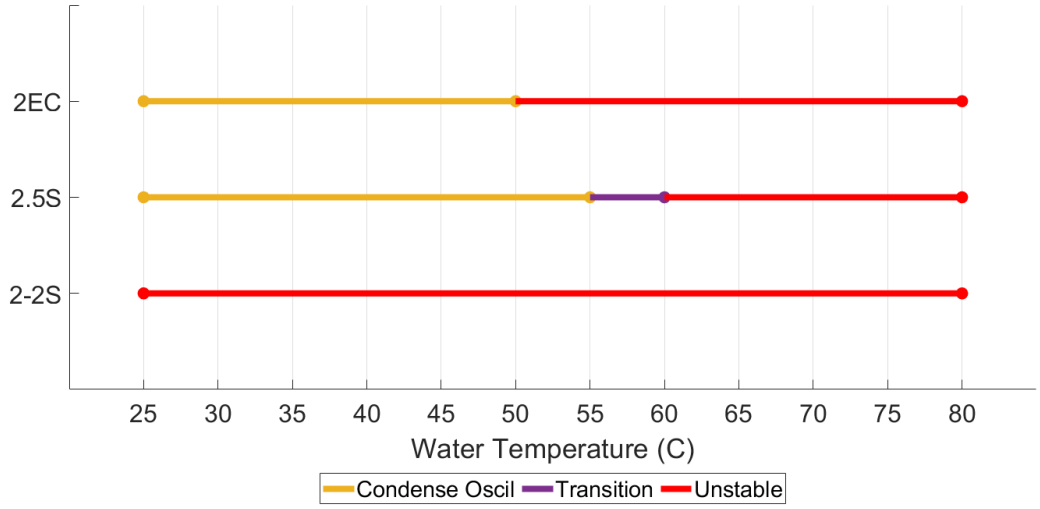

Figure 65. Regime map of condensation stability as a function of process water temperature and nozzles with defects in their geometry. All trials are collected at pressure ratios of 0.472 and water flow rates of 15 gpm.

Examination of the steam mass flux reinforces these differences. Fig. 66 shows the steam mass flux associated with the straight nozzles and their 'defective' cousins through the temperature sweep. All nozzles are run at the same conditions (process water temperature range, nozzle pressure ratio, process water flow rate), and the mass flow is therefore an independent parameter. The 1S, 2S, and 3S nozzles all show mass fluxes between 900-950 $\frac{kg}{m^2 s}$. The 2EC nozzle show mass fluxes that are slightly less at 825-875 $\frac{kg}{m^2 s}$. The 2.5S nozzle is even worse at 750-800 $\frac{kg}{m^2 s}$. Finally, the 2-2S is the clear loser in this regard, falling between 600-650 $\frac{kg}{m^2 s}$. It has been previously shown that a decreased steam mass flux results in instability; the steam momentum trends to stabilize the injection. This data brings the relationship back full-circle. Even if all other parameters can be kept the same, small geometric imperfections impact the mass flow rate through the nozzle, resulting in a nozzle that will put the steam injection at a disadvantage before injection has even begun.

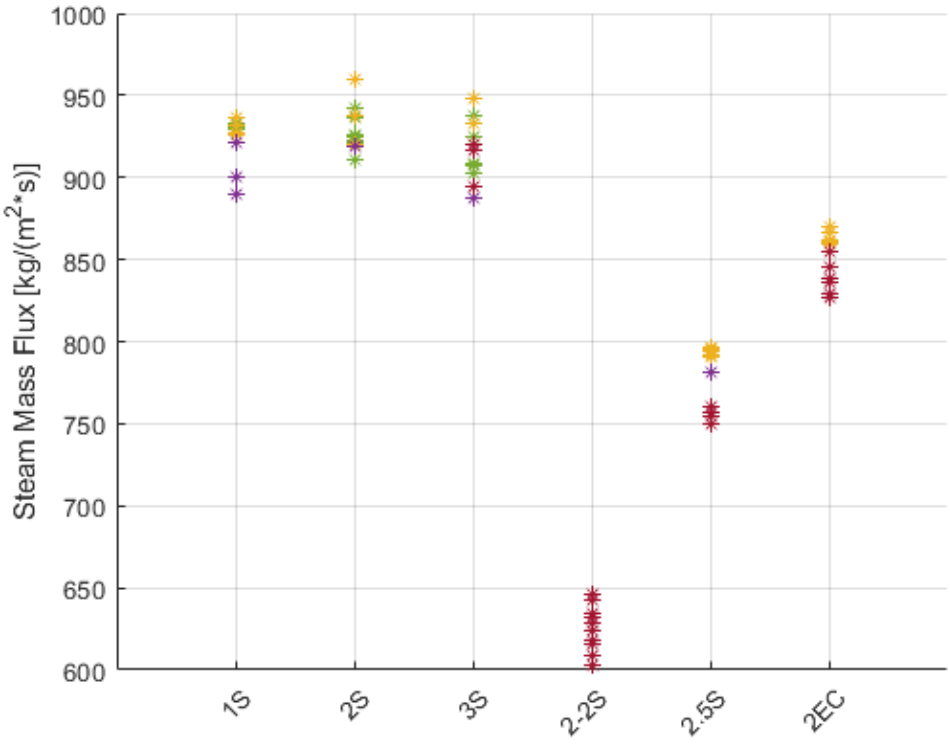

Figure 66. Steam mass flux for each temperature sweep of the straight and 'defected' nozzles. All trials are run at a pressure ratio of 0.472 (water pressure = 30 psig, steam pressure = 80 psig) and a process water flow rate = 15 gpm.

8. Internal Chamfer Study – 1C, 2C, 3C Nozzles

This chapter focuses on the opposite of the nozzle 'defects' studied in the last section: a chamfer on the leading edge of the nozzle. This smoother entrance into the nozzle has the opposite effect on stability, and the nozzles with this feature are some of the best that were tested. Internal chamfers are added to the 1S, 2S, and 3S nozzle designs; these are designated as the 1C, 2C, and 3C nozzles, respectively, and tested through the same temperature sweep. It is noted that, while the chamfered nozzles did not perform better than the 2S nozzle, any trends previously observed related to the L/D ratio effect are gone for the chamfered nozzles. The addition of the entrance chamfer causes all nozzles to provide consistent and good results in terms of stability.

8.1 1C Nozzle

The first nozzle under examination is the ‘1C’ nozzle. The dimensions of the 1S nozzle are maintained (inner diameter 0.096”, straight section length 0.096”), but a small entrance length is added with a 30° chamfer to better guide the steam into the nozzle. To help designate this nozzle amongst others, it is named the 1C nozzle for being a ‘chamfered’ nozzle with a straight-section L/D ratio of 1. A schematic of the nozzle is shown in Fig. 67.

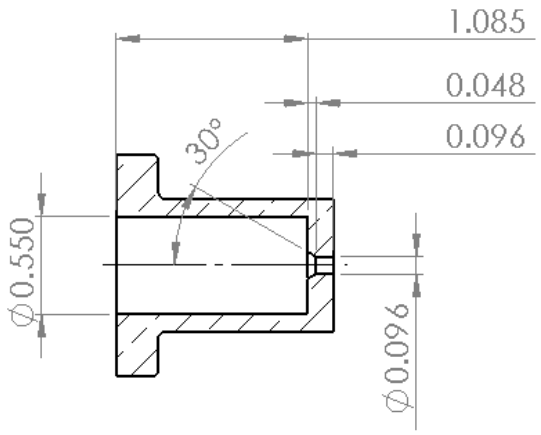

Figure 67. Schematic of the ‘1C’ nozzle (all dimensions are in inches)

Running the 25-80°C temperature sweep at the usual pressure ratio of 0.472 (water pressure = 30 psig, steam pressure = 80 psig) and water flow rate of 15 gpm shows a long pathway to instability. Plume oscillations of low magnitude can be found around 3000 and 6000-7000 Hz in the low temperature regime, but the plume is quite stable until around 60°C. Significant peaks form around 4000 and 8000 Hz when the plume enters the condensation regime, decreasing in frequency until the plume finally breaks down into the transition regime around 75°C. From there, the dominant frequencies range from 500 to 1200-1500 to 2200-2800 Hz as the plume sometimes collapses into the chaotic bubbling structure of the unstable regime. However, the plume never goes fully unstable during testing, and the condensation mode is a battle between the single plume of the condensation oscillation regime and the bubbling disarray of the unstable regime. Figs. 68 and 69 show this pathway to instability for the 1C nozzle.

When comparing results to the 1S nozzle, the 1C is a noticeable improvement. Instead of entering the condensation oscillation regime around 50°C, this regime change is extended another 10°C to 60°C. Similar, the 1S nozzle enters the transition regime around 70°C. The 1C nozzle holds off on this transition for 5°C more, finally collapsing at 75°C.

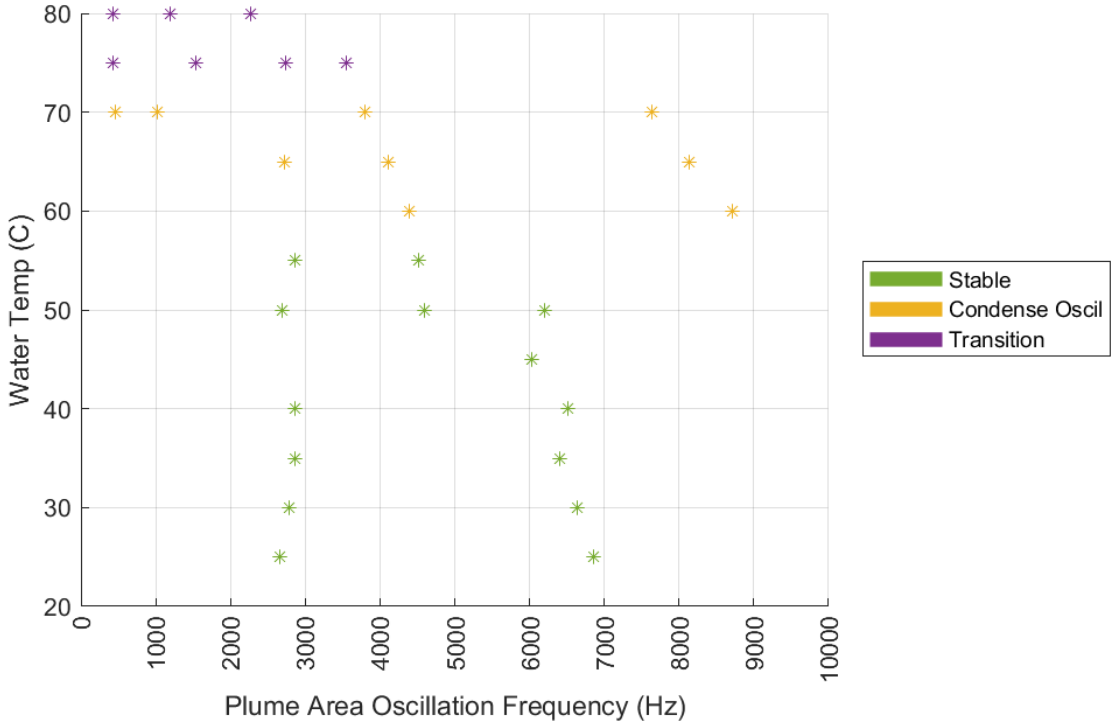

Figure 68. Map of major 1C plume area frequencies as a function of process water temperature. The dominant frequency of the stable regime starts at 7000 Hz before reducing as it approaches the condensation oscillation and transition regimes at higher temperatures. There is also a 3000 Hz frequency noticed through the stable regime.

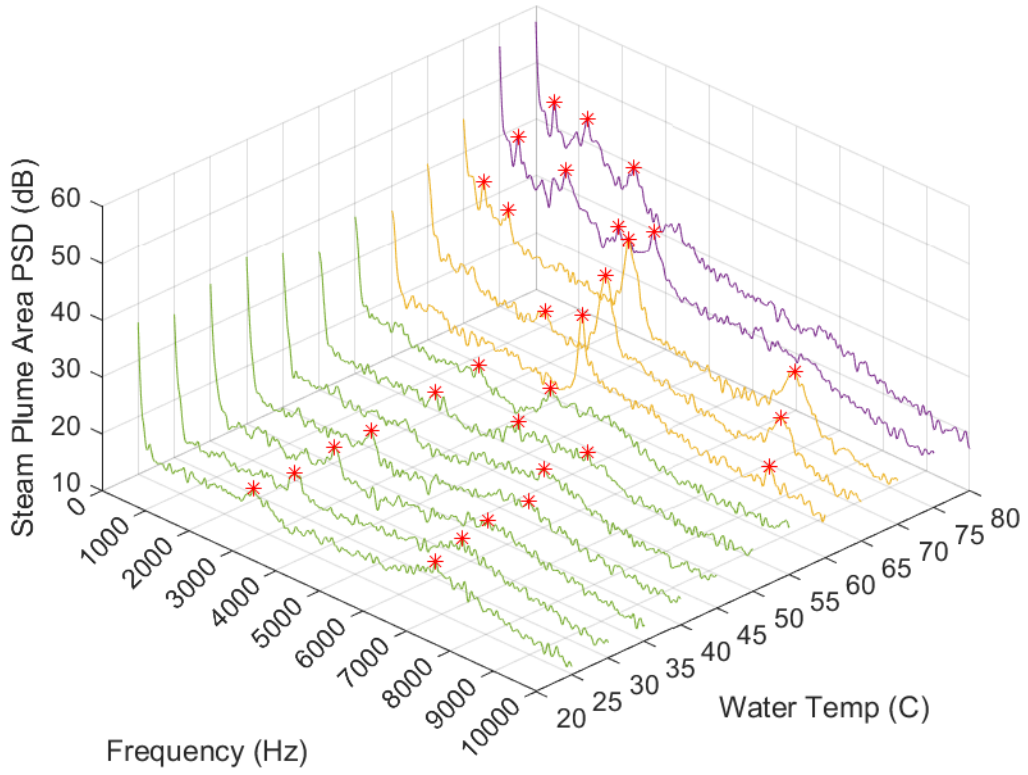

Figure 69. Waterfall plot of the 1C plume area PSD as a function of water temperature at a pressure ratio of 0.472 (water pressure = 30 psig, steam pressure = 80 psig). Green is the stable condensation regime, yellow is the condensation oscillation regime, and purple is the transition regime. Frequencies follow a decreasing trend while amplitudes increase as water temperature is increased.

8.2 2C Nozzle

In keeping with comparing to the L/D effect study, the next nozzle under analysis is the 2C nozzle. Similar to the 1C nozzle design, the dimensions of the 2S nozzle are maintained (inner diameter 0.096", straight section length 0.096"), but a small entrance length is added with a 30° chamfer pecked drilled to better guide the steam into the nozzle. To help designate this nozzle amongst others, it is named the 2C nozzle for being a 'chamfered' nozzle with a straight-section L/D ratio of 2. A schematic of the nozzle is shown in Fig. 70.

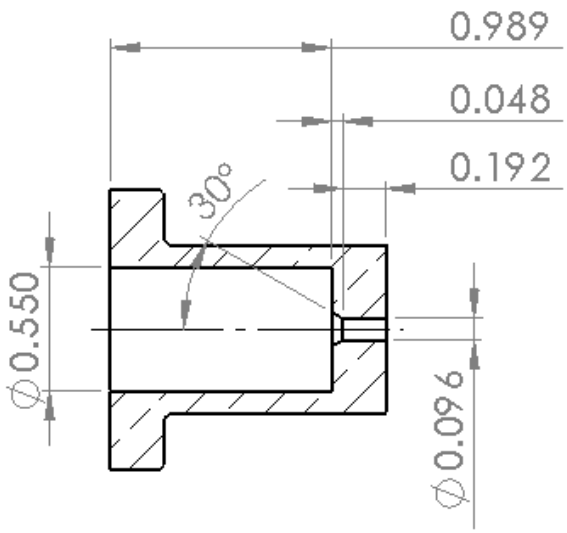

Figure 70. Schematic of the ‘2C’ nozzle (all dimensions are in inches)

The 25-80°C temperature sweep at the usual pressure ratio of 0.472 (water pressure = 30 psig, steam pressure = 80 psig) and water flow rate of 15 gpm gives slightly disappointing results. The 2C nozzle does not have a better path to instability than the 2S nozzle. In fact, it is slightly worse. Plume oscillations of low magnitude can be found around 3000 and 6000-7000 Hz in the low temperature regime, but the plume is quite stable until around 60°C. A significant peak around 4000 Hz appears as the plume enters the condensation regime, decreasing in frequency and rising in magnitude until the plume finally breaks down into the transition regime around 75°C. A frequency peak around 8000 Hz also shows up around 70°C and follows the same trend of decreased frequency, increased intensity as the process temperature is increased. From there, the dominant frequencies range from 500 to 1200-1600 to 2200-2900 Hz as the plume sometimes collapses into the chaotic bubbling structure of the unstable regime. However, the plume never goes fully unstable during testing, and the condensation mode is a battle between the single plume of the condensation oscillation regime and the bubbling disarray of the unstable regime. Figs. 71 and 72 show this pathway to instability for the 2C nozzle.

If the previous paragraph sounds oddly familiar, it is because this is the same story of the 1C nozzle. Indeed, comparing the steam plume area PSDs between the 1C and 2C nozzles show only slight

differences in plume frequencies. For instance, the 3000 Hz frequencies are not as prominent, even disappearing, in the stable regime, and the 8000 Hz frequencies do not show up immediately in the condensation oscillation regime. Like the 2-2S and 2.5S nozzles suggesting that a contraction at the inlet can ruin stability, the inlet chamfer can provide good, consistent stability results. The 3C nozzle discussed next further provides evidence of this.

Comparing the 2C nozzle to the 2S nozzle, there are no significant improvements in nozzle stability. Both nozzles enter the condensation oscillation regime around 60°C. While the 2S nozzle shows a higher frequency peak in the transition regime, it can hold off this regime for 5°C longer. There are tradeoffs between the two nozzle geometries, with no discernable 'winner' between the two. If one were to judge solely on the transition regime water temperature, however, the 2S nozzle is still the better of the two.

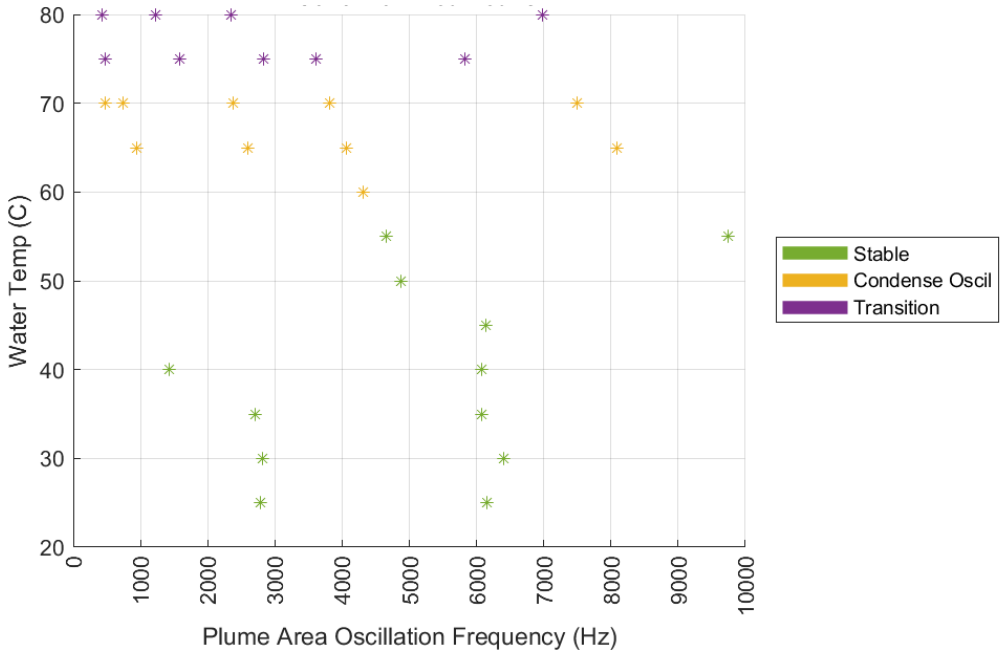

Figure 71. Map of major 2C plume area frequencies as a function of process water temperature. The frequency around 3000 Hz does not last long in the stable regime. The major frequency pathway starts at 6000 Hz in the stable condensation regime and decreases to 4000 Hz in the condensation oscillation regime. Frequencies are further reduced in the transition regime.

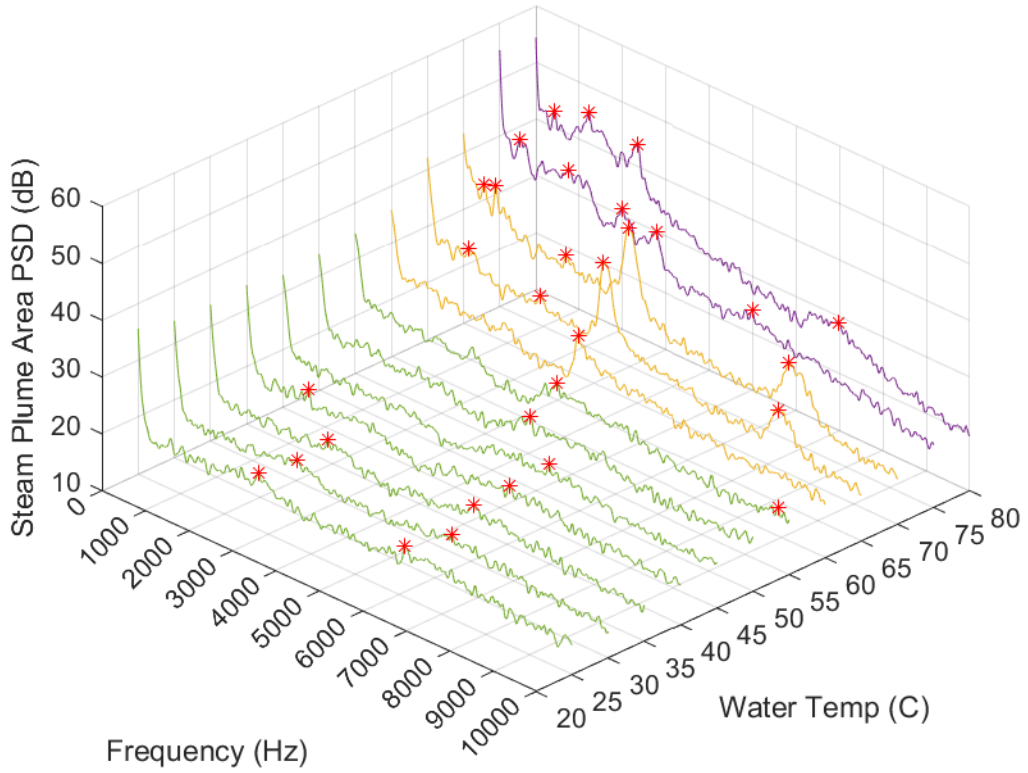

Figure 72. Waterfall plot of the 2C plume area PSD as a function of water temperature at a pressure ratio of 0.472 (water pressure = 30 psig, steam pressure = 80 psig). Green is stable, yellow is condensation oscillation, and purple is transition. Frequencies follow a decreasing trend while amplitudes increase as water temperature is increased.

8.3 3C Nozzle

The final nozzle presented in this thesis is the 3C nozzle. The dimensions of the 3S nozzle are maintained (inner diameter 0.096”, straight section length 0.096”), but a small entrance length is added with a 30° chamfer pecked drilled to better guide the steam into the nozzle. To help designate this nozzle amongst others, it is named the 3C nozzle for being a ‘chamfered’ nozzle with a straight-section L/D ratio of 3. A schematic of the nozzle is shown in Fig. 73.

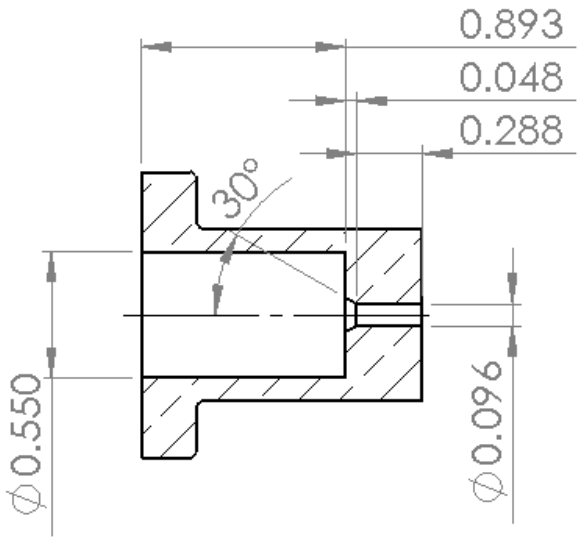

Figure 73. Schematic of the '3C' nozzle (all dimensions are in inches)

Looking at the 25-80°C temperature sweep at the usual pressure ratio of 0.472 (water pressure = 30 psig, steam pressure = 80 psig) and water flow rate of 15 gpm confirms that internal chamfer produces similar results regardless of L/D ratio. Plume oscillations of low magnitude can be found around 3000 and 7000 Hz in the low temperature regime, but the plume is quite stable until around 60°C. A significant peak around 5000 Hz appears as the plume enters the condensation regime, decreasing in frequency and rising in magnitude until the plume finally breaks down into the transition regime around 75°C. From there, the dominant frequencies range from 1000-1800 to 2200 to 3200-3600 Hz as the plume sometimes collapses into the chaotic bubbling structure of the unstable regime. Again, the plume never goes fully unstable, instead transitioning back and forth between the condensation oscillation regime and unstable regime. It would be an interesting study to determine the time between regime changes as a function of the temperature sweep, but that is not explored in this thesis. Figs. 74 and 75 show this pathway to instability for the 3C nozzle.

Like its cohort, the 3C nozzle shows only slight deviations from the main 'storyline' of the internal chamfer nozzles. The stable regime is consistent with the other nozzles, but there are no

frequencies around 8000 Hz in the condensation oscillation regime. In fact, the 3C nozzle's condensation oscillation shows the least amount of peak activity. Likewise, the frequencies in the transition regime are higher and more spread out. While the general trend is maintained across all three nozzles, the 3C nozzle could be ranked as the best due to the smallest amount of activity noticed across the temperature sweep.

A comparison to the 3S nozzle clearly shows the improvement the internal chamfer has made on the nozzle's instability pathway. The condensation oscillation regime is held off for 5°C, the transition regime for 10°C, and the unstable regime is never encountered. This small change to the leading edge of the nozzle has an enormous impact on the stability of the nozzle in regards to the 3S and 3C nozzles.

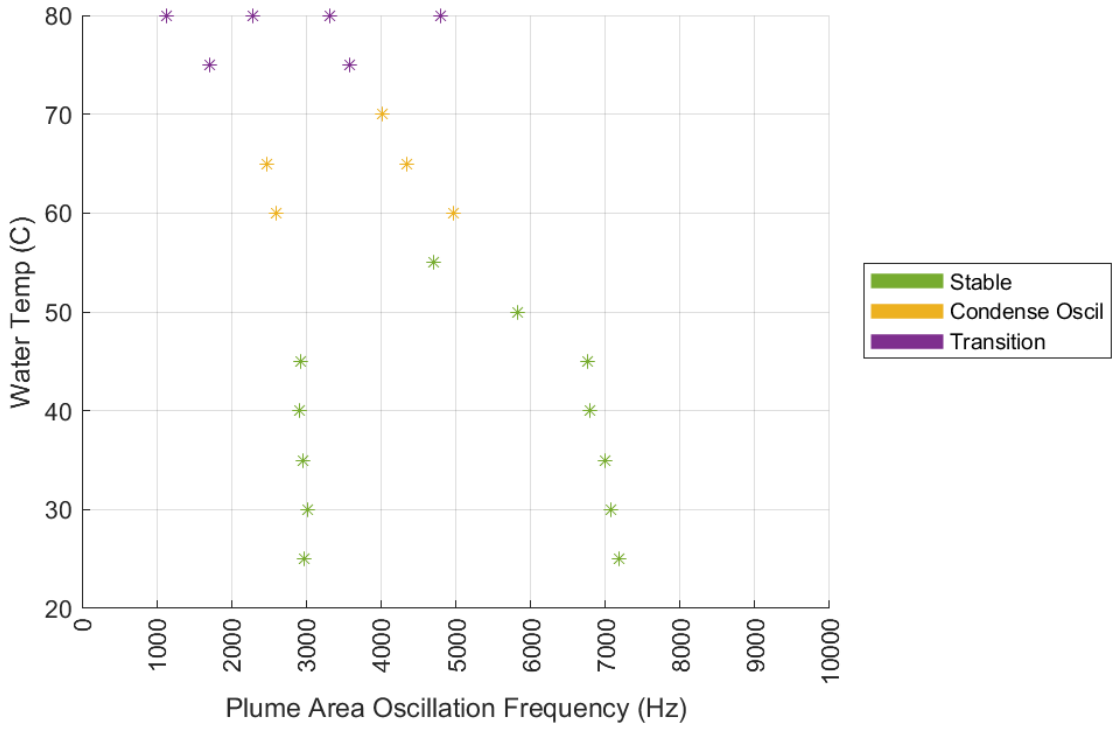

Figure 74. Map of major 3C plume area frequencies as a function of process water temperature. The frequencies are contained to a constant 3000 Hz through the stable condensation regime, and a path starting at 7000 Hz and ending at 3300 Hz upon reaching the transition regime.

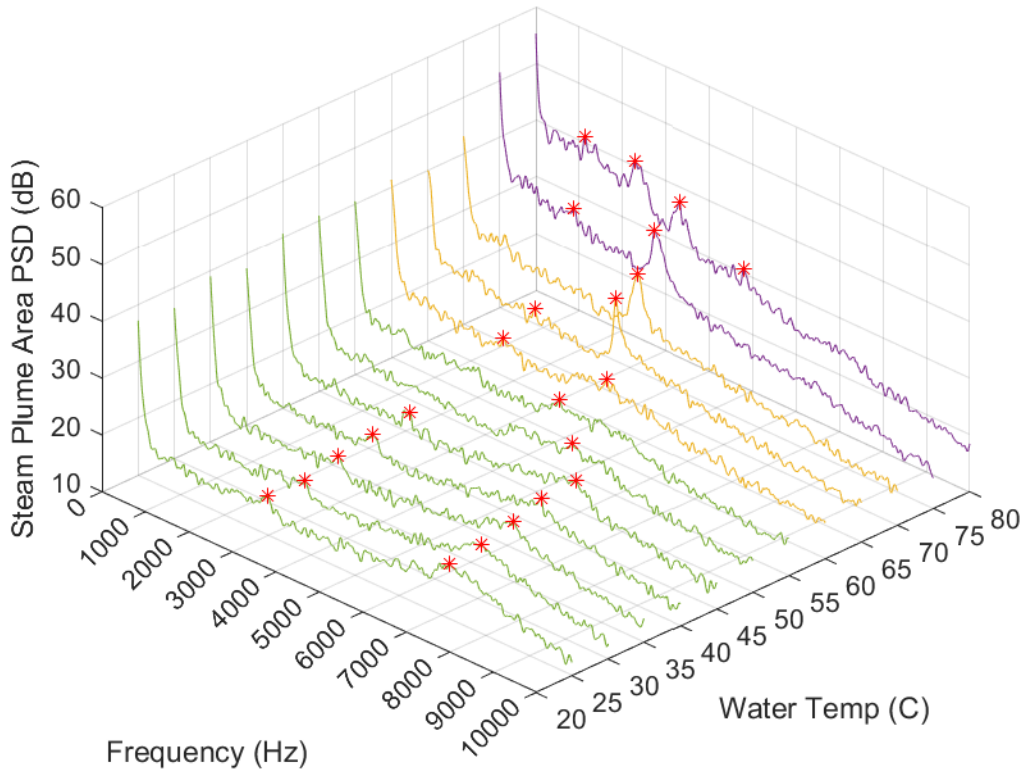

Figure 75. Waterfall plot of the 3C plume area PSD as a function of water temperature at a pressure ratio of 0.472 (water pressure = 30 psig, steam pressure = 80 psig). Green is stable, yellow is condensation oscillation, and purple is transition. Frequencies follow a decreasing trend while amplitudes increase as water temperature is increased.

8.4 Comparison of Internal Chamfer Nozzles

As mentioned throughout this chapter, a comparison of the 1C, 2C, and 3C nozzles suggests that a similar pathway to instability occurs independent of other nozzle parameters like L/D ratio, as shown in the regime map of Fig. 76. All three nozzles enter the condensation oscillation regime around 60°C. All three nozzles enter the transition regime around 75°C. None of the nozzles go fully unstable under the current temperature range. While the ‘best’ nozzle may not be in this study, the fact that consistent stability results can be found across multiple nozzles with varying geometries can be important for multiple product designs.

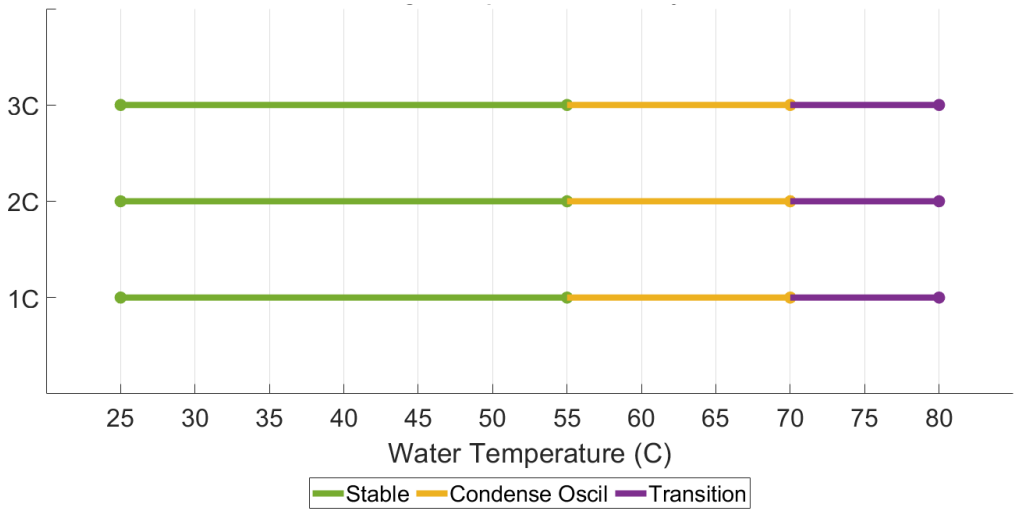

Figure 76. Regime map of condensation stability as a function of process water temperature and internal chamfer nozzle. All trials are collected at pressure ratios of 0.472 and water flow rates of 15 gpm.

The x-ray cross sections of the internal chamfer nozzles in Figs. 77, 78, and 79 do not show significant deviations from their schematics. Thus, it is assumed that it is the internal chamfer is responsible for the consistent results between nozzles.

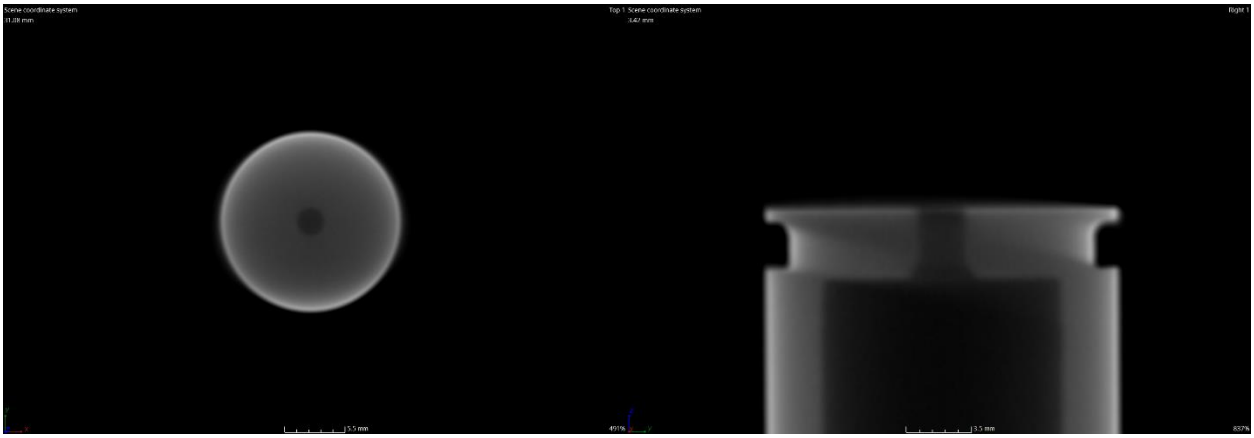

Figure 77. X-ray scan of the normal (left) and tangent (right) views of the 1C nozzle

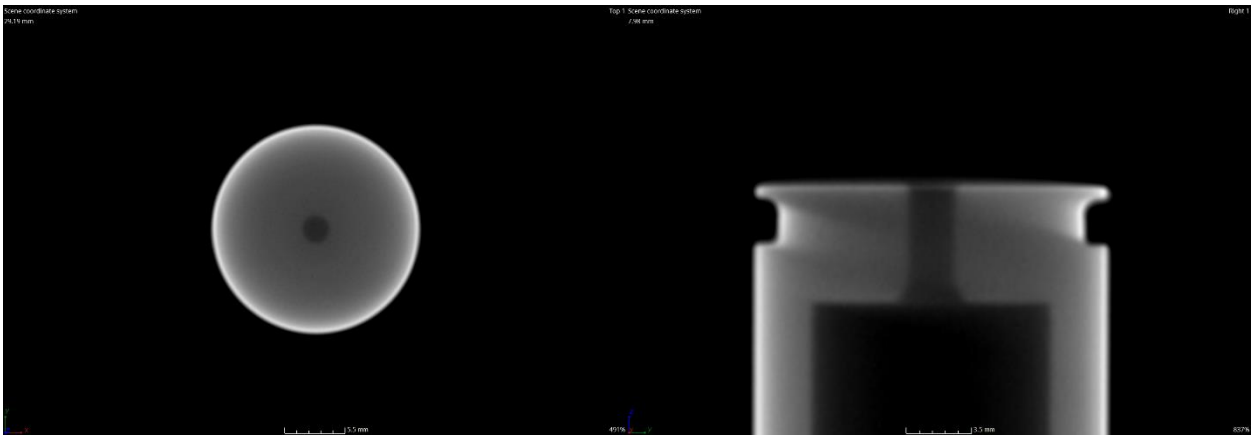

Figure 78. X-ray scan of the normal (left) and tangent (right) views of the 2C nozzle

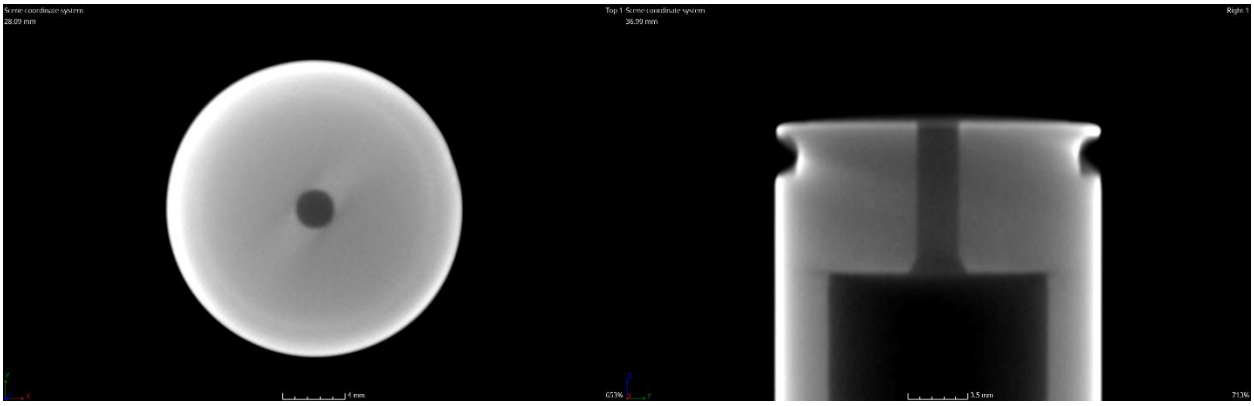

Figure 79. X-ray scan of the normal (left) and tangent (right) views of the 3C nozzle

9. Summary and Conclusions

Previous research has been devoted to the impact of process parameters on the stability of direct contact condensation. Many regime maps have been constructed based on process water temperature and steam mass flux with varying results between experiments. The consensus in the literature is that increasing the process water temperature or decreasing the steam mass flux results in an unstable mode of condensation; these conclusions are affirmed in this thesis. The point at which this instability occurs, however, has varied between experiments and prevented researchers from creating a single, unified regime map. Part of the reason for this is the wide range of injection environments that are possible for

direct contact condensation. Injection into a stagnant pool can occur vertically downward or horizontally. Injection into a process flow is even more complex, with injection possibly occurring in crossflow, parallel flow, counterflow, horizontal, vertical, angled. The experimental facility used in this thesis is limited to the case of injecting vertically upward into a crossflow of process water. Many different nozzle sizes, lengths, and shapes have been used to explore direct contact condensation; however, an original study on the nozzle geometry effects in isolation (i.e., holding all other parameters constant) has not been published to this author's knowledge. This thesis serves as an exploration into geometric considerations for direct contact condensation stability. A regime map of all nozzles presented in this thesis is shown in Fig. 80 with dashed lines demarcating the three nozzle groups to summarize and compare results.

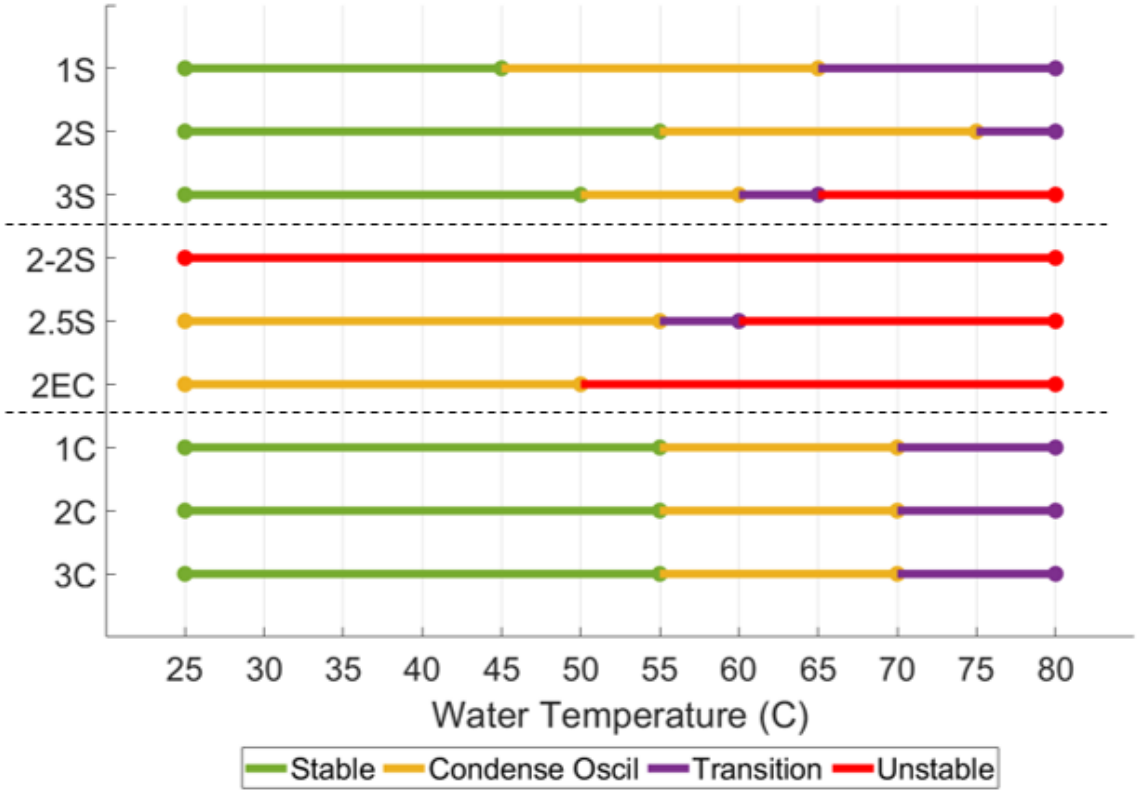

Figure 80. Regime map of condensation stability as a function of process water temperature and all nozzles presented in this work, split by cohort. All trials are collected at a pressure ratio of 0.472 (water pressure = 30 psig, steam pressure = 80 psig) and water flow rates of 15 gpm.

A nozzle geometry that has been used in the previous grad student Max Brennan's research serves as the starting point for comparison. The so-called 1S nozzle has been previously mapped based on nozzle pressure ratio and process water temperature [38]. For every nozzle tested here, the same temperature sweep from 25-80°C is performed at an intermediate pressure ratio (0.472) and water flow rate (15 gpm). This region was selected because it is known to have all regimes represented, which is helpful for comparison's sake. Through the temperature sweep, it is noted that the steam plume transforms from stable to the wild oscillations associated with the condensation oscillation regime around 50°C.and to the back-and-forth struggle of going unstable and then pulling back into a single plume that is the transition regime around 70°C. Looking at the frequency response of the plume area through this sweep, the steam plume shows low amplitude, high frequency (~6000-7000 Hz) oscillations in the stable regime that similarly show up in the outlet pressure frequency spectrum of a similar magnitude. High amplitude, medium frequency (~4000 Hz) oscillations start to appear when the plume approaches the condensation oscillation regime, again showing up in the outlet pressure frequency spectrum. It is when the plume goes temporarily unstable in the transition regime that low frequency peaks (~500-3000 Hz) dominate the chaotic bubbling structure that the plume devolves into and that much greater activity is noticed on the outlet pressure spectrum. It is also noted as a general trend that the plume area oscillations decrease in frequency and increase in magnitude as instability is approached, as well as the entire frequency spectrum rising in magnitude.

The effect of nozzle length to diameter (L/D) ratio is then explored through the 1S, 2S, and 3S nozzles, increasing the L/D ratio from 1 to 2 to 3, respectively. From comparison of plume area spectrum and videos, the 2S nozzle shows an improvement over the 1S nozzle, but the 3S performs the worst out of the three. Specifically, the 2S nozzle reaches the condensation oscillation regime at 60°C and the transition regime at 80°C, an improvement of 10°C for each regime change. The 3S nozzle does not enter the condensation oscillation regime until 55°C, but it quickly goes through the transition regime at 65°C to become fully unstable at 70°C, a regime not noticed in the other nozzles. This suggests that a L/D ratio

of 2 may be an optimal value for nozzle stability, but a larger set of L/D ratios would be needed to confirm this. This dataset was attempted but instead lead to the discovery that very slightly imperfect nozzle geometries had a profound effect on condensation stability.

A recreation of the purportedly 'best' 2S nozzle was machined to confirm the testing results, but the new nozzle performed horribly even at the start of the temperature sweep, being the worst out of all of the nozzles presented in this thesis. An examination of the internal geometry of the 2-2S nozzle through an x-ray scan shows that defects occurred to the nozzle during the machining process. An obstruction was found at the inlet of the nozzle, possibly due to the hole not being fully drilled out or a burr forming from machining the entrance chamber geometry. An expansion was also found at the exit of the nozzle. It is hypothesized that the combination of these nozzle 'defects' contribute to the earlier breakdown to an unstable bubbling structure. This is supported by the 2.5S and 2EC nozzles. The 2.5S nozzle, which was supposed to further validate the L/D effect study, shows an early entrance to the unstable regime at 60-65°C. Examination of the nozzle x-ray shows a less prominent but still noticeable obstruction at the inlet of the nozzle. The 2EC nozzle duplicates the outlet expansion of the 2-2S nozzle and shows an early instability at 55°C. These nozzles drive home the theory that small geometric imperfections can have a large impact on the condensation stability of steam injection. Careful machining practices need to be put in place if a straight-bore nozzle is to be used as the injection geometry.

Finally, an examination of adding a 30° chamfer at the inlet of the nozzle to better guide flow showed interesting results. The 1S, 2S, and 3S nozzle schematics from the L/D study were altered by adding the internal chamfer; these are referred to as the 1C, 2C, and 3C nozzles, respectively, and retested under the same conditions. All nozzles produced the same pathway to instability and similar frequency spectrums. All nozzles would enter the condensation oscillation regime at 60°C and the transition regime at 75°C. Thus, while some nozzles would show improvement over their straight nozzle counterparts (1C vs 1S, 3C vs 3S), others broke down faster (2C vs 2S). Instead, it appears that the internal chamfer negates other geometry effects like the L/D ratio and produce consistent, predictable results across many nozzles.

In conclusion, nozzle geometry plays a significant factor in the stability of direct contact condensation, and this needs to be considered when discussing condensation regime boundaries. A straight-bore nozzle can be designed to handle the highest process water temperatures, such as the 2S nozzle, but slight imperfections can result in a nozzle that turns unstable immediately upon introduction to the process water, as seen in the 2-2S nozzle. A high amount of unpredictability in the stability of straight nozzles will be inherent without tight tolerancing and good machining practices. Inlet contractions or outlet expansions produce nozzles of lower caliber for stability purposes. On the flip-side of this argument, an internal chamfer machined into the nozzle produces good stability results, although they may not be the 'best' results.

Thus, some rules of thumb may be laid for nozzle design in direct contact condensation:

1. A L/D ratio of 2 appears to be the best for straight hole design in terms of stability.
2. Small imperfections need careful attention during the nozzle machining process. A nozzle that is not deburred properly at the inlet or deburred too much at the outlet can lead to early instability.
3. A nozzle that has a converging inlet produces a consistent pathway to instability that is close to, but not quite, the best-case scenario for the nozzle.

The exploration of nozzle geometry could go beyond that presented in this thesis. Other inlet and outlet effects could be studied to determine their effect on stability. A constant nozzle diameter was used in this exploration but varying this parameter could also lead to new conclusions on condensation regime boundaries and dominant frequencies found during injection. Further exploration of chamfer design could also prove useful to the design of injector nozzles. The possibilities of obtaining an 'optimal' nozzle geometry are endless, and this work serves to highlight this importance and the impact this can have on direct contact condensation stability.

Bibliography

[1] Arinobu, M., 1980, "Studies on the Dynamic Phenomena Caused by Steam Condensation in Water," *Proc. of ANSI/ASME/NRC International Topical Meeting on Nuclear Reactor Thermal Hydraulics*, Saratoga, New York, **1**, pp. 293-302.

[2] Chan, C. K., and Lee, C. K. B., 1982, "A Regime Map for Direct Contact Condensation," International Journal of Multiphase Flow, **8**(1), pp. 11-20.

[3] Aya, I., Nariai, H., and Kobayashi, M., 1980, "Pressure and Fluid Oscillations in Vent System due to Steam Condensation, (I): Experimental Results and Analysis Model for Chugging," Journal of Nuclear Science and Technology, **17**(7), pp. 499-515.

[4] Aya, I., Kobayashi, M., and Nariai, H., 1983, "Pressure and Fluid Oscillations in Vent System due to Steam Condensation, (II): High-frequency Component of Pressure Oscillations in Vent Tubes Under at Chugging and Condensation Oscillation," Journal of Nuclear Science and Technology, **20**(3), pp. 213-227.

[5] Nariai, H., and Aya, I., 1976, "Fluid and Pressure Oscillations Occurring at Direct Contact Condensation of Steam Flow with Cold Water," Nuclear Engineering and Design, **95**, pp. 35-45.

[6] Aya, I., and Nariai, H., 1987, "Boundaries Between Regimes of Pressure Oscillation Induced by Steam Condensation in Pressure Suppression Containment," Nuclear Engineering and Design, **99**, pp. 31-40.

[7] Liang, K. S., and Griffith, P., 1994, "Experimental and Analytical Study of Direct Contact Condensation of Steam in Water," Nuclear Engineering and Design, **147**(3), pp. 425-435.

[8] Chun, M. H., Kim, Y. S., and Park, J. W., 1996, "An Investigation of Direct Contact Condensation of Steam Jet in Subcooled Water," International Communications in Heat and Mass Transfer, **23**(7), pp. 947-958.

[9] Cho, S., Song, C. H., Park, C. K., Yang, S. K., Chung, M. K., 1998, "Experimental Study on Dynamic Pressure Pulse in Direct Contact Condensation of Steam Discharging into Subcooled Water," *Proceedings of 1st Korea-Japan Symposium on Nuclear Thermal Hydraulics and Safety*, Pusan, Korea, **1**, pp. 291-298.

[10] Lee, S. I., and No, H. C., 1998, "Gravity-driven Injection Experiments and Direct-contact Condensation Regime Map for Passive High-pressure Injection System," Nuclear Engineering and Design, **183**(3), pp. 213-234.

[11] Petrovic de With, A., Calay, R.K., and de With, G., 2007, "Three-dimensional Condensation Regime Diagram for Direct Contact Condensation of Steam Injected into Water," International Journal of Heat and Mass Transfer, **50**, pp. 1762-1770.

[12] Wu, X., Yan, J., Pan, D., Liu, G., and Li, W., 2009, "Condensation Regime Diagram for Supersonic/Sonic Steam Jet in Subcooled Water," Nuclear Engineering and Design, **239**, pp. 3142-3150.

[13] Xu, Q., Guo, L., Zou, S., Chen, J., and Zhang, X., 2013, "Experimental Study on Direct Contact Condensation of Stable Steam Jet in Water Flow in a Vertical Pipe," International Journal of Heat and Mass Transfer, **66**, pp. 808-817.

[14] Zong, X., Liu, J. J., Yang, X. P., and Yan, J. J., 2015, "Experimental Study on the Direct Contact Condensation of Steam Jet in Subcooled Water Flow in a Rectangular Mix Chamber," International Journal of Heat and Mass Transfer, **80**, pp. 448-457.

[15] Xu, Q., and Guo, L., 2016, "Direct Contact Condensation of Steam Jet in Crossflow of Water in a Vertical Pipe. Experimental Investigation on Condensation Regime Diagram and Jet Penetration Length," International Journal of Heat and Mass Transfer, **94**, pp. 528-538.

[16] Xu, Q., Guo, L., and Chang, L., 2017, "Interfacial Characteristics of Steam Jet Condensation in Crossflow of Water in a Vertical Pipe," Applied Thermal Engineering, **113**, pp. 1266-1276.

[17] Xu, Q., Guo, L., and Chang, L., 2017, “Mechanisms of Pressure Oscillation in Steam Jet Condensation in Water Flow in a Vertical Pipe,” International Journal of Heat and Mass Transfer, **110**, pp. 643-656.

[18] Gregu, G., Takahashi, M., Pellegrini, M., and Mereu, R., 2017, “Experimental Study on Steam Chugging Phenomenon in a Vertical Sparger,” International Journal of Multiphase Flow, **88**, pp. 87-98.

[19] Zhao, Q., and Hibiki, T., 2018, “Review: Condensation Regime Maps of Steam Submerged Jet Condensation,” Progress in Nuclear Energy, **107**, pp. 31-47.

[20] Xu, Q., Ye, S., Chen, Y., Chen, Q., and Guo, L., 2018, “Condensation Regime Diagram for Supersonic and Subsonic Steam Jet Condensation in Water Flow in a Vertical Pipe,” Applied Thermal Engineering, **130**, pp. 62-73.

[21] Kerney, P.J., Faeth, G.M., and Olson, D. R., 1972, “Penetration Characteristics of a Submerged Steam Jet,” AlChE Journal, **18**(3), pp. 548-553.

[22] Gulawani, S. S., Joshi, J. B., Shah, M. S., RamaPrasad, C. S., and Shukla, D. S., 2006, “CFD Analysis of Flow Pattern and Heat Transfer in Direct Contact Steam Condensation,” Chemical Engineering Science, **61**, pp. 5204-5220.

[23] Chong, D., Quanbin, Z., Yuan, F., Wang, W., Chen, W., and Yan, J., 2015, “Research on the Steam Jet Length with Different Nozzle Structures,” Experimental Thermal and Fluid Science, **64**, pp. 134-141.

[24] Simpson, M. E., and Chan, C. K., 1982, “Hydrodynamics of a Subsonic Vapor Jet in Subcooled Liquid,” Journal of Heat Transfer, **104**(2), pp. 271-278.

[25] Damasio, C., Del Tin, G., Fiegna, G., and Malandrone, M., 1985, “Experimental Study on the Unstable Direct Contact Condensation Regimes,” *Proc. of 3rd International Topical Meeting on Reactor Thermal Hydraulics,* Newport, Rhode Island, **1**, pp. 6.C1-6.C8.

[26] Hong, S. J., Park, G. C., Cho, S., and Song, C., 2012, "Condensation Dynamics of Submerged Steam Jet in Subcooled Water," International Journal of Multiphase Flow, **39**, pp. 66-77.

[27] Qiu, B., Yan, J., Liu, J., Chong, D., Zhao, Q., and Wu, X., 2014, "Experimental Investigation on the Second Dominant Frequency of Pressure Oscillation for Sonic Steam Jet in Subcooled Water," Experimental Thermal and Fluid Science, **58**, pp. 131-138.

[28] Villanueva, W., Li, H., Puustinen, M., and Kudinov, P., 2015, "Generalization of Experimental Data on Amplitude and Frequency of Oscillations Induced by Steam Injection into a Subcooled Pool," Nuclear Engineering and Design, **295**, pp. 155-161.

[29] Chong, D., Zhao, Q., Yuan, F., Yuelei, C., Chen, W., and Yan, J., 2015, "Experimental and Theoretical Study on the Second Dominant Frequency in Submerged Steam Jet Condensation," Experimental Thermal and Fluid Science, **68**, pp. 744-758.

[30] Chen, W., Wang, Y., Zhao, Q., Chong, D., and Yan, J., 2016, "Experimental Investigation on the Second Dominant Frequency of Supersonic Steam Jet Condensation Oscillation and its Propagation Characteristic," Annals of Nuclear Energy, **97**, pp. 122-131.

[31] Qiu, B., Yang, Q., Junjie, Y., Li, G., and Revankar, S., 2017, "Experimental Investigation on the Propagation Characteristics of Pressure Oscillation in Direct Contact Condensation with Low Max Flux Steam Jet," Experimental Thermal and Fluid Science, **88**, pp. 400-408.

[32] Xu, Q., and Guo, L., 2017, "Recognition of Steam Jet Condensation Regime in Water Pipe Flow System by Statistical Features of Pressure Oscillation," Applied Thermal Engineering**, 117**, pp. 213-224.

[33] Yang, X., Fu, P., Chen, N., Liu, J., and Wei, J., 2019, "Mechanisms of Pressure Pulse for Condensing Supersonic Steam Jet in a Rectangular Channel," Experimental Thermal and Fluid Science, **105**, pp. 223-233.

[34] Tang, J., Yan, C., Sun, L., Li, Y., and Wang, K., 2015, “Effect of Liquid Subcooling on Acoustic Characteristics during the Condensation Process of Vapor Bubbles in a Subcooled Pool,” Nuclear Engineering and Design, **293**, pp. 492-502.

[35] Tang, J., Yan, C., and Sun, L., 2015, “Feature of Acoustic Sound Signals Involved in Vapor Bubble Condensation and its Application in Identification of Condensation Regimes,” Chemical Engineering Science, **137**, pp. 384-397.

[36] Tang, J., Yan, C., and Sun, L., 2015, “A Study Visualizing the Collapse of Vapor Bubbles in a Subcooled Pool,” International Journal of Heat and Mass Transfer, **88**, pp. 597-608.

[37] Barot, V., 2011, “Thermal and Fluid Behavior of a Steam-driven Jet in Subcooled Water Crossflow,” M.S. dissertation, University of Wisconsin – Madison, Madison, WI.

[38] Brennan, M., 2018, “Conditional Stability of a Steam Jet during Direct Contact Condensation in Subcooled Water Crossflow,” M.S. dissertation, University of Wisconsin – Madison, Madison, WI.

Appendix A – Literature Regime Definitions and Parameters

Authors	Regime Parameters	Identified Condensation Regimes	Injection Environment	Steam Jet Orientation	Nozzle Diameter [mm]	Water Temp [C]	Steam Mass Flux [kg/m*s]
Arinobu [1]	Water temperature, steam mass flux	I, II (chugging), III, IV (condensation oscillation), V, VI	Stagnant	Vertical downward	16.1, 27.6	20-92	5-100
Chan & Lee [2]	Water temperature, steam mass flux	Oscillatory bubble, oscillatory interface, oscillatory cone jet, ellipsoidal jet, ellipsoidal oscillatory bubble, external chug with encapsulating bubble, external chug with detached bubble, internal chug	Stagnant	Vertical downward	51	40-90	1-175
Aya et al. [3,4] Nariai & Aya [5]	Water temperature, steam mass flux	Large chugging, small chugging, bubbling, condensation oscillation, transition, I, II-a, II-b, III, IV	Stagnant	Vertical downward	18, 29	10-100	0-200
Liang & Griffith [7]	Water temperature, steam mass flux	Chugging, low frequency bubbling with detached bubbles, high frequency bubbling with attached bubbles, oscillatory jet, stable jet	Cocurrent	Vertical upward, mixing chamber	19	60-90	0-50
Chun et al. [8]	Water temperature, steam mass flux	Condensation oscillation, stable condensation, interfacial oscillation condensation, bubbling condensation oscillation, chugging, transition region from chugging to condensation oscillation	Stagnant	Horizontal, vertical downward	1.35, 4.45, 7.65, 10.85	13-84	200-1600
Cho et al. [9]	Water temperature, steam mass flux	Chugging, transition chugging, condensation oscillation, bubble condensation oscillation, stable condensation, interface oscillation condensation	Stagnant	Horizontal	5, 10, 15, 20	20-95	45-450
Lee & No [10]	Water tempearture, steam mass flux	Chugging, subsonic jetting, transition I, transition II, steam cavity	Stagnant	Vertical downward	150	31-91	20-80
De With et al. [11]	Water subcooling, steam mass flux, nozzle diameter	divergent jetting, ellipsoidal jetting, conical jetting, bubbling, chugging, interfacial condensation oscillation, no condensation	Stagnant	Varied	10-50	10-90	0-1500

Authors	Regime Parameters	Identified Condensation Regimes	Injection Environment	Steam Jet Orientation	Nozzle Diameter [mm]	Water Temp [C]	Steam Mass Flux [kg/m*s]
Wu et al. [12]	Water temperature, steam mass flux, nozzle pressure ratio	Double expansion divergent, double expansion contraction, expansion contraction, contraction, contaction expansion contraction, unstable jet	Stagnant	Horizontal	D_{cr} = 8, D_e = 8, 8.8, 9.6, 10.4, 11.2	20-70	298-865
Xu et al. [13]	Water temperature, steam mass flux, water Reynolds number	Hemisphere, conical, cylinder, divergent, ellipsoidal	Cocurrent	Vertical upward, vertical crossflow	8	20-70	150-500
Zong et al. [14]	Steam mass flux, water mass flux, water temperature	Divergent jet, stable jet, oscillatory jet, bubble flow	Cocurrent	Horizontal, mixing chamber	D_{cr} = 8 x 8 rectangular, D_e = 10 x 10 rectangular	20-60	200-600
Xu & Guo [15]	Water temperature, steam mass flux, water Reynolds number	Chugging, condensation oscillation, stable - conical, stable - expansion, stable - cylinder	Angled current	45° vertical upward	5	20-70	70-620
Xu et al. [16]	Ambient (outlet) pressure, steam mass flux	Expansion-contraction, double expansion-contraction, contraction, cylinder, hemisphere	Crosscurrent	Horizontal	3	20-70	0-900
Xu et al. [17]	Water tempearture, steam mass flux, water Reynolds number	Stable, oscil-I, oscil-II, chugging	Cocurrent	Vertical upward	8	20-70	0-500
Gregu et al. [18]	Water temperature, steam mass flux	Small encapsulating bubbles, big encapsulating bubbles, big encapsulating elongated bubbles, non-encapsulating bubbles, small chugging, internal chugging	Stagnant	Vertical downward	27	19-46.5	5.5-19.5
Xu et al. [20]	Ambient (outlet) pressure, steam mass flux, water temperature	Stable, oscil-I, oscil-II, chugging	Countercurrent	Vertical downward	D_{cr} = 3, D_e = 3.8	30-70	0-800
Zhao & Hibiki [19]	Many	Chugging, hemispherical bubble oscillation, condensation oscillation, stable condensation, steam escape, no condensation	Varied	Varied	Varied	Varied	Varied

Appendix B – Comparison of Literature to Experimental Regimes

Authors	New Regimes				
	Stable	Condensation Oscillation	Transition	Unstable	Uncategorized
Arinobu [1]	III	IV (CO)		V	I, II (chugging), VI
Chan & Lee [2]	Ellip jet	Oscil cone jet		Oscil bubble, ellip oscil bubble	Ext chug with encap bubble, ext chug with detached bubble, int chug, oscil interface
Aya et al. [3,4] Nariai & Aya [5]		CO	Trans	Bubbling	Large chugging, small chugging,
Liang & Griffith [7]	Stable jet	Oscil jet		Low freq bubbling with detached bubbles, high freq bubbling with attached bubbles	Chugging
Chun et al. [8]	Stable	CO, interfacial oscil cond		Bubbling cond oscil	Chugging, trans from chugging to CO
Cho et al. [9]	Stable	CO, interface oscil cond		Bubble cond oscil	Chugging, trans chugging
Lee & No [10]				Subsonic jet	Chugging, Trans I, Trans II, steam cavity
De With et al. [11]	Ellip jetting, con jetting, diverg jetting	Interfacial cond oscil		Bubbling	Chugging, NC
Wu et al. [12]	Double expan diverg, double expan contract, expan contract, contract, contact expan contract			Unstable jet	
Xu et al. [13]	Hemi, conical, cyl, ellip	Divergent			
Zong et al. [14]	Stable jet	Oscil jet		Bubble flow	Divergent jet
Xu & Guo [15]	Stable - conical, stable - cyl, stable - expan	CO			Chugging
Xu et al. [16]	Expansion-contract, double expan-contract, contract, cyl, hemi				
Xu et al. [17]	Stable			Oscil-I	Chugging, Oscil-II
Gregu et al. [18]					SEB, BEB, BEEB, NEB, small chugging, internal chugging
Xu et al. [20]	Stable			Oscil-I	Chugging, Oscil-II
Zhao & Hibiki [19]	Stable	CO		Hemi bubble oscil	Chugging, SE, NC